A frequency-independent second-order framework for the formulation of experimental fluidelastic forces using hidden flow variables

J. Antunes, Philippe Piteau, Xavier Delaune, Romain Lagrange, Domenico Panunzio

A frequency-independent second-order framework for the formulation of experimental fluidelastic forces using hidden flow variables

J. Antunes[a*], P. Piteau[b], X. Delaune[b], R. Lagrange[b], D. Panunzio[b]

[a] Centro de Ciências e Tecnologias Nucleares (C2TN), Instituto Superior Técnico (IST), Universidade de Lisboa, 2695-066 Bobadela LRS, Portugal

[*] jantunes@ctn.tecnico.ulisboa.pt

[b] Université Paris-Saclay, CEA, Service d'Etudes Mécaniques et Thermiques, F-91191 Gif-sur-Yvette, France

Keywords: Flow-induced vibrations, Flow-structure coupling, Fluidelastic instability, Tube bundles.

ABSTRACT

The importance of fluidelastic forces in flow-excited vibrations is crucial, in view of their damaging potential. Flow-coupling coefficients are often experimentally obtained from vibration experiments, performed within a limited experimental frequency range. For any given flow velocity, these coefficients are typically frequency-dependent, as amply documented in the literature since the seminal work of Tanaka and Takahara. Such frequency dependence, which seems quite natural in view of the flows intricacies, not only is awkward for attempting physical interpretations, but also leads to numerical difficulties when performing time-domain computations. In this work, we address this problem by assuming that the measured fluidelastic forces encapsulate "hidden" (non-measured) dynamics of the coupled flow. This leads to the possibility of modelling the flow-structure coupled dynamics through conventional ordinary differential equations with constant parameters. The substructure analysis of such a model, augmented with a set of "hidden" flow variables, readily highlights an inevitability of the frequency-dependence found in the measured flow forces, when these are condensed at the measurement degrees of freedom. The formulation thus obtained clearly suggests the mathematical structure of the measured fluidelastic forces, in particular providing the formal justification for a modelling approach often used in unsteady aeroelasticity. Then, inspired by previous work in the fields of viscoelasticity and soil-structure interaction, we proceed by identifying adequate frequency-independent second-order flow-coupling matrices from the frequency-dependent experimental data, which is a challenging identification problem, even for the specific case of symmetric coupling detailed here. Finally, the developed concepts and procedures are applied to experimental results obtained at CEA-Saclay (France), for the fluidelastic interaction forces acting on a flexible tube within a rigid bundle, although the problem addressed embraces a much wider range of applications. The proposed flow modelling and identification approach shows significant potential in practical applications, with many definite advantages.

1. Introduction

When dealing with flow-induced vibrations, the importance of fluidelastic forces should not be underestimated, in view of their damaging potential. This has been amply documented by many researchers, see books by Chen (1987), Blevins (2001), Païdoussis et al. (2011), Kaneko et al. (2014) and Pettigrew et al. (2022), hence the need for advanced models of fluidelastic coupling, as well as for experimental coupling coefficients, to feed and validate such models. In this work, the problem of fluid-elastic data reduction is revisited in the context of heat-exchanger tube bundle vibrations, although the main features of the proposed framework embrace a much wider range of flow-structure coupled systems.

Flow-structure fluidelastic forces are difficult to model theoretically, due to complex fluid dynamics, often involving flow separation and severe vorticity. The physics are somewhat more

manageable for structures subjected to axial and azimuthal flows, with no or very limited separation, enabling the development of quite effective theoretical models, as documented in the extensive work by Païdoussis (2014, 2016), as well as for rotor-flow coupled problems, as addressed for instance by Antunes et al. (1996). The modelling problem is however quite different and more delicate whenever flow separation is an essential feature of the problem, which arises when structures are subjected to cross-flows, typified by the specific case of fluidelastic vibrations in heat-exchanger tube bundles.

For this important problem, semi-empirical models were developed since the sixties, such as the early jet-switch model by Roberts (1962), followed by the quasi-static Connors (1970)-Blevins (1974) approach. These efforts were later rethought and refined on a more physical ground since the early eighties, as reviewed by Price (1995), Païdoussis et al. (2011) and Kaneko et al. (2014). Particularly significant are the unsteady model of Tanaka and Takahara (1981) and Chen (1983a, 1983b), the semi-analytical model developed by Lever and Weaver (1982), the quasi-steady model by Price and Païdoussis (1984) and the quasi-unsteady model proposed by Granger and Païdoussis (1996). Numerical dynamical computations have recently been developed, based on coupled structural / flow numerical computations, as typified by the work of Anderson et al. (2014) and De Pedro et al. (2016).

Research efforts on simplified physical modelling and understanding of the flow-structure coupling forces are actively pursued, leading to increasingly elaborate theoretical approaches. The work of Lever and Weaver (1982) already pointed the need for a postulated delay (or phase lag) between the structural motion and the ensuing flow-coupling force, in order to obtain fluidelastic instability. Such need was also corroborated by Price and Païdoussis (1984) and reiterated in most ulterior work, which focused on improving the somewhat fuzzy physical understanding of the delayed term, refining the delay modelling, as well as inferring the delay function from actual measurements. These aspects have been addressed in significant papers since Granger and Païdoussis (1996), including Meskell (2009), Hassan et al. (2010), El Bouzidi and Hassan (2015), Mureithi (2017), Li and Mureithi (2017) and Alyaldin and Mureithi (2022, 2023).

On the course of these investigations, the simple time-lag originally used by Lever and Weaver (1982) and Price and Païdoussis (1984) evolved to a "memory function" developed by Granger and Païdoussis (1996), based on a linear combination of decaying exponentials, and more complex delay functions developed in more recent contributions. Interestingly, in the work by Granger and Païdoussis (1996) and by Mureithi and co-workers (2017, 2022, 2023) classic concepts from unsteady aeroelasticity are recalled, in order to develop fluidelastic time-lag functions for tube bundles as generalized versions of the Theodorsen aerofoil theory, see Fung (1969) or Dowell (2022).

Because of the difficulties in obtaining reliable models of fluidelastic forces, when the flows are complex, the coupling force coefficients are often experimentally identified from vibration experiments, in order to feed and/or validate the theoretical models. As conceptualized in Fig. 1, fluidelastic forces are often addressed through linearized flow-coupling coefficients, that are measured under flow, see Blevins (2001), Païdoussis et al. (2011) and Kaneko et al. (2014). These coefficients are typically obtained from vibration experiments performed at various flow velocities and vibration frequencies, see Sawadogo and Mureithi (2014a, 2014b) and Piteau et al. (2012, 2018, 2019). Fig. 2 illustrates experimental dimensionless fluidelastic stiffness and damping coefficients $C_k(V_R)$ and $C_d(V_R)$, with $V_R = V_f / (fD)$, measured by Piteau et al. (2018) at CEA-Saclay (France) for a tube vibrating in the lift direction, within a rigid heat-exchanger square tube bundle subjected to single-phase cross-flow with pitch velocity V_p.

As shown in Fig. 2, fluidelastic coefficients have been found to be highly-dependent on the reduced velocity V_R (and therefore on the reduced frequency $f_R = fD/V_p = 1/V_R$, hence the reduced circular frequency $\bar{\omega} = \omega D / V_p = 2\pi f_R$) and, regardless of the identification method used, such data is typically confined to a feasible limited experimental range of the reduced frequency. The frequency-dependency of fluidelastic coefficients is amply documented in the literature, since the seminal work of Tanaka and Takahara (1981). Such behavior is extensively

reported in more recent fluidelastic force identification work, see Inada et al. (2002), Sawadogo and Mureithi (2014a, 2014b), Nishida et al. (2018) and Piteau et al. (2012, 2018, 2019). One should notice that the frequency-dependency of coupling forces is also encountered in many other physical problems beyond flow-structure interaction. These are of particular relevance in the fields of viscoelasticity, hydroelasticity and soil-structure interaction, see Golla and Hughes (1985), Friswell et al. (1997), Cummings (1962), Damaren (2000), Wolf (1994), Cottereau et al. (2007) and Ropars et al. (2014).

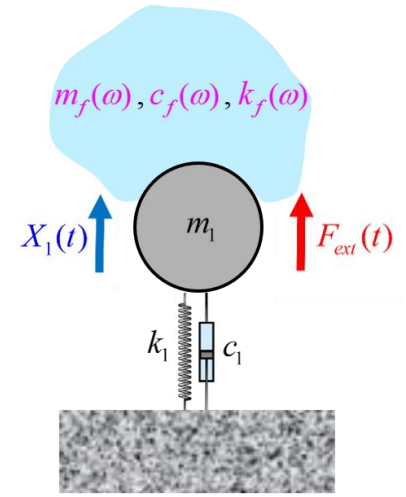

Fig. 1. Conceptual illustration of the identification of fluidelastic forces.

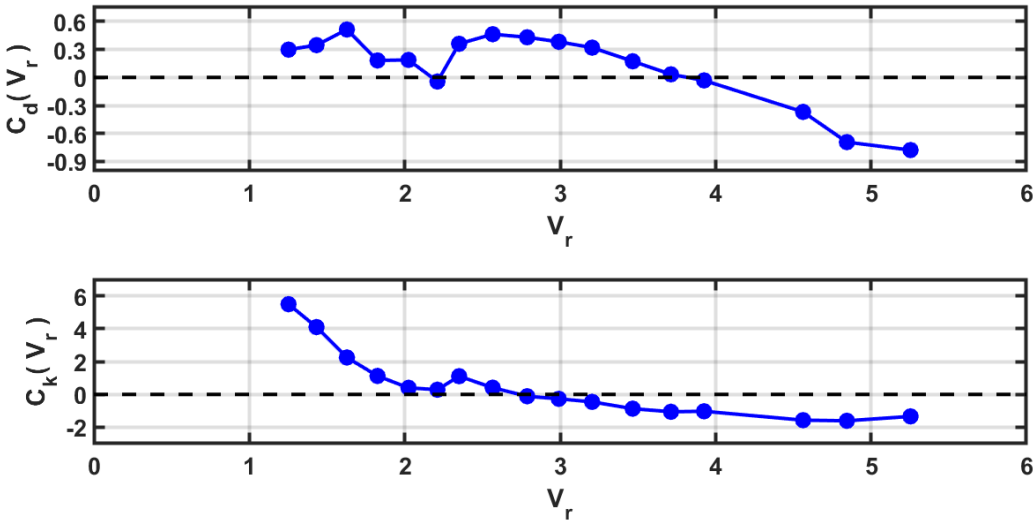

Fig. 2. Experimental fluidelastic stiffness and damping dimensionless coefficients per unit length, as a function of the reduced velocity $V_R = V_p / (fD)$, measured by Piteau et al. (2018).

In the context of flow-structure interaction, this frequency-dependency is essentially attributed to the complexity of the physical interaction phenomena. However, we believe that such dismissing view overlooks some important aspects, which will be detailed in the present work. For the sake of simplicity we will tacitly assume here that they solely depend on the reduced frequency, although such assumption is not strictly true, see Piteau et al. (2019) and Lagrange et al. (2019). The experimental flow coefficients depend on the reduced frequency in ways that cannot be anticipated. And, unfortunately, this behavior is very awkward for attempting physical interpretations, as the frequency-dependent fluidelastic coefficients $C_m(\bar{\omega})$, $C_d(\bar{\omega})$ and $C_k(\bar{\omega})$ do not actually represent inertia, viscous damping and stiffness, but much more complex physical entities, something that is often forgotten.

On the other hand, such frequency-dependency also leads to numerical difficulties when performing time-domain computations of the flow-coupled system responses, see Politopoulos et al. (2014) and Piteau et al. (2018). A common approach to deal with frequency-dependent

forces in the time-domain is through a convolution integral, which suffer from being computationally intensive. Moreover, convolution-based time-domain computations ask for adequate estimations of the fluidelastic impulse responses, which are typically obtained from the Inverse Fourier Transform (IFT) of the complex experimental flow-coupling matrix, thus imposing a very extended corpus of frequency-data to properly compute the IFT, which is seldom available experimentally. Naïve frequency-extrapolations of the experimental data will induce in particular causality issues, see Antunes et al. (2022). Actually, it appears that no ideal solution currently exists for an effective and physically appealing implementation of the experimental fluidelastic data in time-domain flow-structure coupled equations.

In our view, most difficulties for achieving a satisfactory description of the experimental fluidelastic forces stem from the fact that the flow dynamics are not directly accessed in measurements, but only indirectly through their impact on the measured structural degrees of freedom (DOF). To elaborate on this idea, we start by noting that, for very specific flow-structure configurations, the flow is highly constrained by the structure, so that one may safely assume that it lacks any "internal" self-dynamics and therefore can be described in terms of the structure DOF alone, at the flow-structure boundary interface. As illustrated in Fig. 3, two important systems for which such simplification is adequate are flow-conveying pipes and bearings/seals.

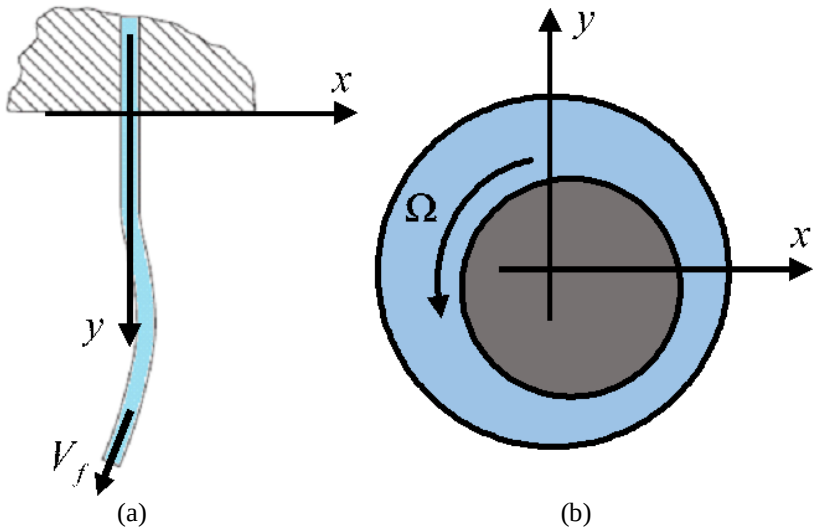

Fig. 3. Two systems for which the coupled flow does not entail additional degrees of freedom: (a) flow-conveying pipes with internal flow velocity V_f; (b) bearing/seals with rotor spinning velocity Ω.

However, when addressing structures subjected to less constrained flows, the fluid moves more freely and often displays separation phenomena and significant vortical structures, which constitute "internal" dynamical phenomena. This is illustrated in Fig. 4, extracted from the work by Marcel (2011), which presents the instantaneous vorticity field given by Computational Fluid Dynamics (CFD) of the turbulent cross-flow within a rigid square bundle, at two dimensionless time-instants, clearly showing flow structures of various length-scales which develop in space and time/frequency. Modelling of such a physical problem would clearly entail the need for additional degrees of freedom, pertaining to the flow. This view has been explicitly formulated in the specific case of structures subjected to flow vortex-shedding, a paradigmatic example typically described in terms of a structural equation coupled with a Van der Pol "flow oscillator" equation, see Païdoussis et al. (2011).

The "flow degrees of freedom" are therefore instrumental for better understanding the flow-structure coupled dynamics. However, in current practice, only the dynamics of the structural DOF are explicitly formulated, therefore the flow "hidden dynamics" are encapsulated in the measured frequency-dependent and/or time-delayed fluidelastic forces. The present work is concerned with the practical exploitation of experimentally obtained fluidelastic force coefficients, by explicitly addressing the flow internal dynamics through "hidden" (non-

measured) degrees of freedom. We show that the frequency-dependency of the coupling coefficients is unavoidable, even for very simple coupled subsystems with constant parameters, as a direct consequence of the condensation of the hidden dynamical variables of the unmeasured subsystem (e.g., the flow) on the structural variables accessible to the measurements.

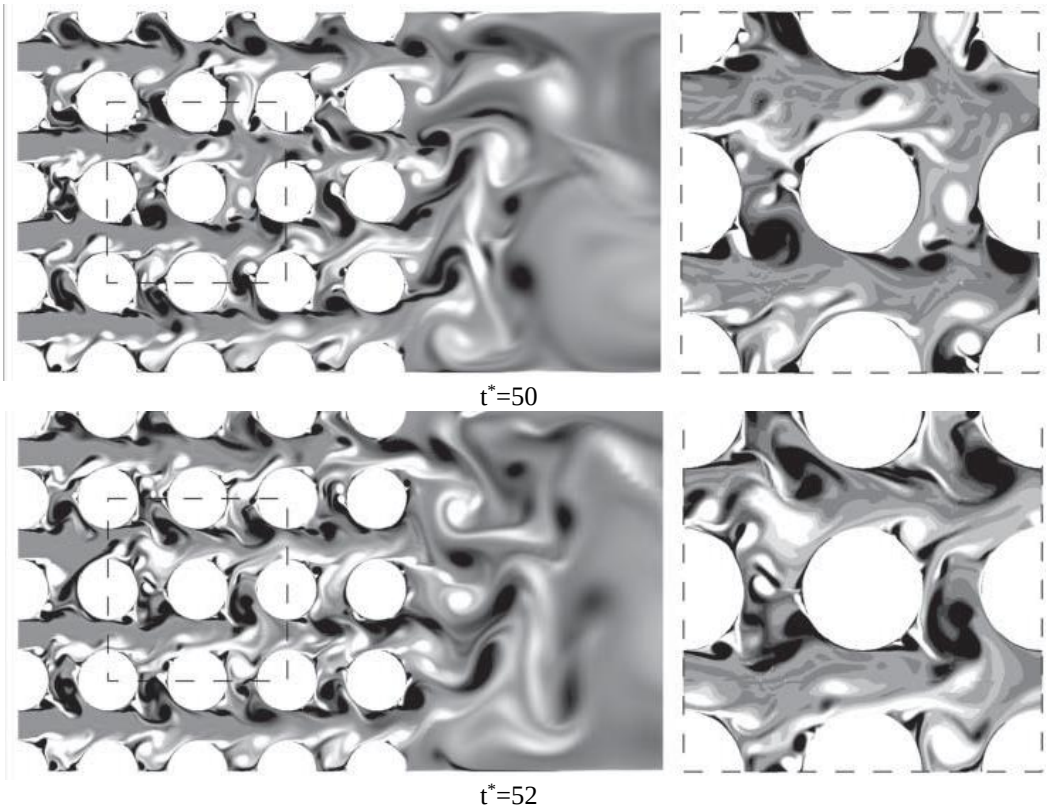

Fig. 4. Illustration of a system for which the coupled flow entails additional degrees of freedom: CFD iso-contours of the instantaneous vorticity (component perpendicular to the flow plane) within a rigid tube bundle at two dimentionless time-instants $t^* = tU_\infty / D$, with $\mathrm{Re} = 60000$, see Marcel (2011).

Then, by assuming that the measured fluidelastic forces encapsulate hidden DOF of the coupled flow, this leads to the possibility of formulating the full flow-structure coupled dynamics through conventional second-order ordinary differential equations (ODE) with frequency-independent flow-coupling standard matrices, which truly represent inertia, viscous dissipation and stiffness effects. Among many advantages, such a formulation may shed light on the system physical features, second-order representations being the most familiar to vibration practitioners. Moreover, the formulation thus obtained provides a formal clarification for a family of empirical modelling approaches widely used in the field of unsteady aeroelasticity, see Tewari (2015).

These ideas are developed using concepts and techniques common in model reduction theory and system analysis. In the course of the present work, we became aware that the use of hidden variables in augmented models, and hence similar efforts, have been developed in other fields, namely the modelling of viscoelastic structures and soil-structure interaction, where coupling coefficients are also strongly dependent on frequency. Such work in the above-mentioned fields led to comparable formal contexts and useful identification techniques well adapted to the general formulation developed here. Acordingly, the present work borrows important identification features from Cottereau et al. (2007), which somewhat connects with previous work from Golla and Hughes (1985), Paronesso and Wolf (1995) and Friswell et al. (1997).

A general framework is developed in the present paper for converting the experimental frequency-dependent fluidelastic data into a standard second-order matrix formulation of the flow-structure coupled system. The mathematical details of the actual conversion are somewhat

involved, even in the specific case of symmetric fluidelastic coupling, which is detailed here. The general case involving both symmetric and anti-symmetric coupling entails further mathematical difficulties and will be addressed in subsequent work. To embody the presentation, we apply the developed formulation and procedures to actual experimental data obtained at CEA-Saclay by Piteau et al. (2018). The measured fluidelastic lift force acting on a flexible tube within a rigid square bundle was modeled using the described techniques, with seemingly satisfactory results.

We believe that the proposed framework shows significant potential in a wide range of practical applications, with many definite advantages when dealing with measured fluidelastic forces, as summarized in the paper concluding section.

2. A common flow-structure formulation

2.1 Flow-structure equations

For compactness, in sections 2 to 4 we will express the experimental fluidelastic dynamical matrix $\mathbf{D}_{mm}^{FS}(\omega)$ in terms of its physical values (in N/m), as a function of the physical circular frequency. Their relation with the corresponding dimensionless fluidelastic quantities will be addressed in section 6. In the following, the generic notation $\mathbf{A}_{mn}$ (standing for any structural/flow mass, damping or stiffness matrix) denotes a dense matrix (or sub-matrix) of size $M \times N$, with subscripts $m = 1, 2, \cdots, M$ and $n = 1, 2, \cdots, N$. When referring to diagonal square matrices, such as when dealing with modal quantities, the matrix notation is italicized as $\boldsymbol{A}_{mm}$.

The general linearized formulation for the flow-coupled structure, as applied to a structure (S) with $m = 1, 2, \cdots, M$ DOF, assumed measurable, reads in the frequency-domain ω:

$$\left(-\omega^2 \mathbf{M}_{mm}^{S} + i\omega \mathbf{C}_{mm}^{S} + \mathbf{K}_{mm}^{S}\right)\mathbf{x}_m(\omega) = \mathbf{f}_m^{Ext}(\omega) + \mathbf{f}_m^{FS}(\omega) \tag{1}$$

where $\mathbf{M}_{mm}^{S}$, $\mathbf{C}_{mm}^{S}$ and $\mathbf{K}_{mm}^{S}$ are the symmetric mass, damping and stiffness matrices of the structure (with size $M \times M$), respectively, while the excitation force vector is $\mathbf{f}_m^{Ext}(\omega)$ and the flow-structure (*FS*) coupling force vector is $\mathbf{f}_m^{FS}(\omega)$ (both with size $M \times 1$), formulated with respect to the response vector $\mathbf{x}_m(\omega)$ at the $m = 1, 2, \cdots, M$ measured structural DOF:

$$\mathbf{f}_m^{FS}(\omega) = -\left(-\omega^2 \mathbf{M}_{mm}^{FS}(\omega) + i\omega \mathbf{C}_{mm}^{FS}(\omega) + \mathbf{K}_{mm}^{FS}(\omega)\right)\mathbf{x}_m(\omega) = -\mathbf{D}_{mm}^{FS}(\omega)\mathbf{x}_m(\omega) \tag{2}$$

where $\mathbf{M}_{mm}^{FS}(\omega)$, $\mathbf{C}_{mm}^{FS}(\omega)$ and $\mathbf{K}_{mm}^{FS}(\omega)$ are the so-called added mass, damping and stiffness flow-structure coupling matrices (also with size $M \times M$), which are in general frequency-dependent. From the inverse of formulation (2), it is clear that in general the fluidelastic forces $\mathbf{f}_m^{FS}(\omega)$ couple the structural DOF $\mathbf{x}_m(\omega)$.

Hence, the fluidelastic forces $\mathbf{f}_m^{FS}(\omega)$ are described through the measured dynamical flow-coupling dynamic matrix $\mathbf{D}_{mm}^{FS}(\omega)$:

$$\mathbf{D}_{mm}^{FS}(\omega) = -\omega^2 \mathbf{M}_{mm}^{FS}(\omega) + i\omega \mathbf{C}_{mm}^{FS}(\omega) + \mathbf{K}_{mm}^{FS}(\omega) \tag{3}$$

and the coupled problem is formulated as:

$$\left(-\omega^2 \mathbf{M}_{mm}^{S} + i\omega \mathbf{C}_{mm}^{S} + \mathbf{K}_{mm}^{S}\right)\mathbf{x}_m(\omega) + \mathbf{D}_{mm}^{FS}(\omega)\mathbf{x}_m(\omega) = \mathbf{f}_m^{Ext}(\omega) \tag{4}$$

or:

$$\left(-\omega^2\left(\mathbf{M}_{mm}^{S} + \mathbf{M}_{mm}^{FS}(\omega)\right) + i\omega\left(\mathbf{C}_{mm}^{S} + \mathbf{C}_{mm}^{FS}(\omega)\right) + \left(\mathbf{K}_{mm}^{S} + \mathbf{K}_{mm}^{FS}(\omega)\right)\right)\mathbf{x}_m(\omega) = \mathbf{f}_m^{Ext}(\omega) \tag{5}$$

which, in the time-domain, may be loosely written as:

$$\left(\mathbf{M}_{mm}^{S} + \mathbf{M}_{mm}^{FS}(\omega)\right)\ddot{\mathbf{x}}_m(t) + \left(\mathbf{C}_{mm}^{S} + \mathbf{C}_{mm}^{FS}(\omega)\right)\dot{\mathbf{x}}_m(t) + \left(\mathbf{K}_{mm}^{S} + \mathbf{K}_{mm}^{FS}(\omega)\right)\mathbf{x}_m(t) = \mathbf{f}_m^{Ext}(t) \tag{6}$$

2.2 Flow-structure equations in the time-domain

As stated before, a common approach to deal with frequency-dependent forces in the time-domain is through the convolution integral obtained from (2):

$$\mathbf{f}_m^{FS}(t) = -\int_0^t \mathbf{D}_{mm}^{FS}(t-\tau)\,\mathbf{x}_m(\tau)\,d\tau \quad \text{with} \quad \mathbf{D}_{mm}^{FS}(t) = \mathcal{F}^{-1}\left(\mathbf{D}_{mm}^{FS}(\omega)\right) = \frac{1}{2\pi}\int_{-\infty}^{\infty} \mathbf{D}_{mm}^{FS}(\omega)\,e^{i\omega t}\,d\omega \quad (7)$$

so that, from (4) and (7), the system time-domain response is computed as:

$$\mathbf{M}_{mm}^{S}\ddot{\mathbf{x}}_m(t) + \mathbf{C}_{mm}^{S}\dot{\mathbf{x}}_m(t) + \mathbf{K}_{mm}^{S}\mathbf{x}_m(t) + \int_0^t \mathbf{D}_{mm}^{FS}(t-\tau)\,\mathbf{x}_m(\tau)\,d\tau = \mathbf{f}_m^{Ext}(t) \quad (8)$$

which formally rigorous, compared to the loose form (6). It is clear from (8) that the convolution formulation for frequency-dependent fluidelastic forces leads to a computationally intensive integro-differential matrix equation. Moreover, as pointed before, expression (7) highlights the need for extensive experimental frequency-data $\mathbf{D}_{mm}^{FS}(\omega)$, in order to properly compute the impulse responses $\mathbf{D}_{mm}^{FS}(t)$ through the Inverse Fourier Transform (IFT).

2.3 Flow-structure eigen-formulation

The coupled system modes $(n) = 1, 2, \cdots, N$ are computed from (6), with $\mathbf{f}_m^{Ext}(t) \equiv \mathbf{0}_m$, by seeking solutions of the form $\mathbf{x}_m(\omega) = \{\boldsymbol{\phi}_m\}_{(n)} \exp\left(\lambda_{(n)} t\right)$. Then, the eigen-formulation reads:

$$\left(\lambda_{(n)}^2\left(\mathbf{M}_{mm}^{S} + \mathbf{M}_{mm}^{FS}(\omega_{(n)})\right) + \lambda_{(n)}\left(\mathbf{C}_{mm}^{S} + \mathbf{C}_{mm}^{FS}(\omega_{(n)})\right) + \left(\mathbf{K}_{mm}^{S} + \mathbf{K}_{mm}^{FS}(\omega_{(n)})\right)\right)\{\boldsymbol{\phi}_m\}_{(n)} = \mathbf{0}_m \quad (9)$$

with $\omega_{(n)} = \mathrm{Im}\left(\lambda_{(n)}\right)$. The complex eigenvalues $\lambda_{(n)} = \sigma_{(n)} + i\omega_{(n)}$ and eigenvectors $\{\boldsymbol{\phi}_m\}_{(n)}$ are computed from (9), for each mode (n), and the system stability can be inferred from the sign of the real part $\sigma_{(n)}$. However, the eigen-formulation (9) is clearly non-standard because of the frequency-dependence of the operators $\mathbf{M}_{mm}^{FS}(\omega)$, $\mathbf{C}_{mm}^{FS}(\omega)$ and $\mathbf{K}_{mm}^{FS}(\omega)$, which is a drawback, as it calls for specific numerical search/iterative schemes to compute the system eigen-solutions.

3. The proposed flow-structure formulation

3.1 Flow-structure equations in the frequency-domain

In the previous section we pointed several difficulties stemming from a common formulation of the experimental fluidelastic forces. Here we develop a second-order standard formulation for the coupled flow-structure, by augmenting the structure (S) dynamic model DOF $\mathbf{x}_m$ ($m = 1, 2, \cdots, M$) with additional DOF $\mathbf{x}_h$ ($h = 1, 2, \cdots, H$), which will describe explicitly the flow (F) internal dynamics and are hidden from experimentation. In the field of dynamic substructuring, the DOF of such partitioned system are often designated "master" and "slave" coordinates, see Leung (1993). Then, the partitioned model of the linearized coupled system:

$$\left(-\omega^2\mathbf{M} + i\omega\mathbf{C} + \mathbf{K}\right)\mathbf{x}(\omega) = \mathbf{f}^{Ext}(\omega) \quad (10)$$

reads:

$$\left(-\omega^2\begin{bmatrix}\mathbf{M}_{mm} & \mathbf{M}_{mh}\\ \mathbf{M}_{hm} & \mathbf{M}_{hh}\end{bmatrix} + i\omega\begin{bmatrix}\mathbf{C}_{mm} & \mathbf{C}_{mh}\\ \mathbf{C}_{hm} & \mathbf{C}_{hh}\end{bmatrix} + \begin{bmatrix}\mathbf{K}_{mm} & \mathbf{K}_{mh}\\ \mathbf{K}_{hm} & \mathbf{K}_{hh}\end{bmatrix}\right)\begin{Bmatrix}\mathbf{x}_m(\omega)\\ \mathbf{x}_h(\omega)\end{Bmatrix} = \begin{Bmatrix}\mathbf{f}_m^{Ext}(\omega)\\ \mathbf{0}_h\end{Bmatrix} \quad (11)$$

with a total of $P = M + H$ degrees of freedom, with M measured structure DOF and H hidden flow DOF. For instance, for a tube bundle subjected to transverse flow, $\mathbf{x}_m$ will be the vector

of tube displacements, while $\mathbf{x}_h$ will be a vector of relevant hidden flow motion variables. For convenience, the equations of this section will be written in terms of physical quantities. They will be adapted in section 6 to the dimensionless parameters used for fluidelastic forces.

Concerning the explicitly measured degrees of freedom, $\mathbf{f}_m^{Ext}$ is the vector of external excitation forces applied to the structure, while matrices $\mathbf{M}_{mm} = \mathbf{M}_{mm}^S + \mathbf{M}_{mm}^F$, $\mathbf{C}_{mm} = \mathbf{C}_{mm}^S + \mathbf{C}_{mm}^F$ and $\mathbf{K}_{mm} = \mathbf{K}_{mm}^S + \mathbf{K}_{mm}^F$ express the structure dynamical features, as well as the flow forces directly interacting at the measured degrees of freedom. On the other hand, concerning the flow non-measured (hidden) degrees of freedom, the flow-structure linearized effects are encapsulated in the square "internal" flow matrices $\mathbf{M}_{hh} \equiv \mathbf{M}_{hh}^F$, $\mathbf{C}_{hh} \equiv \mathbf{C}_{hh}^F$ and $\mathbf{K}_{hh} \equiv \mathbf{K}_{hh}^F$, as well as the rectangular flow-coupling matrices $\mathbf{M}_{mh} \equiv \mathbf{M}_{mh}^F$, $\mathbf{M}_{hm} \equiv \mathbf{M}_{hm}^F$, $\mathbf{C}_{mh} \equiv \mathbf{C}_{mh}^F$, $\mathbf{C}_{hm} \equiv \mathbf{C}_{hm}^F$, $\mathbf{K}_{mh} \equiv \mathbf{K}_{mh}^F$ and $\mathbf{K}_{hm} \equiv \mathbf{K}_{hm}^F$. All the flow-related matrices are assumed real and, with the mentioned assumptions, equation (11) reads:

$$\left(-\omega^2 \begin{bmatrix} \mathbf{M}_{mm}^S + \mathbf{M}_{mm}^F & \mathbf{M}_{mh}^F \\ \mathbf{M}_{hm}^F & \mathbf{M}_{hh}^F \end{bmatrix} + i\omega \begin{bmatrix} \mathbf{C}_{mm}^S + \mathbf{C}_{mm}^F & \mathbf{C}_{mh}^F \\ \mathbf{C}_{hm}^F & \mathbf{C}_{hh}^F \end{bmatrix} + \begin{bmatrix} \mathbf{K}_{mm}^S + \mathbf{K}_{mm}^F & \mathbf{K}_{mh}^F \\ \mathbf{K}_{hm}^F & \mathbf{K}_{hh}^F \end{bmatrix} \right) \begin{Bmatrix} \mathbf{x}_m(\omega) \\ \mathbf{x}_h(\omega) \end{Bmatrix} = \begin{Bmatrix} \mathbf{f}_m^{Ext}(\omega) \\ \mathbf{0}_h \end{Bmatrix} \quad (12)$$

Compared to the common flow-structure coupled formulation (4), equation (12) displays more flow-related coefficients, but they are not frequency-dependent. As will be shown in the following, this is because formulation (4) condenses all the coupled system dynamics into the measured DOF $\mathbf{x}_m$, while (12) is formulated in terms of both the measured and the flow hidden DOF $\mathbf{x}_h$. Both formulations can, in principle, be applied to any given flow-structure problem. Formulation (4) is based on directly accessible experimental flow parameters, which however are frequency-dependent and, as discussed before, lead to a non-standard eigen-problem. By contrast, formulation (12) is obviously more informative, is built on frequency-independent coefficients and leads to a standard eigen-problem, however it depends on flow quantities which are not directly accessible through experiments. At this point, the flow matrices in formulation (12) will be assumed without any specific structure. This aspect will be developed in the following and particularized with respect to symmetric flow-coupling.

Now, from classic model-reduction and substructuring concepts, see Leung (1993), interesting information can be extracted from (12), which is equivalent to the following pair of equations:

$$\begin{aligned} &\left(-\omega^2 \mathbf{M}_{mm}^S + i\omega \mathbf{C}_{mm}^S + \mathbf{K}_{mm}^S \right) \mathbf{x}_m(\omega) \\ &+ \left(-\omega^2 \mathbf{M}_{mm}^F + i\omega \mathbf{C}_{mm}^F + \mathbf{K}_{mm}^F \right) \mathbf{x}_m(\omega) + \left(-\omega^2 \mathbf{M}_{mh}^F + i\omega \mathbf{C}_{mh}^F + \mathbf{K}_{mh}^F \right) \mathbf{x}_h(\omega) = \mathbf{f}_m^{Ext}(\omega) \end{aligned} \quad (13)$$

and:

$$\left(-\omega^2 \mathbf{M}_{hm}^F + i\omega \mathbf{C}_{hm}^F + \mathbf{K}_{hm}^F \right) \mathbf{x}_m(\omega) + \left(-\omega^2 \mathbf{M}_{hh}^F + i\omega \mathbf{C}_{hh}^F + \mathbf{K}_{hh}^F \right) \mathbf{x}_h(\omega) = \mathbf{0}_h \quad (14)$$

Then, equation (14) leads to the following relation between $\mathbf{x}_h$ and $\mathbf{x}_m$:

$$\mathbf{x}_h(\omega) = -\left(-\omega^2 \mathbf{M}_{hh}^F + i\omega \mathbf{C}_{hh}^F + \mathbf{K}_{hh}^F \right)^{-1} \left(-\omega^2 \mathbf{M}_{hm}^F + i\omega \mathbf{C}_{hm}^F + \mathbf{K}_{hm}^F \right) \mathbf{x}_m(\omega) \quad (15)$$

which enables recovering the hidden variables from the measured ones, if the system flow matrices are known. Then, replacing (15) into (13), the following coupled formulation is obtained in terms of the structural DOF alone, similarly to (4):

$$\left(-\omega^2 \mathbf{M}_{mm}^S + i\omega \mathbf{C}_{mm}^S + \mathbf{K}_{mm}^S \right) \mathbf{x}_m(\omega) + \mathbf{D}_{mm}^{FS}(\omega) \mathbf{x}_m(\omega) = \mathbf{f}_m^{Ext}(\omega) \quad (16)$$

with the following flow-structure interaction force:

$$\begin{aligned} \mathbf{D}_{mm}^{FS}(\omega) = &\left(-\omega^2 \mathbf{M}_{mm}^F + i\omega \mathbf{C}_{mm}^F + \mathbf{K}_{mm}^F \right) \\ &- \left(-\omega^2 \mathbf{M}_{mh}^F + i\omega \mathbf{C}_{mh}^F + \mathbf{K}_{mh}^F \right) \left(-\omega^2 \mathbf{M}_{hh}^F + i\omega \mathbf{C}_{hh}^F + \mathbf{K}_{hh}^F \right)^{-1} \left(-\omega^2 \mathbf{M}_{hm}^F + i\omega \mathbf{C}_{hm}^F + \mathbf{K}_{hm}^F \right) \end{aligned} \quad (17)$$

or, in more compact notation:

$$\mathbf{D}_{mm}^{FS}(\omega) = \mathbf{D}_{mm}^F(\omega) - \mathbf{D}_{mh}^F(\omega) \left(\mathbf{D}_{hh}^F(\omega) \right)^{-1} \mathbf{D}_{hm}^F(\omega) \quad (18)$$

The dynamical coupling matrix $\mathbf{D}_{mm}^{FS}(\omega)$ formulated in (17)-(18) expresses how the structure "feels" the flow, and this general form is relevant for any flow-structure configuration, if the previous assumptions apply. The first term $\mathbf{D}_{mm}^{F}(\omega)=-\omega^2\mathbf{M}_{mm}^{F}+i\omega\mathbf{C}_{mm}^{F}+\mathbf{K}_{mm}^{F}$ stems from the flow-coupling effects directly connected with the measured structural DOF. These are the only relevant terms for systems with highly constrained flows, such as those illustrated in Fig. 3, which therefore typically lead to frequency-independent coupling matrices.

The remaining, more complex terms, stem from the flow dynamics, connected with the flow hidden DOF. Notice in (17)-(18) that the term $\mathbf{D}_{hh}^{F}(\omega)=-\omega^2\mathbf{M}_{hh}^{F}+i\omega\mathbf{C}_{hh}^{F}+\mathbf{K}_{hh}^{F}$, intrinsically related to the flow "internal" DOF, is inverted, while the "mixed" flow-structure coupling terms $\mathbf{D}_{mh}^{F}(\omega)=-\omega^2\mathbf{M}_{mh}^{F}+i\omega\mathbf{C}_{mh}^{F}+\mathbf{K}_{mh}^{F}$ and $\mathbf{D}_{hm}^{F}(\omega)=-\omega^2\mathbf{M}_{hm}^{F}+i\omega\mathbf{C}_{hm}^{F}+\mathbf{K}_{hm}^{F}$ appear in a quadratic manner. Because we have by definition the transfer function $\mathbf{H}_{hh}^{F}(\omega)=\left(\mathbf{D}_{hh}^{F}(\omega)\right)^{-1}$, the result (18) can also be written as:

$$\mathbf{D}_{mm}^{FS}(\omega)=\mathbf{D}_{mm}^{F}(\omega)-\mathbf{D}_{mh}^{F}(\omega)\mathbf{H}_{hh}^{F}(\omega)\mathbf{D}_{hm}^{F}(\omega) \tag{19}$$

and relation (19) demonstrates why the interaction forces expressed by $\mathbf{D}_{mm}^{FS}(\omega)$ are quite complex, even for simple coupled subsystems. The reason is because the modal behavior encapsulated in the flow transfer function $\mathbf{H}_{hh}^{F}(\omega)$, which is possibly the crucial term of the formulation, conveys into the measured $\mathbf{D}_{mm}^{FS}(\omega)$ the dynamical properties of the hidden coupled subsystem. In the framework of the present "flow hidden variables" view, the general mathematical form (17)-(18) applies to any flow-structure configuration, whatever the nature of the system addressed, and this fact stands as a general feature.

At this point, comparing the common flow-structure formulation (3) with the result (17):

$$\begin{aligned}\mathbf{D}_{mm}^{FS}(\omega)&=-\omega^2\mathbf{M}_{mm}^{FS}(\omega)+i\omega\mathbf{C}_{mm}^{FS}(\omega)+\mathbf{K}_{mm}^{FS}(\omega)\\&=\left(-\omega^2\mathbf{M}_{mm}^{F}+i\omega\mathbf{C}_{mm}^{F}+\mathbf{K}_{mm}^{F}\right)\\&\quad-\left(-\omega^2\mathbf{M}_{mh}^{F}+i\omega\mathbf{C}_{mh}^{F}+\mathbf{K}_{mh}^{F}\right)\left(-\omega^2\mathbf{M}_{hh}^{F}+i\omega\mathbf{C}_{hh}^{F}+\mathbf{K}_{hh}^{F}\right)^{-1}\left(-\omega^2\mathbf{M}_{hm}^{F}+i\omega\mathbf{C}_{hm}^{F}+\mathbf{K}_{hm}^{F}\right)\end{aligned} \tag{20}$$

it becomes clear that no easy correspondence between $\mathbf{M}_{mm}^{FS}(\omega)$, $\mathbf{C}_{mm}^{FS}(\omega)$, $\mathbf{K}_{mm}^{FS}(\omega)$ and the frequency-independent flow-coupling matrices in (12) and (17) may be found. Also, it is clear from (20) that the flow-coupling matrices $\mathbf{M}_{mm}^{FS}(\omega)$, $\mathbf{C}_{mm}^{FS}(\omega)$, $\mathbf{K}_{mm}^{FS}(\omega)$ are the result of complex dynamical interactions within the flow-structure system, invalidating the supposed "pure" inertia, damping and stiffness nature of such operators. One must therefore be careful when attempting a physical interpretation of them, from specific test results.

Formulation (12) can only be useful if a proper strategy is devised for the identification of all the flow matrices. That crucial aspect will be addressed in section 4.

3.2 Flow-structure equations in the time-domain

Time-domain computations also become very straightforward, from the standard formulation stemming directly from (12):

$$\begin{bmatrix}\mathbf{M}_{mm}^{S}+\mathbf{M}_{mm}^{F} & \mathbf{M}_{mh}^{F}\\ \mathbf{M}_{hm}^{F} & \mathbf{M}_{hh}^{F}\end{bmatrix}\begin{Bmatrix}\ddot{\mathbf{x}}_m(t)\\ \ddot{\mathbf{x}}_h(t)\end{Bmatrix}+\begin{bmatrix}\mathbf{C}_{mm}^{S}+\mathbf{C}_{mm}^{F} & \mathbf{C}_{mh}^{F}\\ \mathbf{C}_{hm}^{F} & \mathbf{C}_{hh}^{F}\end{bmatrix}\begin{Bmatrix}\dot{\mathbf{x}}_m(t)\\ \dot{\mathbf{x}}_h(t)\end{Bmatrix}+\begin{bmatrix}\mathbf{K}_{mm}^{S}+\mathbf{K}_{mm}^{F} & \mathbf{K}_{mh}^{F}\\ \mathbf{K}_{hm}^{F} & \mathbf{K}_{hh}^{F}\end{bmatrix}\begin{Bmatrix}\mathbf{x}_m(t)\\ \mathbf{x}_h(t)\end{Bmatrix}=\begin{Bmatrix}\mathbf{f}_m^{Ext}(t)\\ \mathbf{0}_h\end{Bmatrix} \tag{21}$$

3.3 Flow-structure eigen-formulation

From equation (21), with $\mathbf{f}_m^{Ext}(t)\equiv\mathbf{0}_m$, the coupled system complex modes are easily computed through a standard eigen-formulation by seeking solutions of the form:

$$\begin{Bmatrix}\mathbf{x}_m(t)\\ \mathbf{x}_h(t)\end{Bmatrix}=\begin{Bmatrix}\boldsymbol{\phi}_m\\ \boldsymbol{\phi}_h\end{Bmatrix}_{(n)}\exp\left(\lambda_{(n)}t\right)\quad;\quad\lambda_{(n)}=\sigma_{(n)}+i\omega_{(n)} \tag{22}$$

for $(n)=1,2,\cdots,N$, leading to the eigen-problem:

$$\left(\lambda_{(n)}^2\begin{bmatrix}\mathbf{M}_{mm}^S+\mathbf{M}_{mm}^F & \mathbf{M}_{mh}^F\\ \mathbf{M}_{hm}^F & \mathbf{M}_{hh}^F\end{bmatrix}+\lambda_{(n)}\begin{bmatrix}\mathbf{C}_{mm}^S+\mathbf{C}_{mm}^F & \mathbf{C}_{mh}^F\\ \mathbf{C}_{hm}^F & \mathbf{C}_{hh}^F\end{bmatrix}+\begin{bmatrix}\mathbf{K}_{mm}^S+\mathbf{K}_{mm}^F & \mathbf{K}_{mh}^F\\ \mathbf{K}_{hm}^F & \mathbf{K}_{hh}^F\end{bmatrix}\right)\begin{Bmatrix}\boldsymbol{\phi}_m\\ \boldsymbol{\phi}_h\end{Bmatrix}_{(n)}=\begin{Bmatrix}\mathbf{0}_m\\ \mathbf{0}_h\end{Bmatrix} \tag{23}$$

or, written compactly as:

$$\left(\lambda_{(n)}^2\mathbf{M}_{m+h}^{S+F}+\lambda_{(n)}\mathbf{C}_{m+h}^{S+F}+\mathbf{K}_{m+h}^{S+F}\right)\left\{\boldsymbol{\phi}_{m+h}\right\}_{(n)}=\left\{\mathbf{0}_{m+h}\right\} \tag{24}$$

from which the system stability is inferred as discussed before. Classically, the quadratic eigen-problem (23)-(24) is converted into an equivalent linear one of twice the size, see for instance Ginsberg (2001), for which the numerical eigen-solution is standard:

$$\left(\lambda_{(n)}\begin{bmatrix}\mathbf{C}_{m+h}^{S+F} & \mathbf{M}_{m+h}^{S+F}\\ \mathbf{M}_{m+h}^{S+F} & \mathbf{0}\end{bmatrix}+\begin{bmatrix}\mathbf{K}_{m+h}^{S+F} & \mathbf{0}\\ \mathbf{0} & -\mathbf{M}_{m+h}^{S+F}\end{bmatrix}\right)\begin{Bmatrix}\left\{\boldsymbol{\phi}_{m+h}\right\}_{(n)}\\ \lambda_{(n)}\left\{\boldsymbol{\phi}_{m+h}\right\}_{(n)}\end{Bmatrix}=\begin{Bmatrix}\mathbf{0}_{m+h}\\ \mathbf{0}_{m+h}\end{Bmatrix} \tag{25}$$

4. Identification of the second-order flow-coupling submatrices from experiments

The frequency-dependent fluidelastic matrix being typically obtained through experiments, the frequency-independent flow matrices of formulation (12) must be inferred from the dynamical data encapsulated in the measured matrix $\hat{\mathbf{D}}_{mm}^{FS}(\omega)$. One may assume that, by choosing an adequate number H of flow hidden DOF, a second-order flow formulation can be found such that, using the identified coefficient matrices, the experimental $\hat{\mathbf{D}}_{mm}^{FS}(\omega)$ is reproduced through condition (17). This section deals with the identification of the matrices in (12) that stand for the fluidelastic forces.

The problem of model coefficients identification from dynamical measurements is not new. An extensive literature exists since the fifties in the field of Network Synthesis, initiated for designing electronic circuits with given component assembling topologies and response specifications, see Guillemin (1951, 1957) and more recent work in books by Anderson and Vongpanitlerd (1973), Daryanani (1976) or Bhattacharya and Singh (2015). Transposition of these design methods to assemblies of mechanical components with targeted responses $\mathbf{H}_{mm}(\omega)$ introduces a non-trivial feature concerning the inertia terms, as elucidated by Goyder (2012), see also the books by Morelli and Smith (2019) and Chen et al. (2020). Relevant identification results along this line of work were produced by Wolf (1991, 1994) and Paronesso and Wolf (1995), in the field of soil-structure interaction. Coefficient identification methods may either operate using directly second-order formulations, or else by making use of first-order state-space formulations, for which several equivalent canonical realizations exist. Although conversion between second-order and state-space models is an immediate exercise, the reverse conversion is far from trivial, though techniques have been developed, see Friswell (1999), Lus et al. (2003a, 2003b) and Houlston (2006).

All the previously discussed identification methods share with the one adopted here standard mathematical techniques such as rational polynomial functions and partial fraction expansions. However, as mentioned before, the second-order model identification technique expanded in the following is inspired by previous work in the field of viscoelasticity and subsequent work in the field of soil-structure interaction, which deal with formulations close to the present one. The first field is mostly concerned about overdamped dynamics, while in the second field only underdamped behavior is addressed. In flow-coupled vibrations it is plausible to assume that the flow intrinsic dynamics, represented by the hidden variables, will include both types of modal behavior. Physically, the flow non-oscillatory may be connected with the fluid lag responses, in the sense of the quasi-unsteady fluidelastic model by Granger and Païdoussis (1996), while the flow oscillatory behavior is connected with near-periodic vortical

phenomena. Due to formulation similarity, the identification procedure devised by Cottereau et al. (2007) for extracting the coupling matrices is adopted in the present work. Moreover, opposite to the system synthesizing methods previously described, which associate physical component networks to emulate the hidden dynamics, in the method by Cottereau et al. (2007) the hidden dynamics of the augmented model are expressed in modal terms, this being more convenient for highlighting the flow physical phenomena. However, because their technique aims the identification of oscillating hidden dynamics, it will be extended here in order to accommodate both oscillating and non-oscillating modes of the identified equivalent second-order model.

The identification strategy consists of the following steps:

(1) Express the measured fluidelastic matrix in residue/pole form;
(2) Express the model dynamical equations in terms of hidden flow modes;
(3) Identify the unknown flow matrix terms from (1) and (2).

4.1 Expressing the measured fluidelastic matrix in residue/pole form

From experimental results, for a given order H of the hidden model, the measured fluidelastic matrix is written in a classic rational fraction polynomial form, see Richardson and Formenti (1982) or Maia and Silva (1997):

$$\hat{\mathbf{D}}_{mm}^{FS}(\omega) = \frac{\mathbf{N}(\omega;H)}{d(\omega;H)} = \frac{\sum_{m=0}^{2H+2}(i\omega)^m \mathbf{N}_m}{\sum_{n=0}^{2H}(i\omega)^n d_n} \tag{26}$$

where the coefficient of the term $(i\omega)^{2H}$ is postulated as $d_{2H}=1$ and the polynomials in m and n are of even order by construction, as we aim to build a second-order formulation. It will become clear in the following that the equivalence between experimental results $\hat{\mathbf{D}}_{mm}^{FS}(\omega)$ and their intended model (17) implies that the numerator expansion of (26) should be two orders higher than the denominator expansion. In other words, $\mathbf{N}(\omega;H)/d(\omega;H)$ in (26) is an improper formulation, the numerator order being higher than the denominator order, as it must be because (26) emulates a dynamical matrix. Notice that the identification procedures described in this section equally apply to models defined in terms of the physical frequency ω or the reduced frequency $\bar{\omega}$. We will use physical frequency for the illustrative mechanical examples of section 5, while the fluidelastic force identified in section 7 is defined in terms of the reduced frequency. Therefore, the circular frequency in equations (26) to (48) should be perceived as being ω or $\bar{\omega}$ according to the context.

The coefficients d_n and coefficient matrices $\mathbf{N}_m$ of the expansions in (26) can be identified from the measured matrix $\hat{\mathbf{D}}_{mm}^{FS}(\omega)$ using numerical methods that are fairly mature today, although far from a closed topic, see Ljung (1999), Isermann and Münchhof (2011) or Pintelon and Schoukens (2012). We now briefly explain the main features of the identification algorithm used, which is based on the work of Ozdemir and Gumussoy (2017). Basically, the unknown coefficients of the polynomials $d(\omega;H)$ and $\mathbf{N}(\omega;H)$ are searched in order to minimize the Frobenius norm of the functional:

$$J\left(d_n, \mathbf{N}_m; H\right) = \left\| w(\omega)\left(\hat{\mathbf{D}}_{mm}^{FS}(\omega) - \frac{\mathbf{N}(\omega;H)}{d(\omega;H)} \right) \right\|_F \tag{27}$$

where $w(\omega)$ stands for an eventual frequency-weighting function. This is a nonlinear optimization problem, which is solved iteratively, for each iteration k, as:

$$J^{(k)}\left(d_n, \mathbf{N}_m; H\right) = \frac{\left|w(\omega)\right|^2}{\left|d^{(k-1)}(\omega)\right|^2} \left\| d^{(k)}(\omega;H)\,\hat{\mathbf{D}}_{mm}^{FS}(\omega) - \mathbf{N}^{(k)}(\omega;H) \right\|_F \tag{28}$$

which is a sequence of linear least-squares problems, a method initiated by Sanathanan and Koerner (1963), here with the starting value $d^{(0)}(\omega)=1$. In order to improve the numerical condition of the identification problem, the formulation is first converted from the complex plane imaginary axis to the unit disk, through a bilinear mapping. Also, an orthogonal rational basis functions set is used on the unit disk, see Ozdemir and Gumussoy (2017) for details. If model stability is enforced, the unstable poles are "reflected" inside the stability boundary and the resulting solution is refined until minimization of $J^{(k)}\left(d_n,\mathbf{N}_m;H\right)$, a common but not flawless approach. On the other hand, in order to achieve a better compromise between the bias and variance errors tradeoff, the formulation (27) may be regularized via a penalty term added to the solution quadratic norm, the so-called ridge regression, see Rish and Grabarnik (2015):

$$J_r\left(d_n,\mathbf{N}_m;H;\lambda_r\right)=\left\|w(\omega)\left(\hat{\mathbf{D}}_{mm}^{FS}(\omega)-\frac{\mathbf{N}(\omega;H)}{d(\omega;H)}\right)\right\|_F+\lambda_r\left\|\left(d_n,\mathbf{N}_m\right)\right\|_{L2} \tag{29}$$

where λ_r is the penalty weight. Analysis of the convergence error of the approximation (26), as a function of H, enables to assert the optimal order $H=H_{opt}$ of the approximation.

Then, through long polynomial division, we put (26) in the form:

$$\hat{\mathbf{D}}_{mm}^{FS}(\omega)=\mathbf{P}(\omega)+\frac{\mathbf{Q}(\omega)}{d(\omega)}=\sum_{r=0}^{2}(i\omega)^r\mathbf{P}_r+\frac{\sum_{m=0}^{2H-1}(i\omega)^m\mathbf{Q}_m}{\sum_{n=0}^{2H}(i\omega)^n d_n} \tag{30}$$

where $\mathbf{Q}(\omega)/d(\omega)$ is now a strictly proper formulation and the improper nature of $\hat{\mathbf{D}}_{mm}^{FS}(\omega)$ is entirely transferred to the quadratic matrix polynomial $\mathbf{P}(\omega)$.

Referring to the formal equation (18), the polynomial $d(\bar{\omega})$ of formulation (30) is connected with the submatrix $\left(\mathbf{D}_{hh}^{F}(\omega)\right)^{-1}$, with $2H$ poles pertaining to H flow modes, while in broad terms $\mathbf{P}(\omega)$ is connected with submatrix $\mathbf{D}_{mm}^{F}(\omega)$ and $\mathbf{Q}(\omega)$ stems from the product $\mathbf{D}_{mh}^{F}(\omega)\mathbf{D}_{hm}^{F}(\omega)$.

Now, through standard partial fraction decomposition, the rational polynomial part of formulation (30) can be converted into residue-pole form:

$$\hat{\mathbf{D}}_{mm}^{FS}(\omega)=-\omega^2\mathbf{P}_2+i\omega\mathbf{P}_1+\mathbf{P}_0+\sum_{n=1}^{2H}\frac{\mathbf{R}_n}{i\omega-\lambda_n}\quad;\quad\begin{cases}\lambda_n=\sigma_n+i\omega_n\\ \mathbf{R}_n=\mathbf{S}_n+i\mathbf{T}_n\end{cases} \tag{31}$$

and we will assume that, among the $2H$ poles, there are $2H_R$ real poles and $2H_C$ complex conjugate poles, with $H=H_R+H_C$. To obtain the mathematical forms (26) and (31), the Matlab functions "*tfest*" and "*residue*" were used, respectively, for increasing values of the model order $2H$.

Pairing the λ_n in groups of real poles and complex conjugate poles, we write the modal development (31) as:

$$\hat{\mathbf{D}}_{mm}^{FS}(\omega)=-\omega^2\mathbf{P}_2+i\omega\mathbf{P}_1+\mathbf{P}_0+\sum_{n=1}^{H_R}\left(\frac{\mathbf{S}_n^{(1)}}{i\omega-\sigma_n^{(1)}}+\frac{\mathbf{S}_n^{(2)}}{i\omega-\sigma_n^{(2)}}\right)+\sum_{n=H_R+1}^{H}\left(\frac{\mathbf{R}_n}{i\omega-\lambda_n}+\frac{\mathbf{R}_n^{*}}{i\omega-\lambda_n^{*}}\right) \tag{32}$$

where the star notation stands for the complex conjugate. Developing each modal pair within the sums of (32), one obtains for the non-oscillating modes:

$$\frac{\mathbf{S}_n^{(1)}}{i\omega-\sigma_n^{(1)}}+\frac{\mathbf{S}_n^{(2)}}{i\omega-\sigma_n^{(2)}}=\frac{-\left(\sigma_n^{(2)}\mathbf{S}_n^{(1)}+\sigma_n^{(1)}\mathbf{S}_n^{(2)}\right)+i\omega\left(\mathbf{S}_n^{(1)}+\mathbf{S}_n^{(2)}\right)}{-\omega^2-i\omega\left(\sigma_n^{(1)}+\sigma_n^{(2)}\right)+\sigma_n^{(1)}\sigma_n^{(2)}} \tag{33}$$

and for the oscillating modes:

$$\frac{\mathbf{R}_n}{i\omega-\lambda_n}+\frac{\mathbf{R}_n^{*}}{i\omega-\lambda_n^{*}}=\frac{\mathbf{S}_n+i\mathbf{T}_n}{i\omega-\left(\sigma_n+i\omega_n\right)}+\frac{\mathbf{S}_n-i\mathbf{T}_n}{i\omega-\left(\sigma_n-i\omega_n\right)}=2\frac{-\left(\sigma_n\mathbf{S}_n+\omega_n\mathbf{T}_n\right)+i\omega\mathbf{S}_n}{-\omega^2-2i\omega\sigma_n+\sigma_n^2+\omega_n^2} \tag{34}$$

hence, from (32)-(34), the experimental results are expressed as:

$$\hat{\mathbf{D}}_{mm}^{FS}(\omega) = -\omega^2\mathbf{P}_2 + i\omega\mathbf{P}_1 + \mathbf{P}_0 + \sum_{n=1}^{H_R} \frac{-\left(\sigma_n^{(2)}\mathbf{S}_n^{(1)} + \sigma_n^{(1)}\mathbf{S}_n^{(2)}\right) + i\omega\left(\mathbf{S}_n^{(1)} + \mathbf{S}_n^{(2)}\right)}{-\omega^2 - i\omega\left(\sigma_n^{(1)} + \sigma_n^{(2)}\right) + \sigma_n^{(1)}\sigma_n^{(2)}} + \sum_{n=H_R+1}^{H} 2\frac{-\left(\sigma_n\mathbf{S}_n + \omega_n\mathbf{T}_n\right) + i\omega\mathbf{S}_n}{-\omega^2 - 2i\omega\sigma_n + \sigma_n^2 + \omega_n^2} \quad (35)$$

4.2 Expressing the model dynamical equations in terms of hidden flow modes

We now turn to the expression of the theoretical dynamical fluidelastic matrix (17). As pointed by Cottereau et al. (2007), identification of the model matrices pertaining to the hidden dynamics has many different but equivalent solutions which, for a given number of "hidden" flow variables, approach the measured matrix $\hat{\mathbf{D}}_{mm}^{FS}(\omega)$. Then, among those possible solutions, it seems a sensible choice to opt for a formulation that implies a minimum of coefficients to identify. Hence the decision to model the flow "hidden" dynamics in terms of flow modes, leading to diagonal matrices $\boldsymbol{M}_{hh}^F$, $\boldsymbol{C}_{hh}^F$ and $\boldsymbol{K}_{hh}^F$, a choice that is also suggested by the form of (35) and leads to an easier physical interpretation. Therefore we will represent the flow matrices in terms of the flow modal parameters (e.g., the flow with rigid structural boundaries) and emphasize this by writing the italicized quantities $\boldsymbol{D}_{hh}^F(\omega) = -\omega^2\boldsymbol{M}_{hh}^F + i\omega\boldsymbol{C}_{hh}^F + \boldsymbol{K}_{hh}^F$, so that (12) reads:

$$\left(-\omega^2\begin{bmatrix}\mathbf{M}_{mm}^S + \mathbf{M}_{mm}^F & \mathbf{M}_{mh}^F \\ \mathbf{M}_{hm}^F & \boldsymbol{M}_{hh}^F\end{bmatrix} + i\omega\begin{bmatrix}\mathbf{C}_{mm}^S + \mathbf{C}_{mm}^F & \mathbf{C}_{mh}^F \\ \mathbf{C}_{hm}^F & \boldsymbol{C}_{hh}^F\end{bmatrix} + \begin{bmatrix}\mathbf{K}_{mm}^S + \mathbf{K}_{mm}^F & \mathbf{K}_{mh}^F \\ \mathbf{K}_{hm}^F & \boldsymbol{K}_{hh}^F\end{bmatrix}\right)\begin{Bmatrix}\mathbf{x}_m(\omega) \\ \mathbf{x}_h(\omega)\end{Bmatrix} = \begin{Bmatrix}\mathbf{f}_m^{Ext}(\omega) \\ \mathbf{0}_h\end{Bmatrix} \quad (36)$$

and therefore (17) as:

$$\mathbf{D}_{mm}^{FS}(\omega) = \left(-\omega^2\mathbf{M}_{mm}^F + i\omega\mathbf{C}_{mm}^F + \mathbf{K}_{mm}^F\right) - \left(-\omega^2\mathbf{M}_{mh}^F + i\omega\mathbf{C}_{mh}^F + \mathbf{K}_{mh}^F\right)\left(-\omega^2\boldsymbol{M}_{hh}^F + i\omega\boldsymbol{C}_{hh}^F + \boldsymbol{K}_{hh}^F\right)^{-1}\left(-\omega^2\mathbf{M}_{hm}^F + i\omega\mathbf{C}_{hm}^F + \mathbf{K}_{hm}^F\right) \quad (37)$$

where the diagonal flow matrices in $\boldsymbol{D}_{hh}^F(\omega)$ are built from the modal coefficients m_n, c_n and k_n, to be identified from the denominator parameters of (35). And, for a given order H, expression (37) is written in terms of the modal series:

$$\mathbf{D}_{mm}^{FS}(\omega) = \left(-\omega^2\mathbf{M}_{mm}^F + i\omega\mathbf{C}_{mm}^F + \mathbf{K}_{mm}^F\right) - \sum_{n=1}^{H}\frac{\left(-\omega^2\hat{\mathbf{m}}_n + i\omega\hat{\mathbf{c}}_n + \hat{\mathbf{k}}_n\right)\left(-\omega^2\breve{\mathbf{m}}_n + i\omega\breve{\mathbf{c}}_n + \breve{\mathbf{k}}_n\right)}{-\omega^2 m_n + i\omega c_n + k_n} \quad (38)$$

where $\hat{\mathbf{m}}_n$, $\hat{\mathbf{c}}_n$ and $\hat{\mathbf{k}}_n$ are matrix columns $M\times 1$ such that:

$$\mathbf{M}_{mh} = \left[\hat{\mathbf{m}}_1\ \hat{\mathbf{m}}_2\cdots\hat{\mathbf{m}}_N\right] \quad ; \quad \mathbf{C}_{mh} = \left[\hat{\mathbf{c}}_1\ \hat{\mathbf{c}}_2\cdots\hat{\mathbf{c}}_N\right] \quad ; \quad \mathbf{K}_{mh} = \left[\hat{\mathbf{k}}_1\ \hat{\mathbf{k}}_2\cdots\hat{\mathbf{k}}_N\right] \quad (39)$$

and $\breve{\mathbf{m}}_n$, $\breve{\mathbf{c}}_n$ and $\breve{\mathbf{k}}_n$ are matrix lines $1\times M$ such that:

$$\mathbf{M}_{hm} = \begin{bmatrix}\breve{\mathbf{m}}_1 \\ \breve{\mathbf{m}}_2 \\ \vdots \\ \breve{\mathbf{m}}_N\end{bmatrix} \quad ; \quad \mathbf{C}_{hm} = \begin{bmatrix}\breve{\mathbf{c}}_1 \\ \breve{\mathbf{c}}_2 \\ \vdots \\ \breve{\mathbf{c}}_N\end{bmatrix} \quad ; \quad \mathbf{K}_{hm} = \begin{bmatrix}\breve{\mathbf{k}}_1 \\ \breve{\mathbf{k}}_2 \\ \vdots \\ \breve{\mathbf{k}}_N\end{bmatrix} \quad (40)$$

so that we obtain from (38):

$$\mathbf{D}_{mm}^{FS}(\omega) = \left(-\omega^2\mathbf{M}_{mm}^F + i\omega\mathbf{C}_{mm}^F + \mathbf{K}_{mm}^F\right) - \sum_{n=1}^{H}\frac{\omega^4\hat{\mathbf{m}}_n\breve{\mathbf{m}}_n - i\omega^3\left(\hat{\mathbf{m}}_n\breve{\mathbf{c}}_n + \hat{\mathbf{c}}_n\breve{\mathbf{m}}_n\right) - \omega^2\left(\hat{\mathbf{m}}_n\breve{\mathbf{k}}_n + \hat{\mathbf{c}}_n\breve{\mathbf{c}}_n + \hat{\mathbf{k}}_n\breve{\mathbf{m}}_n\right) + i\omega\left(\hat{\mathbf{c}}_n\breve{\mathbf{k}}_n + \hat{\mathbf{k}}_n\breve{\mathbf{c}}_n\right) + \hat{\mathbf{k}}_n\breve{\mathbf{k}}_n}{-\omega^2 m_n + i\omega c_n + k_n} \quad (41)$$

4.3 Identification of the flow matrix terms

Comparison between the rational terms of (35) and (41) shows that one should put modal masses $m_n = 1$ and, in order to establish an equivalence, the numerator terms in ω^4, $i\omega^3$ and

ω^2 must disappear, without destroying the $i\omega$ and constant terms. Using the same principle of economy, to nullify the terms in ω^4 and $i\omega^3$, it is sufficient to postulate that the inertia vector cross-terms are nil, $\widehat{\mathbf{m}}_n = \mathbf{0}_{M\times 1}$ and $\breve{\mathbf{m}}_n = \mathbf{0}_{1\times M}$. With respect to other eventual mathematical solutions of the identification problem, this seems the most logical choice, while preserving the inertial interaction between the flow and the structure in the formulation, through the fluid added mass matrix $\mathbf{M}_{mm}^F$. Therefore, we have:

$$\mathbf{M}_{hh}^F = \boldsymbol{I}_{hh} \quad ; \quad \mathbf{M}_{mh}^F = \mathbf{0}_{mh} \quad ; \quad \mathbf{M}_{hm}^F = \mathbf{0}_{hm} \tag{42}$$

Then, (36), (37) and (41) reduce to:

$$\left(-\omega^2\begin{bmatrix}\mathbf{M}_{mm}^S+\mathbf{M}_{mm}^F & \mathbf{0}_{mh}\\ \mathbf{0}_{hm} & \boldsymbol{I}_{hh}\end{bmatrix}+i\omega\begin{bmatrix}\mathbf{C}_{mm}^S+\mathbf{C}_{mm}^F & \mathbf{C}_{mh}^F\\ \mathbf{C}_{hm}^F & \boldsymbol{C}_{hh}^F\end{bmatrix}+\begin{bmatrix}\mathbf{K}_{mm}^S+\mathbf{K}_{mm}^F & \mathbf{K}_{mh}^F\\ \mathbf{K}_{hm}^F & \boldsymbol{K}_{hh}^F\end{bmatrix}\right)\begin{Bmatrix}\mathbf{x}_m(\omega)\\ \mathbf{q}_h(\omega)\end{Bmatrix}=\begin{Bmatrix}\mathbf{f}_m^{Ext}(\omega)\\ \mathbf{0}_h\end{Bmatrix} \tag{43}$$

and:

$$\mathbf{D}_{mm}^{FS}(\omega)=\left(-\omega^2\mathbf{M}_{mm}^F+i\omega\mathbf{C}_{mm}^F+\mathbf{K}_{mm}^F\right)-\left(i\omega\mathbf{C}_{mh}^F+\mathbf{K}_{mh}^F\right)\left(-\omega^2\boldsymbol{I}_{hh}+i\omega\boldsymbol{C}_{hh}^F+\boldsymbol{K}_{hh}^F\right)^{-1}\left(i\omega\mathbf{C}_{hm}^F+\mathbf{K}_{hm}^F\right) \tag{44}$$

hence:

$$\mathbf{D}_{mm}^{FS}(\omega)=\left(-\omega^2\mathbf{M}_{mm}^F+i\omega\mathbf{C}_{mm}^F+\mathbf{K}_{mm}^F\right)-\sum_{n=1}^{H}\frac{-\omega^2\widehat{\mathbf{c}}_n\breve{\mathbf{c}}_n+i\omega\left(\widehat{\mathbf{c}}_n\breve{\mathbf{k}}_n+\widehat{\mathbf{k}}_n\breve{\mathbf{c}}_n\right)+\widehat{\mathbf{k}}_n\breve{\mathbf{k}}_n}{-\omega^2+i\omega c_n+k_n} \tag{45}$$

However, to nullify the term in ω^2, one cannot postulate that $\widehat{\mathbf{c}}_n$ and $\breve{\mathbf{c}}_n$ are nil, as that would also nullify the term in $i\omega$ that must be kept. A clever workaround for this difficulty, devised by Cottereau et al. (2007), is to use the identity:

$$\frac{-\omega^2\widehat{\mathbf{c}}_n\breve{\mathbf{c}}_n}{-\omega^2+i\omega c_n+k_n}=\widehat{\mathbf{c}}_n\breve{\mathbf{c}}_n-\frac{\left(i\omega c_n+k_n\right)\widehat{\mathbf{c}}_n\breve{\mathbf{c}}_n}{-\omega^2+i\omega c_n+k_n} \tag{46}$$

and we obtain from (45) with (46):

$$\mathbf{D}_{mm}^{FS}(\omega)=\left(-\omega^2\mathbf{M}_{mm}^F+i\omega\mathbf{C}_{mm}^F+\left(\mathbf{K}_{mm}^F-\sum_{n=1}^{H}\widehat{\mathbf{c}}_n\breve{\mathbf{c}}_n\right)\right)-\sum_{n=1}^{H}\frac{\left(\widehat{\mathbf{k}}_n\breve{\mathbf{k}}_n-k_n\widehat{\mathbf{c}}_n\breve{\mathbf{c}}_n\right)+i\omega\left(\widehat{\mathbf{c}}_n\breve{\mathbf{k}}_n+\widehat{\mathbf{k}}_n\breve{\mathbf{c}}_n-c_n\widehat{\mathbf{c}}_n\breve{\mathbf{c}}_n\right)}{-\omega^2+i\omega c_n+k_n} \tag{47}$$

One may now identify the unknown terms c_n, k_n, $\widehat{\mathbf{k}}_n$, $\widehat{\mathbf{c}}_n$, $\breve{\mathbf{k}}_n$ and $\breve{\mathbf{c}}_n$, with $n=1,2,\cdots,H$, as well as $\mathbf{M}_{mm}^F$, $\mathbf{C}_{mm}^F$ and $\mathbf{K}_{mm}^F$, by comparing the experimentally obtained $\hat{\mathbf{D}}_{mm}^{FS}(\omega)$ expressed in (35) and the corresponding theoretical formulation $\mathbf{D}_{mm}^{FS}(\omega)$ expressed in (47). Starting with the rational terms, we obtain directly the denominator coefficients pertaining to the non-oscillatory and oscillatory modes:

$$\begin{cases}c_n=-\left(\sigma_n^{(1)}+\sigma_n^{(2)}\right)\\ k_n=\sigma_n^{(1)}\sigma_n^{(2)}\end{cases},\quad n=1,\cdots,H_R \quad ; \quad \begin{cases}c_n=-2\sigma_n\\ k_n=\sigma_n^2+\omega_n^2\end{cases},\quad n=H_R+1,\cdots,H \tag{48}$$

Then, for the matrix columns of the numerators, the following equations are obtained from the real and imaginary parts:

$$\widehat{\mathbf{k}}_n\breve{\mathbf{k}}_n-k_n\widehat{\mathbf{c}}_n\breve{\mathbf{c}}_n=\mathbf{A}_n \quad ; \quad \widehat{\mathbf{c}}_n\breve{\mathbf{k}}_n+\widehat{\mathbf{k}}_n\breve{\mathbf{c}}_n-c_n\widehat{\mathbf{c}}_n\breve{\mathbf{c}}_n=\mathbf{B}_n \quad , \quad n=1,\cdots,H \tag{49}$$

which can also be written in matrix form:

$$\begin{bmatrix}\widehat{\mathbf{k}}_n & \widehat{\mathbf{c}}_n\end{bmatrix}\begin{bmatrix}1 & 0\\ 0 & -k_n\end{bmatrix}\begin{bmatrix}\breve{\mathbf{k}}_n\\ \breve{\mathbf{c}}_n\end{bmatrix}=\mathbf{A}_n \quad ; \quad \begin{bmatrix}\widehat{\mathbf{k}}_n & \widehat{\mathbf{c}}_n\end{bmatrix}\begin{bmatrix}0 & 1\\ 1 & -c_n\end{bmatrix}\begin{bmatrix}\breve{\mathbf{k}}_n\\ \breve{\mathbf{c}}_n\end{bmatrix}=\mathbf{B}_n \quad , \quad n=1,\cdots,H \tag{50}$$

with:

$$\begin{cases}\mathbf{A}_n=\sigma_n^{(2)}\mathbf{S}_n^{(1)}+\sigma_n^{(1)}\mathbf{S}_n^{(2)}\\ \mathbf{B}_n=-\left(\mathbf{S}_n^{(1)}+\mathbf{S}_n^{(2)}\right)\end{cases},\quad n=1,\cdots,H_R \quad ; \quad \begin{cases}\mathbf{A}_n=2\left(\sigma_n\mathbf{S}_n+\omega_n\mathbf{T}_n\right)\\ \mathbf{B}_n=-2\mathbf{S}_n\end{cases},\quad n=H_R+1,\cdots,H \tag{51}$$

where $\mathbf{A}_n$ and $\mathbf{B}_n$ are all real matrices. We obtain straightforwardly the matrices of the polynomial term as:

$$\mathbf{M}_{mm}^F=\mathbf{P}_2 \quad ; \quad \mathbf{C}_{mm}^F=\mathbf{P}_1 \quad ; \quad \mathbf{K}_{mm}^F=\mathbf{P}_0+\sum_{n=1}^{H}\widehat{\mathbf{c}}_n\breve{\mathbf{c}}_n \tag{52}$$

the value of $\mathbf{K}_{mm}^{F}$ being computed after all the $\widehat{\mathbf{c}}_n$ and $\breve{\mathbf{c}}_n$ are identified, for $n=1,2,\cdots,H$. The only remaining difficulty is solving the equation system (49) or (50) with (51), for the columns $\widehat{\mathbf{k}}_n$ and $\widehat{\mathbf{c}}_n$ of matrices (39) and the lines $\breve{\mathbf{k}}_n$ and $\breve{\mathbf{c}}_n$ of matrices (40). In a related problem, Cottereau et al. (2007) managed to find the analytical solution of system (49), for the case of oscillatory modes of symmetrically coupled systems, using the Takagi (1924) factorization, which is applicable to any symmetric matrix. However, their approach does not seem directly applicable to the general case of non-oscillating modes, neither to non-symmetric coupling matrices.

The identification problem (49)-(50) presents considerable difficulties in the general case of matrices without any specific structure. Here, we will develop a solution for both the non-oscillating an oscillating modes, in the important specific case of symmetric coupling. It is understood that anti-symmetric coupling is also a case of practical significance, however research for extending the present identification approach to the general coupling case is still ongoing and will be reported in a forthcoming paper. Nonetheless, the specific identification method detailed here applies to the two illustrative examples of section 5, as well as to the fluidelastic data adressed in section 7, which stems from a single vibrating tube.

In the specific case of systems with symmetric coupling, one has $\widehat{\mathbf{k}}_n=\mathbf{k}_n$, $\breve{\mathbf{k}}_n=\mathbf{k}_n^T$, $\widehat{\mathbf{c}}_n=\mathbf{c}_n$ and $\breve{\mathbf{c}}_n=\mathbf{c}_n^T$, so that (49)-(50) lead to:

$$\mathbf{k}_n\mathbf{k}_n^T-k_n\mathbf{c}_n\mathbf{c}_n^T=\mathbf{A}_n \quad ; \quad \mathbf{c}_n\mathbf{k}_n^T+\mathbf{k}_n\mathbf{c}_n^T-c_n\mathbf{c}_n\mathbf{c}_n^T=\mathbf{B}_n \quad , \quad n=1,\cdots,H \tag{53}$$

and:

$$\begin{bmatrix}\mathbf{k}_n & \mathbf{c}_n\end{bmatrix}\begin{bmatrix}1 & 0\\ 0 & -k_n\end{bmatrix}\begin{bmatrix}\mathbf{k}_n^T\\ \mathbf{c}_n^T\end{bmatrix}=\mathbf{A}_n \quad ; \quad \begin{bmatrix}\mathbf{k}_n & \mathbf{c}_n\end{bmatrix}\begin{bmatrix}0 & 1\\ 1 & -c_n\end{bmatrix}\begin{bmatrix}\mathbf{k}_n^T\\ \mathbf{c}_n^T\end{bmatrix}=\mathbf{B}_n \quad , \quad n=1,\cdots,H \tag{54}$$

where, obviously, $\mathbf{A}_n$ and $\mathbf{B}_n$ are symmetric matrices. Details of the proposed solution for finding the vectors $\mathbf{k}_n$ and $\mathbf{c}_n$ ($n=1,\cdots,H$) are presented in the Appendix.

5. Two illustrative validating examples

Before dealing with the actual flow-structure problem, let us test the described formulation and identification procedure on two simple structural systems, shown in Fig. 5. Here, for computing the reference dynamical "measurements", the physical parameters of the systems are obviously known. However, the identification procedure just presented will be applied as if such parameters were unknown, in order to test and validate the proposed modelling approach. In these examples, the dynamics of the coupled substructures (shown in blue) stand for the "flow" of real-life flow-structure coupled systems. The first system (a) consists of a single measured oscillator coupled to a hidden multi-degree of freedom (MDOF) substructure, while the second system (b) consists of two measured oscillators coupled through a hidden single-degree of freedom (SDOF) substructure. When applying the preceding formulation to these structural examples, we use in this section the superscript (*C*), instead of (*F*), to designate the coupled subsystem that stands for the "flow", therefore the reference "measured" coupling matrix is denoted $\hat{\mathbf{D}}_{mm}^{CS}(\omega)$ and the corresponding theoretical formulation $\mathbf{D}_{mm}^{CS}(\omega)$.

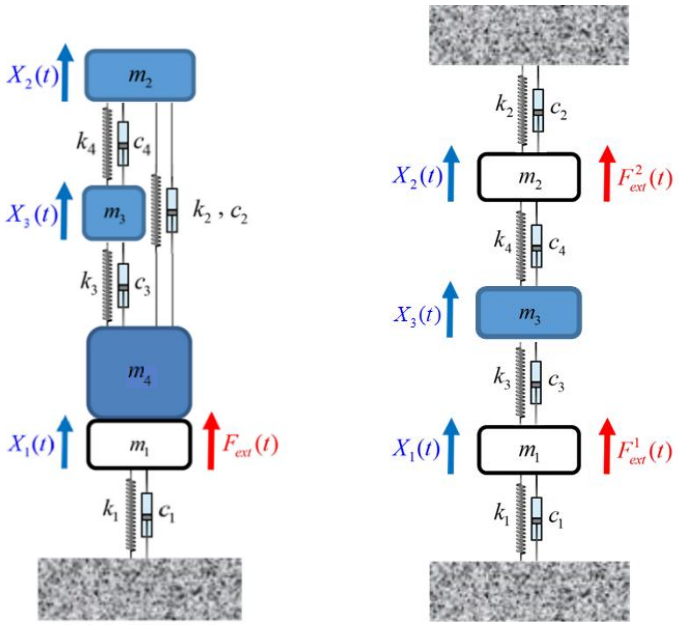

(a) (b)

Fig. 5. Illustrative structural examples for which the coupled subsystems entail additional hidden degrees of freedom: (a) SDOF measured structure coupled to MDOF hidden dynamics; (b) MDOF measured structure coupled to SDOF hidden dynamics.

5.1 SDOF structure coupled to MDOF hidden dynamics

With respect to the coupled system shown in Fig. 5 (a), we will assume that X_1 is the measured variable, associated to the oscillator with parameters (m_1, c_1, k_1), while X_2 and X_3 are hidden variables, associated with the coupled substructure. The system dynamics are simply formulated in the frequency domain as:

$$\left(-\omega^2\begin{bmatrix} m_1+m_4 & \begin{bmatrix}0 & 0\end{bmatrix} \\ \begin{bmatrix}0\\0\end{bmatrix} & \begin{bmatrix} m_2 & 0 \\ 0 & m_3 \end{bmatrix}\end{bmatrix} + i\omega\begin{bmatrix} c_1+c_2+c_3 & \begin{bmatrix}-c_2 & -c_3\end{bmatrix} \\ \begin{bmatrix}-c_2\\-c_3\end{bmatrix} & \begin{bmatrix} c_2+c_4 & -c_4 \\ -c_4 & c_3+c_4 \end{bmatrix}\end{bmatrix} + \begin{bmatrix} k_1+k_2+k_3 & \begin{bmatrix}-k_2 & -k_3\end{bmatrix} \\ \begin{bmatrix}-k_2\\-k_3\end{bmatrix} & \begin{bmatrix} k_2+k_4 & -k_4 \\ -k_4 & k_3+k_4 \end{bmatrix}\end{bmatrix}\right)\left\{\begin{matrix} X_1(\omega) \\ \left\{\begin{matrix} X_2(\omega) \\ X_3(\omega)\end{matrix}\right\}\end{matrix}\right\} = \left\{\begin{matrix} F_{ext}(\omega) \\ \left\{\begin{matrix}0\\0\end{matrix}\right\}\end{matrix}\right\} \quad (55)$$

where the various submatrices of the general equation (12) are easily recognized. Then, the coordinate transformation, between the hidden and the measured DOF is obtained:

$$\left\{\begin{matrix} X_2(\omega) \\ X_3(\omega)\end{matrix}\right\} = \left(-\omega^2\begin{bmatrix} m_2 & 0 \\ 0 & m_3 \end{bmatrix} + i\omega\begin{bmatrix} c_2+c_4 & -c_4 \\ -c_4 & c_3+c_4 \end{bmatrix} + \begin{bmatrix} k_2+k_4 & -k_4 \\ -k_4 & k_3+k_4 \end{bmatrix}\right)^{-1}\left(i\omega\begin{bmatrix} c_2 \\ c_3 \end{bmatrix} + \begin{bmatrix} k_2 \\ k_3 \end{bmatrix}\right) X_1(\omega) \quad (56)$$

and, from the first equation (55) with (56), one obtains:

$$\left(-\omega^2 m_1 + i\omega c_1 + k_1\right) X_1(\omega) = F_{ext}(\omega) + F_c(\omega) \quad (57)$$

with the coupling force:

$$F_c(\omega) = -D_{11}^{CS}(\omega) X_1(\omega) \quad (58)$$

as well as the dynamical coupling matrix (here a single function), with the coupled system dynamics condensed in the measured DOF X_1:

$$\hat{D}_{11}^{CS}(\omega)=\left(-\omega^2 m_4+i\omega\left(c_2+c_3\right)+\left(k_2+k_3\right)\right)$$
$$-\left(i\omega\begin{bmatrix}c_2\\c_3\end{bmatrix}+\begin{bmatrix}k_2\\k_3\end{bmatrix}\right)^T\left(-\omega^2\begin{bmatrix}m_2&0\\0&m_3\end{bmatrix}+i\omega\begin{bmatrix}c_2+c_4&-c_4\\-c_4&c_3+c_4\end{bmatrix}+\begin{bmatrix}k_2+k_4&-k_4\\-k_4&k_3+k_4\end{bmatrix}\right)^{-1}\left(i\omega\begin{bmatrix}c_2\\c_3\end{bmatrix}+\begin{bmatrix}k_2\\k_3\end{bmatrix}\right) \quad (59)$$

where the various submatrices of the general formulation (17) are recognized. Formulation (59) will be used to generate the pseudo-experimental data, hence the "hat" notation $\hat{D}_{11}^{CS}(\omega)$.

We thus turn to the identification problem and, following the procedure described in section 5, we assume that the hidden subsystem to identify has the general structure of equation (43):

$$\left(-\omega^2\begin{bmatrix}m_1+m_{mm}^1&\begin{bmatrix}0&\cdots&0\end{bmatrix}\\\begin{bmatrix}0\\\vdots\\0\end{bmatrix}&\begin{bmatrix}1&\cdots&0\\\vdots&\ddots&\vdots\\0&\cdots&1\end{bmatrix}\end{bmatrix}+i\omega\begin{bmatrix}c_1+c_{mm}^1&\begin{bmatrix}c_{mh}^1&\cdots&c_{mh}^H\end{bmatrix}\\\begin{bmatrix}c_{mh}^1\\\vdots\\c_{mh}^H\end{bmatrix}&\begin{bmatrix}c_{hh}^1&\cdots&0\\\vdots&\ddots&\vdots\\0&\cdots&c_{hh}^H\end{bmatrix}\end{bmatrix}+\begin{bmatrix}k_1+k_{mm}^1&\begin{bmatrix}k_{mh}^1&\cdots&k_{mh}^H\end{bmatrix}\\\begin{bmatrix}k_{mh}^1\\\vdots\\k_{mh}^H\end{bmatrix}&\begin{bmatrix}k_{hh}^1&\cdots&0\\\vdots&\ddots&\vdots\\0&\cdots&k_{hh}^H\end{bmatrix}\end{bmatrix}\right)\begin{Bmatrix}X_1(\omega)\\\begin{Bmatrix}Q_h^1(\omega)\\\vdots\\Q_h^H(\omega)\end{Bmatrix}\end{Bmatrix}=\begin{Bmatrix}F_{ext}(\omega)\\\begin{Bmatrix}0\\\vdots\\0\end{Bmatrix}\end{Bmatrix} \quad (60)$$

and of equation (44), with the optimal order H still to be established:

$$D_{mm}^{CS}(\omega)=\left(-\omega^2 m_{mm}^1+i\omega c_{mm}^1+k_{mm}^1\right)$$
$$-\left(i\omega\begin{bmatrix}c_{mh}^1\\\vdots\\c_{mh}^H\end{bmatrix}+\begin{bmatrix}k_{mh}^1\\\vdots\\k_{mh}^H\end{bmatrix}\right)^T\left(-\omega^2\begin{bmatrix}1&\cdots&0\\\vdots&\ddots&\vdots\\0&\cdots&1\end{bmatrix}+i\omega\begin{bmatrix}c_{hh}^1&\cdots&0\\\vdots&\ddots&\vdots\\0&\cdots&c_{hh}^H\end{bmatrix}+\begin{bmatrix}k_{hh}^1&\cdots&0\\\vdots&\ddots&\vdots\\0&\cdots&k_{hh}^H\end{bmatrix}\right)^{-1}\left(i\omega\begin{bmatrix}c_{mh}^1\\\vdots\\c_{mh}^H\end{bmatrix}+\begin{bmatrix}k_{mh}^1\\\vdots\\k_{mh}^H\end{bmatrix}\right) \quad (61)$$

which, following (47), is equivalent to:

$$D_{11}^{CS}(\omega)=\left(-\omega^2 m_{mm}^1+i\omega c_{mm}^1+\left(k_{mm}^1-\sum_{n=1}^{H}\mathbf{c}_{mh}^n\mathbf{c}_{mh}^{nT}\right)\right)$$
$$-\sum_{n=1}^{H}\frac{\left(\mathbf{k}_{mh}^n\mathbf{k}_{mh}^{nT}-k_{hh}^n\mathbf{c}_{mh}^n\mathbf{c}_{mh}^{nT}\right)+i\omega\left(\mathbf{c}_{mh}^n\mathbf{k}_{mh}^{nT}+\mathbf{k}_{mh}^n\mathbf{c}_{mh}^{nT}-c_{hh}^n\mathbf{c}_{mh}^n\mathbf{c}_{mh}^{nT}\right)}{-\omega^2+i\omega c_{hh}^n+k_{hh}^n} \quad (62)$$

For illustration, we assume the following numerical parameters of the coupled subsystem:

$$\begin{cases}m_2=1\text{ kg},\ m_3=2\text{ kg},\ m_4=5\text{ kg}\\c_2=50\text{ Ns/m},\ c_3=100\text{ Ns/m},\ c_4=10\text{ Ns/m}\\k_2=5\times10^6\text{ N/m},\ k_3=10^6\text{ N/m},\ k_4=10^7\text{ N/m}\end{cases}$$

which are replaced into the reference equation (59) in the range $0\le(\omega/2\pi)\le1000$ Hz, sampled at $\Delta\omega/2\pi=10$ Hz (the largest value adequate for defining the system modal peaks), leading to the "measured" response function $\hat{D}_{11}^{CS}(\omega)$. Then, the rational polynomial expansion (26) is fitted to the reference $\hat{D}_{11}^{CS}(\omega)$, for increasing order H, while evaluating the quadratic error of the approximation. The results presented in Fig. 6, which show the decrease and stabilization of the fit error as H increases, clearly point to the optimal value $H=2$, in agreement with the actual order of the "hidden" coupled subsystem of Fig. 5 (a).

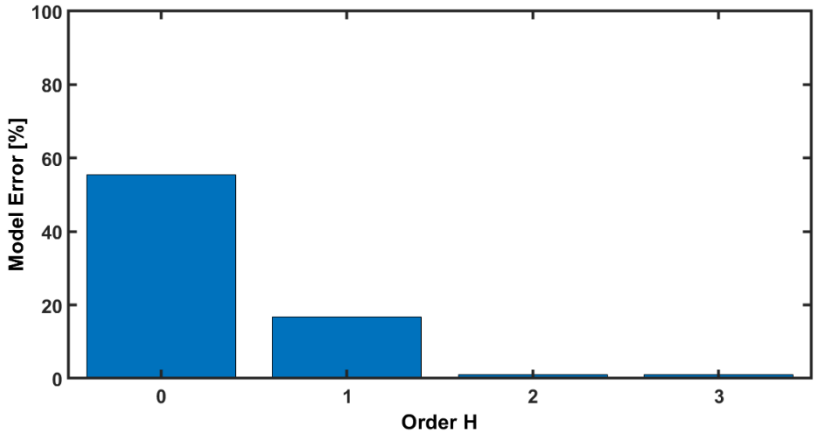

Fig. 6. SDOF structure coupled to MDOF hidden dynamics: Identification error with respect to the "measured" values of $\hat{D}_{11}^{CS}(\omega)$ as a function of the model order H.

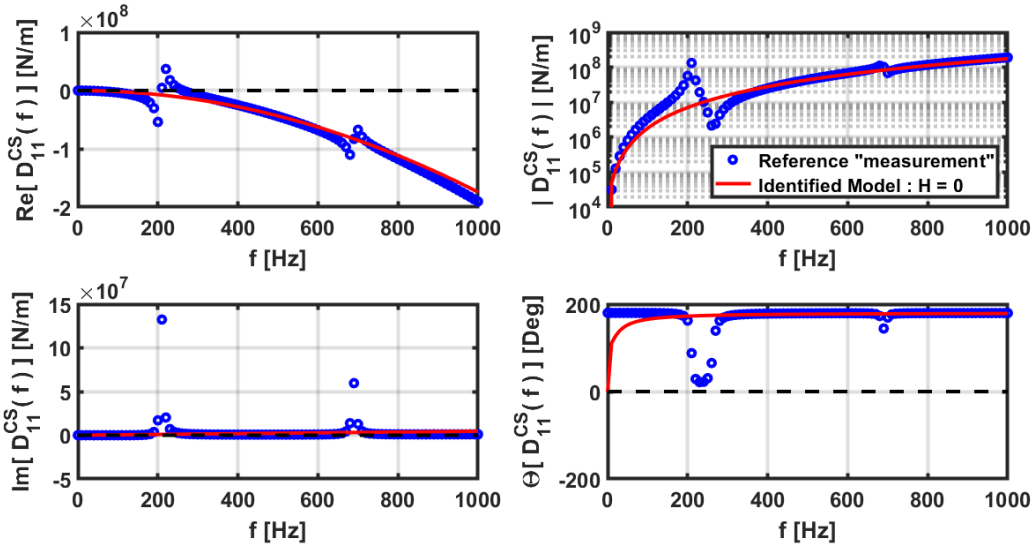

Fig. 7. SDOF structure coupled to MDOF hidden dynamics: Reference "measurement" $\hat{D}_{11}^{CS}(\omega)$ and reconstructed $D_{11}^{CS}(\omega)$ using (61), from the identified model with order $H = 0$.

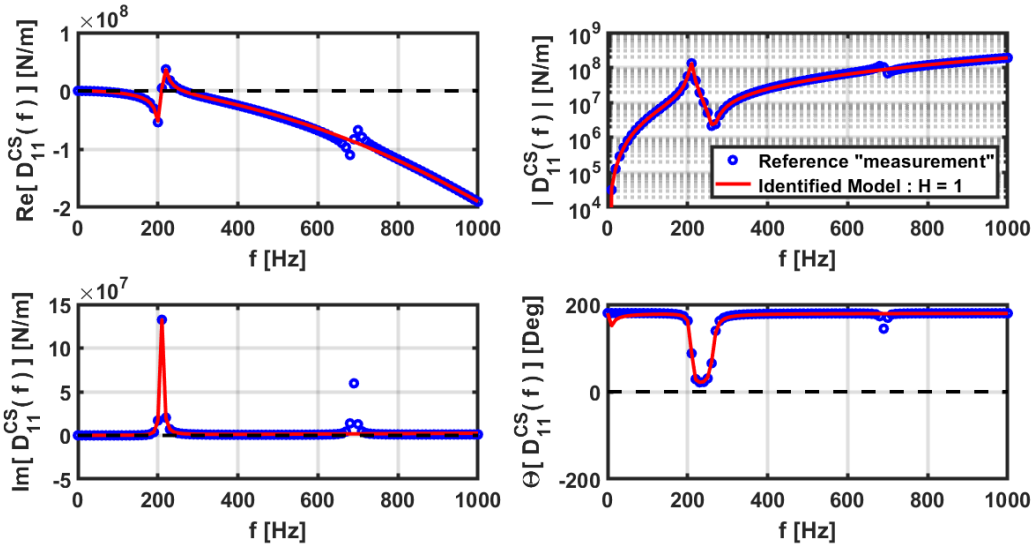

Fig. 8. SDOF structure coupled to MDOF hidden dynamics: Reference "measurement" $\hat{D}_{11}^{CS}(\omega)$ and reconstructed $D_{11}^{CS}(\omega)$ using (61), from the identified model with order $H = 1$.

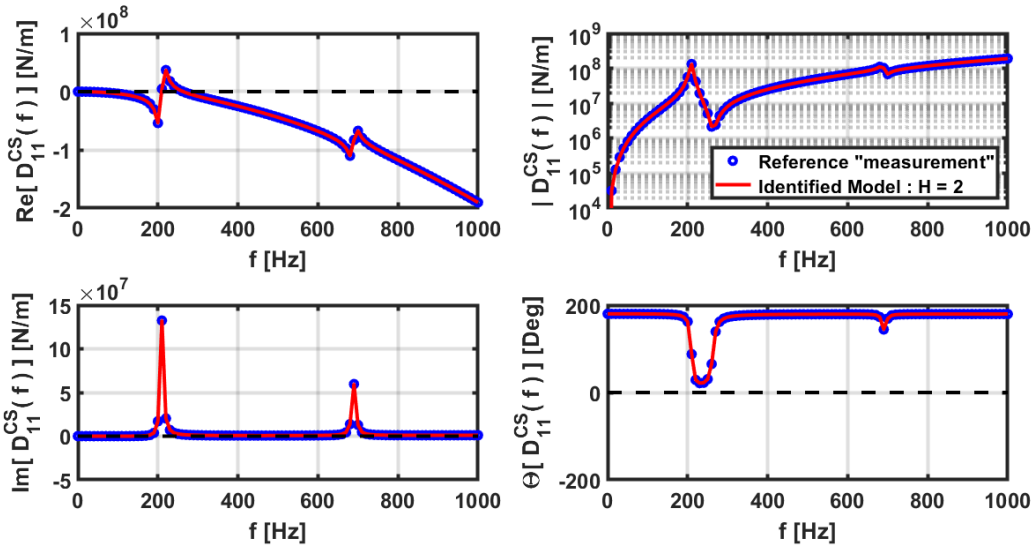

Fig. 9. SDOF structure coupled to MDOF hidden dynamics: Reference "measurement" $\hat{D}_{11}^{CS}(\omega)$ and reconstructed $D_{11}^{CS}(\omega)$ using (61), from the identified model with order $H=2$.

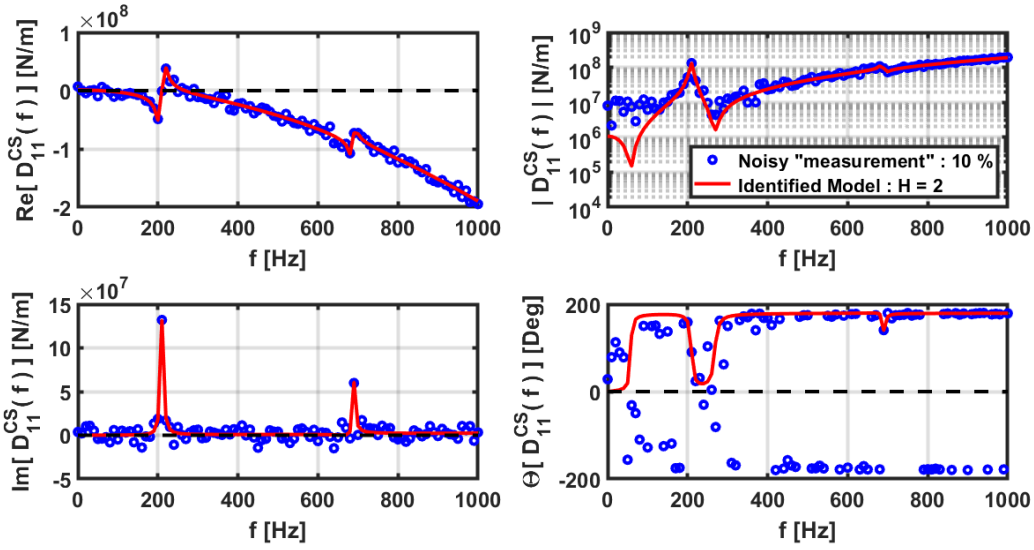

Fig. 10. SDOF structure coupled to MDOF hidden dynamics: Noisy "measurement" $\hat{D}_{11}^{CS}(\omega)$ with 10% noise amplitude and reconstructed $D_{11}^{CS}(\omega)$ using (61), from the identified model with optimal order $H=2$.

The approach presented for the matrices identifications is then applied, leading to the numerical values of the matrix coefficients in the coupled representation (60), and $D_{11}^{CS}(\omega)$ is reconstructed using (61) with the identified parameters. The identification results for increasing order $H=0$, 1 and 2 are presented in Figs. 7 to 9, showing the real and imaginary parts, the magnitude and the phase of $D_{11}^{CS}(\omega)$, respectively. The progressive convergence of the fit is unmistakable, thus validating the identification approach. Also, Fig. 10 presents the results obtained for the optimal order $H=2$, when the "measured" response function $\hat{D}_{11}^{CS}(\omega)$ is polluted by 10 % additive Gaussian noise, emphasising the robustness of the described identification procedure. On the other hand, also from the noisy identification, Fig. 11 presents the model identified poles for increasing order $1 \le H \le 6$, showing that beyond the optimal order $H=2$ the spurious identified poles display an erratic behavior, also leading to unstable poles for $H \ge 4$.

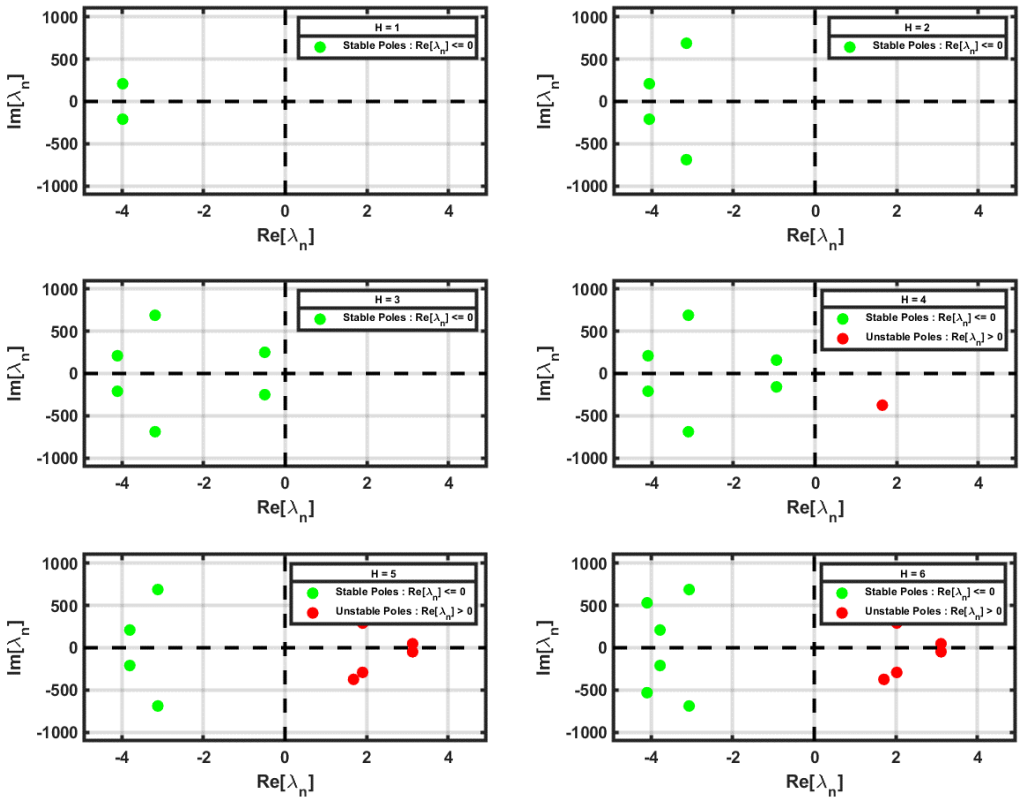

Fig. 11. SDOF structure coupled to MDOF hidden dynamics: Identified poles from the noisy "measurement" $\hat{D}_{11}^{CS}(\omega)$ with 10% noise, as a function of the model order H.

5.2 MDOF structure coupled to SDOF hidden dynamics

The coupled system shown in Fig. 5 (b) reads in the frequency domain:

$$\left(-\omega^2\begin{bmatrix} m_1 & 0 & 0 \\ 0 & m_2 & 0 \\ 0 & 0 & m_3 \end{bmatrix} + i\omega\begin{bmatrix} c_1+c_3 & 0 & -c_3 \\ 0 & c_2+c_4 & -c_4 \\ -c_3 & -c_4 & c_3+c_4 \end{bmatrix} + \begin{bmatrix} k_1+k_3 & 0 & -k_3 \\ 0 & k_2+k_4 & -k_4 \\ -k_3 & k_4 & k_3+k_4 \end{bmatrix}\right)\begin{Bmatrix} X_1(\omega) \\ X_2(\omega) \\ X_3(\omega) \end{Bmatrix} = \begin{Bmatrix} F_{ext}^1(\omega) \\ F_{ext}^2(\omega) \\ 0 \end{Bmatrix} \tag{63}$$

and, from the third equation (63), the following coordinate transformation, between the hidden degree of freedom $X_3(\omega)$ and the measured degrees of freedom $[X_1(\omega), X_2(\omega)]$, is obtained:

$$X_3(\omega) = \left(-\omega^2 m_3 + i\omega\left(c_3+c_4\right)+\left(k_3+k_4\right)\right)^{-1}\left(i\omega\begin{bmatrix} c_3 \\ c_4 \end{bmatrix}+\begin{bmatrix} k_3 \\ k_4 \end{bmatrix}\right)^T \begin{Bmatrix} X_1(\omega) \\ X_2(\omega) \end{Bmatrix} \tag{64}$$

hence, from the first two equations of (63) with (64), one obtains:

$$\left(-\omega^2\begin{bmatrix} m_1 & 0 \\ 0 & m_2 \end{bmatrix} + i\omega\begin{bmatrix} c_1 & 0 \\ 0 & c_2 \end{bmatrix} + \begin{bmatrix} k_1 & 0 \\ 0 & k_2 \end{bmatrix}\right)\begin{Bmatrix} X_1(\omega) \\ X_2(\omega) \end{Bmatrix} = \begin{Bmatrix} F_{ext}^1(\omega) \\ F_{ext}^2(\omega) \end{Bmatrix} + \begin{Bmatrix} F_c^1(\omega) \\ F_c^2(\omega) \end{Bmatrix} \tag{65}$$

with the coupling forces:

$$\begin{Bmatrix} F_c^1(\omega) \\ F_c^2(\omega) \end{Bmatrix} = -\left[\mathbf{D}_{mm}^{CS}(\omega)\right]\begin{Bmatrix} X_1(\omega) \\ X_2(\omega) \end{Bmatrix} \tag{66}$$

where the symmetric coupling matrix (here with 2×2 functions) condenses the coupled system dynamics in the measured DOF X_1 and X_2:

$$\left[\hat{\mathbf{D}}_{mm}^{CS}(\omega)\right]=\left(i\omega\begin{bmatrix}c_3 & 0\\ 0 & c_4\end{bmatrix}+\begin{bmatrix}k_3 & 0\\ 0 & k_4\end{bmatrix}\right)$$
$$-\left(i\omega\begin{bmatrix}c_3\\ c_4\end{bmatrix}+\begin{bmatrix}k_3\\ k_4\end{bmatrix}\right)\left(-\omega^2 m_3+i\omega\left(c_3+c_4\right)+\left(k_3+k_4\right)\right)^{-1}\left(i\omega\begin{bmatrix}c_3\\ c_4\end{bmatrix}+\begin{bmatrix}k_3\\ k_4\end{bmatrix}\right)^T \tag{67}$$

or, equivalently:

$$\left[\hat{\mathbf{D}}^{CS}(\omega)\right]=\left(i\omega\begin{bmatrix}c_3 & 0\\ 0 & c_4\end{bmatrix}+\begin{bmatrix}k_3 & 0\\ 0 & k_4\end{bmatrix}\right)-\frac{\left(i\omega\begin{bmatrix}c_3\\ c_4\end{bmatrix}+\begin{bmatrix}k_3\\ k_4\end{bmatrix}\right)\left(i\omega\begin{bmatrix}c_3\\ c_4\end{bmatrix}+\begin{bmatrix}k_3\\ k_4\end{bmatrix}\right)^T}{-\omega^2 m_3+i\omega\left(c_3+c_4\right)+\left(k_3+k_4\right)} \tag{68}$$

The nature of the various terms in the condensed formulation (67) can be easily recognized. Moreover, because this example has a single internal variable, it allows for the simple form (68), stressing that the inverted term related to the internal dynamics of the secondary subsystem is invariant, meaning that it will identically affect all the coupling forces. This is quite natural, from a physical point of view, but might be easily overlooked when identifying experimental coupling coefficients affecting complex MDOF structures. Such feature can also provide a check criterion for asserting that all identified coupling forces are physically consistent.

Turning now to the identification problem, we assume that the hidden subsystem to identify has the general structure of equation (43):

$$\left(-\omega^2\begin{bmatrix}\begin{bmatrix}m_1 & 0\\ 0 & m_2\end{bmatrix}+\begin{bmatrix}m_{mm}^{11} & m_{mm}^{12}\\ m_{mm}^{21} & m_{mm}^{22}\end{bmatrix} & \begin{bmatrix}0 & \cdots & 0\\ 0 & \cdots & 0\end{bmatrix}\\ \begin{bmatrix}0 & 0\\ \vdots & \vdots\\ 0 & 0\end{bmatrix} & \begin{bmatrix}1 & \cdots & 0\\ \vdots & \ddots & \vdots\\ 0 & \cdots & 1\end{bmatrix}\end{bmatrix}\right.$$
$$+i\omega\begin{bmatrix}\begin{bmatrix}c_1 & 0\\ 0 & c_2\end{bmatrix}+\begin{bmatrix}c_{mm}^{11} & c_{mm}^{12}\\ c_{mm}^{21} & c_{mm}^{22}\end{bmatrix} & \begin{bmatrix}c_{mh}^{11} & \cdots & c_{mh}^{1H}\\ c_{mh}^{21} & \cdots & c_{mh}^{2H}\end{bmatrix}\\ \begin{bmatrix}c_{mh}^{11} & c_{mh}^{21}\\ \vdots & \vdots\\ c_{mh}^{1H} & c_{mh}^{2H}\end{bmatrix} & \begin{bmatrix}c_{hh}^{1} & \cdots & 0\\ \vdots & \ddots & \vdots\\ 0 & \cdots & c_{hh}^{H}\end{bmatrix}\end{bmatrix}$$
$$\left.+\begin{bmatrix}\begin{bmatrix}k_1 & 0\\ 0 & k_2\end{bmatrix}+\begin{bmatrix}k_{mm}^{11} & k_{mm}^{12}\\ k_{mm}^{21} & k_{mm}^{22}\end{bmatrix} & \begin{bmatrix}k_{mh}^{11} & \cdots & k_{mh}^{1H}\\ k_{mh}^{21} & \cdots & k_{mh}^{2H}\end{bmatrix}\\ \begin{bmatrix}k_{mh}^{11} & k_{mh}^{21}\\ \vdots & \vdots\\ k_{mh}^{1H} & k_{mh}^{2H}\end{bmatrix} & \begin{bmatrix}k_{hh}^{1} & \cdots & 0\\ \vdots & \ddots & \vdots\\ 0 & \cdots & k_{hh}^{H}\end{bmatrix}\end{bmatrix}\right)\begin{Bmatrix}\begin{Bmatrix}X_1(\omega)\\ X_2(\omega)\end{Bmatrix}\\ \begin{Bmatrix}Q_h^1(\omega)\\ \vdots\\ Q_h^H(\omega)\end{Bmatrix}\end{Bmatrix}=\begin{Bmatrix}\begin{Bmatrix}F_{ext}^1(\omega)\\ F_{ext}^2(\omega)\end{Bmatrix}\\ \begin{Bmatrix}0\\ \vdots\\ 0\end{Bmatrix}\end{Bmatrix} \tag{69}$$

and of equation (44):

$$\left[\mathbf{D}_{mm}^{CS}(\omega)\right]=\left(-\omega^2\begin{bmatrix}m_{mm}^{11} & m_{mm}^{12}\\ m_{mm}^{21} & m_{mm}^{22}\end{bmatrix}+i\omega\begin{bmatrix}c_{mm}^{11} & c_{mm}^{12}\\ c_{mm}^{21} & c_{mm}^{22}\end{bmatrix}+\begin{bmatrix}k_{mm}^{11} & k_{mm}^{12}\\ k_{mm}^{21} & k_{mm}^{22}\end{bmatrix}\right)$$
$$-\left(i\omega\begin{bmatrix}c_{mh}^{11} & c_{mh}^{21}\\ \vdots & \vdots\\ c_{mh}^{1H} & c_{mh}^{2H}\end{bmatrix}+\begin{bmatrix}k_{mh}^{11} & k_{mh}^{21}\\ \vdots & \vdots\\ k_{mh}^{1H} & k_{mh}^{2H}\end{bmatrix}\right)^T\left(-\omega^2\begin{bmatrix}1 & \cdots & 0\\ \vdots & \ddots & \vdots\\ 0 & \cdots & 1\end{bmatrix}+i\omega\begin{bmatrix}c_{hh}^{1} & \cdots & 0\\ \vdots & \ddots & \vdots\\ 0 & \cdots & c_{hh}^{H}\end{bmatrix}+\begin{bmatrix}k_{hh}^{1} & \cdots & 0\\ \vdots & \ddots & \vdots\\ 0 & \cdots & k_{hh}^{H}\end{bmatrix}\right)^{-1}\times \quad (70)$$
$$\times\left(i\omega\begin{bmatrix}c_{mh}^{11} & c_{mh}^{21}\\ \vdots & \vdots\\ c_{mh}^{1H} & c_{mh}^{2H}\end{bmatrix}+\begin{bmatrix}k_{mh}^{11} & k_{mh}^{21}\\ \vdots & \vdots\\ k_{mh}^{1H} & k_{mh}^{2H}\end{bmatrix}\right)$$

which, following (47), is equivalent to:

$$\left[\mathbf{D}_{mm}^{CS}(\omega)\right]=\left(-\omega^2\begin{bmatrix}m_{mm}^{11} & m_{mm}^{12}\\ m_{mm}^{21} & m_{mm}^{22}\end{bmatrix}+i\omega\begin{bmatrix}c_{mm}^{11} & c_{mm}^{12}\\ c_{mm}^{21} & c_{mm}^{22}\end{bmatrix}+\left(\begin{bmatrix}k_{mm}^{11} & k_{mm}^{12}\\ k_{mm}^{21} & k_{mm}^{22}\end{bmatrix}-\sum_{n=1}^{H}\mathbf{c}_{mh}^{n}\mathbf{c}_{mh}^{nT}\right)\right)$$
$$-\sum_{n=1}^{H}\frac{\left(\mathbf{k}_{mh}^{n}\mathbf{k}_{mh}^{nT}-k_{hh}^{n}\mathbf{c}_{mh}^{n}\mathbf{c}_{mh}^{nT}\right)+i\omega\left(\mathbf{c}_{mh}^{n}\mathbf{k}_{mh}^{nT}+\mathbf{k}_{mh}^{n}\mathbf{c}_{mh}^{nT}-c_{hh}^{n}\mathbf{c}_{mh}^{n}\mathbf{c}_{mh}^{nT}\right)}{-\omega^2+i\omega c_{hh}^{n}+k_{hh}^{n}} \quad (71)$$

We will assume the following numerical parameters of the reference coupled subsystem:

$$\begin{cases} m_3=2\ \text{kg}\\ c_3=100\ \text{Ns/m},\ c_4=50\ \text{Ns/m}\\ k_3=10^6\ \text{N/m},\ k_4=5\times10^6\ \text{N/m}\end{cases}$$

which are replaced into the reference equation (67), with the same frequency range and sampling of the preceding example, leading to the four "measured" response functions of the coupling matrix $\hat{\mathbf{D}}_{mm}^{CS}(\omega)$. Noisy "measurements" were simulated also for this example, with 10% noise amplitude.

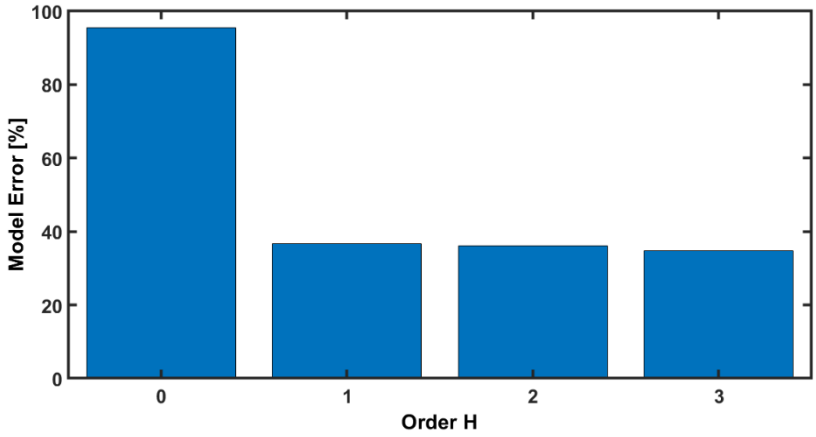

Fig. 12. MDOF structure coupled to SDOF hidden dynamics: Identification error with respect to the noisy "measured" values of the matrix $\hat{\mathbf{D}}_{mm}^{CS}(\omega)$ with 10% noise, as a function of the model order H.

Then, the rational polynomial expansion (26) is fitted to the reference experimental functions $\hat{\mathbf{D}}_{mm}^{CS}(\omega)$, for increasing orders H. In spite of the noisy data, the results shown in Fig. 12 point to the optimal value $H=1$, the chart stabilization value, in agreement with the actual order of the "hidden" coupled subsystem of Fig. 5 (b). Accounting for the significant data noise level, the coupling functions presented in Figs. 13 to 15, obtained from the identified submatrices of (69)-(70), are in reasonable agreement with the reference results.

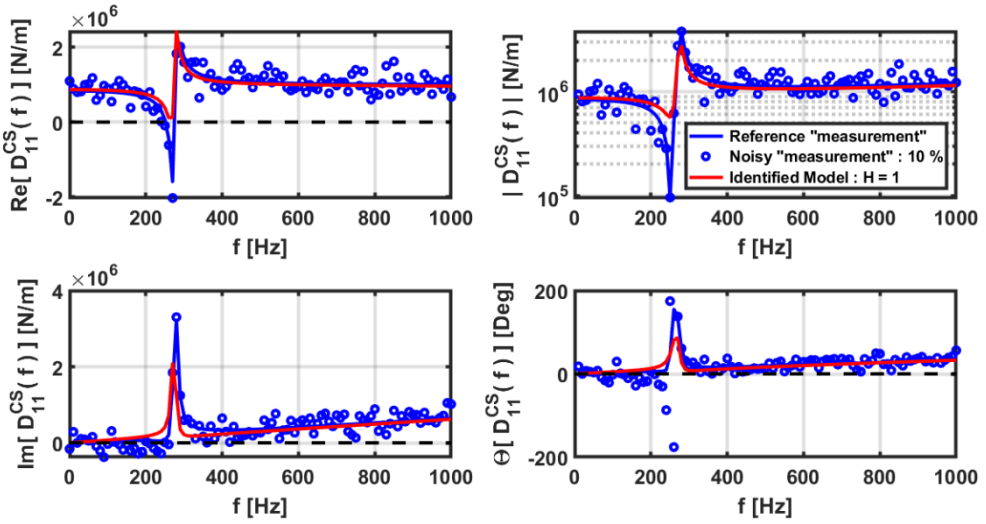

Fig. 13. MDOF structure coupled to SDOF hidden dynamics: Reference noisy "measurement" $\hat{D}_{11}^{CS}(\omega)$ with 10% noise and reconstructed $D_{11}^{CS}(\omega)$ of matrix $\mathbf{D}_{mm}^{CS}(\omega)$ using (70), from the identified model with optimal order $H=1$.

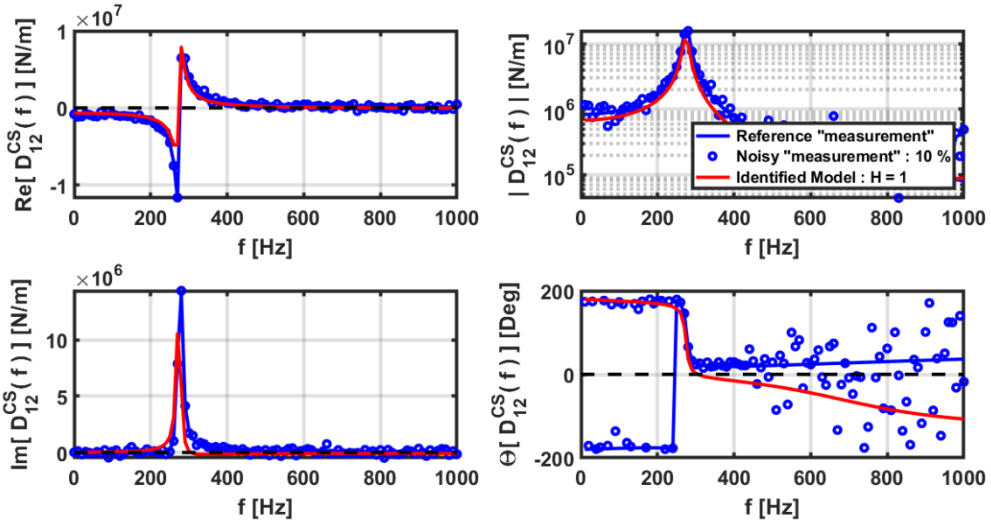

Fig. 14. MDOF structure coupled to SDOF hidden dynamics: Reference noisy "measurement" $\hat{D}_{12}^{CS}(\omega)=\hat{D}_{21}^{CS}(\omega)$ with 10% noise and reconstructed $D_{12}^{CS}(\omega)$ of matrix $\mathbf{D}_{mm}^{CS}(\omega)$ using (70), from the identified model with optimal order $H=1$.

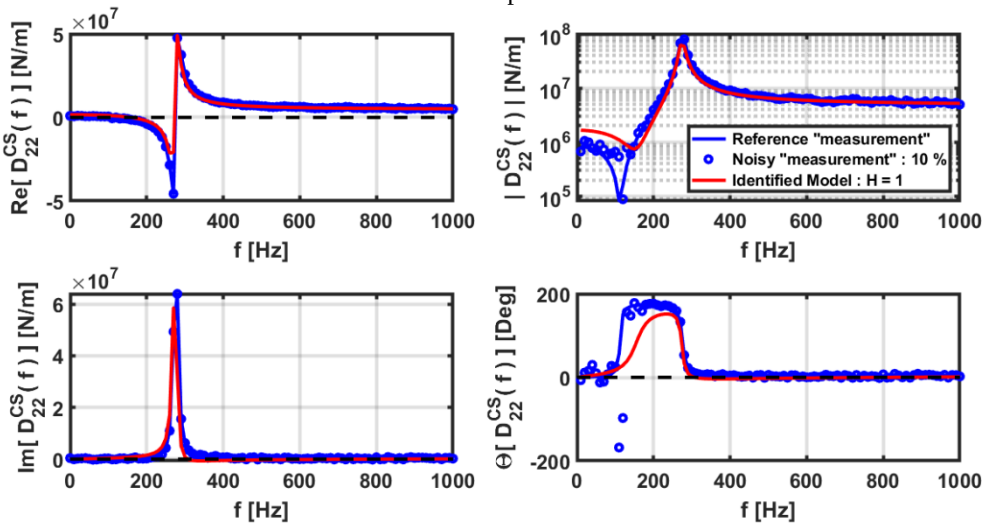

Fig. 15. MDOF structure coupled to SDOF hidden dynamics: Reference noisy "measurement" $\hat{D}_{22}^{CS}(\omega)$ with 10% noise and reconstructed $D_{22}^{CS}(\omega)$ of matrix $\mathbf{D}_{mm}^{CS}(\omega)$ using (70), from the identified model with optimal order $H=1$.

The identified results show that the identification method displays a reasonably satisfactory performance, for two quite different and complementary examples, both sharing some features with flow-structure interaction problems. The identification approach appears to be reasonably robust to noise effects, suggesting that it can be applied to actual experimental data.

6. Fluidelastic coupling in tube bundles

6.1 Relations between physical and dimensionless quantities

The general formulation (43)-(44) applies to a fluidelastically coupled tube bundle with multiple flexible tubes. For the sake of simplicity we will tacitly assume here that the fluidelastic forces solely depend on the reduced frequency, although such assumption is not strictly true, see Piteau et al. (2019) and Lagrange et al. (2019). As discussed earlier, the fluidelastic forces are commonly expressed in terms of dimensionless fluidelastic coefficients per unit length of the structure, $\mathbf{C}_m(\bar{\omega})$, $\mathbf{C}_d(\bar{\omega})$ and $\mathbf{C}_k(\bar{\omega})$, such that:

$$\frac{\hat{\mathbf{D}}_{mm}^{FS}(\omega)}{\frac{1}{2}\rho_f V_p^2 L} = \hat{\bar{\mathbf{D}}}_{mm}^{FS}(\bar{\omega}) = -\bar{\omega}^2\mathbf{C}_m(\bar{\omega}) + i\bar{\omega}\mathbf{C}_d(\bar{\omega}) + \mathbf{C}_k(\bar{\omega}) \quad ; \quad \bar{\omega} = \frac{\omega D}{V_p} \tag{72}$$

with the flow pitch velocity V_p and density ρ_f, and the tubes diameter D and wet length L. The dimensionless fluidelastic coefficients in (72) are related to the physical coefficients of expression (3) through:

$$\mathbf{C}_m = \frac{\mathbf{M}_{mm}^{FS}}{\frac{1}{2}\rho_f D^2 L} \quad ; \quad \mathbf{C}_d(\bar{\omega}) = \frac{\mathbf{C}_{mm}^{FS}(\omega)}{\frac{1}{2}\rho_f V_p D L} \quad ; \quad \mathbf{C}_k(\bar{\omega}) = \frac{\mathbf{K}_{mm}^{FS}(\omega)}{\frac{1}{2}\rho_f V_p^2 L} \tag{73}$$

The added mass coefficient is typically taken under stagnant conditions. From (72), the expression for building the physical function $\hat{\mathbf{D}}_{mm}^{FS}(\omega)$ from the dimensionless fluidelastic coefficients is:

$$\hat{\mathbf{D}}_{mm}^{FS}(\omega) = \frac{1}{2}\rho_f V_p^2 L\left(-\omega^2\left(\frac{D}{V_p}\right)^2\mathbf{C}_m(\bar{\omega}) + i\omega\frac{D}{V_p}\mathbf{C}_d(\bar{\omega}) + \mathbf{C}_k(\bar{\omega})\right) \quad ; \quad \bar{\omega} = \frac{\omega D}{V_p} \tag{74}$$

and notice that, replacing (73) into (74), the resulting expression simplifies to (3):

$$\hat{\mathbf{D}}_{mm}^{FS}(\omega) = -\omega^2\mathbf{M}_{mm}^{FS} + i\omega\mathbf{C}_{mm}^{FS}(\omega) + \mathbf{K}_{mm}^{FS}(\omega) \tag{75}$$

as it should, for consistent scaling factors.

We now express formulation (43) in terms of the tubes uncoupled modes $\boldsymbol{\psi}_r$ (those of the individual tubes), with $r = 1, 2, \cdots, R$, such that $\mathbf{x}_m(\omega) = \left[\boldsymbol{\psi}_1\boldsymbol{\psi}_2\cdots\boldsymbol{\psi}_R\right]\mathbf{q}_r(\omega) \equiv \boldsymbol{\Psi}\mathbf{q}_r(\omega)$. Replacing the modal expansion into (43) and then pre-multiplying the first equation by $\boldsymbol{\Psi}^T$ one obtains:

$$\left(-\omega^2\begin{bmatrix}\boldsymbol{\Psi}^T\mathbf{M}_{mm}^S\boldsymbol{\Psi} + \boldsymbol{\Psi}^T\mathbf{M}_{mm}^F\boldsymbol{\Psi} & \mathbf{0}_{mh}\\ \left(\mathbf{0}_{mh}\right)^T & \boldsymbol{I}_{hh}\end{bmatrix} + i\omega\begin{bmatrix}\boldsymbol{\Psi}^T\mathbf{C}_{mm}^S\boldsymbol{\Psi} + \boldsymbol{\Psi}^T\mathbf{C}_{mm}^F\boldsymbol{\Psi} & \boldsymbol{\Psi}^T\mathbf{C}_{mh}^F\\ \left(\boldsymbol{\Psi}^T\mathbf{C}_{mh}^F\right)^T & \boldsymbol{C}_{hh}^F\end{bmatrix} + \begin{bmatrix}\boldsymbol{\Psi}^T\mathbf{K}_{mm}^S\boldsymbol{\Psi} + \boldsymbol{\Psi}^T\mathbf{K}_{mm}^F\boldsymbol{\Psi} & \boldsymbol{\Psi}^T\mathbf{K}_{mh}^F\\ \left(\boldsymbol{\Psi}^T\mathbf{K}_{mh}^F\right)^T & \boldsymbol{K}_{hh}^F\end{bmatrix}\right)\begin{Bmatrix}\mathbf{q}_r(\omega)\\ \mathbf{q}_h(\omega)\end{Bmatrix} = \begin{Bmatrix}\boldsymbol{\Psi}^T\mathbf{f}_m^{Ext}(\omega)\\ \mathbf{0}_h\end{Bmatrix} \tag{76}$$

where we define the structural modal parameters through the diagonal matrices $\boldsymbol{M}_{rr}^{S} = \boldsymbol{\Psi}^T \mathbf{M}_{mm}^{S} \boldsymbol{\Psi}$, $\boldsymbol{C}_{rr}^{S} = \boldsymbol{\Psi}^T \mathbf{C}_{mm}^{S} \boldsymbol{\Psi}$ and $\boldsymbol{K}_{rr}^{S} = \boldsymbol{\Psi}^T \mathbf{K}_{mm}^{S} \boldsymbol{\Psi}$, as well as the modal excitations $\boldsymbol{f}_r^{Ext}(\omega) = \boldsymbol{\Psi}^T \mathbf{f}_m^{Ext}(\omega)$.

Now, let us assume that the fluidelastic coupling matrices in formulation (76) were identified from the dimensionless experimental functions $\hat{\bar{\mathbf{D}}}_{mm}^{FS}(\bar{\omega})$ per unit length of the tubes. We denote such matrices as $\bar{\mathbf{M}}_{mm}^{F}$, $\bar{\mathbf{C}}_{mm}^{F}$, $\bar{\mathbf{K}}_{mm}^{F}$, $\bar{\mathbf{M}}_{hh}^{F}$, $\bar{\mathbf{C}}_{hh}^{F}$, $\bar{\mathbf{K}}_{hh}^{F}$, $\bar{\mathbf{M}}_{mh}^{F}$, $\bar{\mathbf{C}}_{mh}^{F}$ and $\bar{\mathbf{K}}_{mh}^{F}$, which are all scaled by the factor $(1/2)\rho_f V_p^2 L$ (where L is the length of the tubes of interest in the predictive analysis) and referred to the dimensionless circular frequency $\bar{\omega} = \omega D / V_p$. Then, proceeding as before for converting from dimensionless to physical quantities, the coupled modal formulation (76) becomes:

$$\left(-\omega^2 \begin{bmatrix} \boldsymbol{M}_{rr}^{S} + a\boldsymbol{\Psi}^T \bar{\mathbf{M}}_{mm}^{F} \boldsymbol{\Psi} & \mathbf{0}_{mh} \\ \left(\mathbf{0}_{mh}\right)^T & a\boldsymbol{I}_{hh} \end{bmatrix} + i\omega \begin{bmatrix} \boldsymbol{C}_{rr}^{S} + b\boldsymbol{\Psi}^T \bar{\mathbf{C}}_{mm}^{F} \boldsymbol{\Psi} & b\boldsymbol{\Psi}^T \bar{\mathbf{C}}_{mh}^{F} \\ b\left(\boldsymbol{\Psi}^T \bar{\mathbf{C}}_{mh}^{F}\right)^T & b\bar{\boldsymbol{C}}_{hh}^{F} \end{bmatrix} + \begin{bmatrix} \boldsymbol{K}_{rr}^{S} + c\boldsymbol{\Psi}^T \bar{\mathbf{K}}_{mm}^{F} \boldsymbol{\Psi} & c\boldsymbol{\Psi}^T \bar{\mathbf{K}}_{mh}^{F} \\ c\left(\boldsymbol{\Psi}^T \bar{\mathbf{K}}_{mh}^{F}\right)^T & c\bar{\boldsymbol{K}}_{hh}^{F} \end{bmatrix} \right) \begin{Bmatrix} \mathbf{q}_r(\omega) \\ \mathbf{q}_h(\omega) \end{Bmatrix} = \begin{Bmatrix} \boldsymbol{f}_r^{Ext}(\omega) \\ \mathbf{0}_h \end{Bmatrix} \tag{77}$$

or, in the time-domain:

$$\begin{bmatrix} \boldsymbol{M}_{rr}^{S} + a\boldsymbol{\Psi}^T \bar{\mathbf{M}}_{mm}^{F} \boldsymbol{\Psi} & \mathbf{0}_{mh} \\ \left(\mathbf{0}_{mh}\right)^T & a\boldsymbol{I}_{hh} \end{bmatrix} \begin{Bmatrix} \ddot{\mathbf{q}}_r(t) \\ \ddot{\mathbf{q}}_h(t) \end{Bmatrix} + \begin{bmatrix} \boldsymbol{C}_{rr}^{S} + b\boldsymbol{\Psi}^T \bar{\mathbf{C}}_{mm}^{F} \boldsymbol{\Psi} & b\boldsymbol{\Psi}^T \bar{\mathbf{C}}_{mh}^{F} \\ b\left(\boldsymbol{\Psi}^T \bar{\mathbf{C}}_{mh}^{F}\right)^T & b\bar{\boldsymbol{C}}_{hh}^{F} \end{bmatrix} \begin{Bmatrix} \dot{\mathbf{q}}_r(t) \\ \dot{\mathbf{q}}_h(t) \end{Bmatrix} + \begin{bmatrix} \boldsymbol{K}_{rr}^{S} + c\boldsymbol{\Psi}^T \bar{\mathbf{K}}_{mm}^{F} \boldsymbol{\Psi} & c\boldsymbol{\Psi}^T \bar{\mathbf{K}}_{mh}^{F} \\ c\left(\boldsymbol{\Psi}^T \bar{\mathbf{K}}_{mh}^{F}\right)^T & c\bar{\boldsymbol{K}}_{hh}^{F} \end{bmatrix} \begin{Bmatrix} \mathbf{q}_r(t) \\ \mathbf{q}_h(t) \end{Bmatrix} = \begin{Bmatrix} \boldsymbol{f}_r^{Ext}(t) \\ \mathbf{0}_h \end{Bmatrix} \tag{78}$$

with the conversion coefficients:

$$a = \frac{1}{2}\rho_f V_p^2 L \left(\frac{D}{V_p}\right)^2 = \frac{1}{2}\rho_f D^2 L \quad ; \quad b = \frac{1}{2}\rho_f V_p^2 L \frac{D}{V_p} = \frac{1}{2}\rho_f V_p D L \quad ; \quad c = \frac{1}{2}\rho_f V_p^2 L \tag{79}$$

Therefore, a single identification of the fluidelastic coupling matrices, from the dimensionless experimental data $\hat{\bar{\mathbf{D}}}_{mm}^{FS}(\bar{\omega})$, is needed for all specific cases. Indeed, whatever the actual values of the flow velocity V_p and density ρ_f, and of the structural parameters D and L, the scaling coefficients a, b and c will readily adapt equations (77) and (78) for any actual application.

In its essence, nothing prevents this approach to be applicable to two-phase flows. However, when dealing with the actual fluidelastic reduced data, conversion from dimensionless to dimensional fluidelastic forces must account for the specificities of the reduced data. In cases when collapsing the experimental data (single-phase or two-phase) implies the use of more complex and/or multiple reducing parameters - see papers by Lagrange et al. (2019, 2023) - the formulations for converting the identified reduced fluidelastic function(s) to the corresponding dimensional forces should be adapted accordingly.

6.2 Relation of the present formulation with results in unsteady aeroelasticity

One will notice that models for unsteady aerodynamics, widely used for predicting the stability of airplane wings and bridge decks, are quite close the formulation for fluidelastic forces developed here. Actually, following the seminal work of Wagner (1925) and Theodorsen

(1935) in unsteady aerofoil theory, see Fung (1969) or Dowell (2022), many researchers developed related formulations for generalized aeroelastic systems, see Eversman and Tewari (1991) and Tewari (2015). In particular, Sevart (1975), Roger (1977) and Abel (1979) proposed the following dimensionless expression to model the unsteady aeroelastic forces $\hat{\bar{\mathbf{D}}}_{mm}^{AE}(\bar{s})$, the so-called "Aerodynamic influence coefficient matrix":

$$\hat{\bar{\mathbf{D}}}_{mm}^{AE}(\bar{s}) = \bar{s}^2\mathbf{A}_2 + \bar{s}\,\mathbf{A}_1 + \mathbf{A}_0 + \sum_{n=1}^{N}\frac{\bar{s}\,\mathbf{A}_{n+2}}{\bar{s}+\gamma_n} \quad ; \quad \bar{s} = \frac{sB}{V_f} \tag{80}$$

where B is a reference length (typically the wing semi-chord length) and V_f the flow velocity, while the γ_n enter the formulation as real positive "lag parameters". In terms of the dimensionless circular frequency, (80) reads:

$$\hat{\bar{\mathbf{D}}}_{mm}^{AE}(\bar{\omega}) = -\bar{\omega}^2\mathbf{A}_2 + i\bar{\omega}\mathbf{A}_1 + \mathbf{A}_0 + \sum_{n=1}^{N}\frac{i\bar{\omega}}{i\bar{\omega}+\gamma_n}\mathbf{A}_{n+2} \quad ; \quad \bar{\omega} = \frac{\omega B}{V_f} \tag{81}$$

and the model identification is through parameters γ_n and matrices $\mathbf{A}_0 \sim \mathbf{A}_{N+2}$. In this context, Tiffany and Adams (1987) and Eversman and Tewari (1991) refined the identification of the lag parameters, whereas the Minimum State Method proposed by Karpel (1982) is the following richer variant of (80), which enables more compact approximations:

$$\hat{\bar{\mathbf{D}}}_{mm}^{AE}(\bar{\omega}) = -\bar{\omega}^2\mathbf{A}_2 + i\bar{\omega}\,\mathbf{A}_1 + \mathbf{A}_0 + i\bar{\omega}\,\mathbf{D}\left(i\bar{\omega}\boldsymbol{I} - \boldsymbol{R}\right)^{-1}\mathbf{E} \quad ; \quad \bar{\omega} = \frac{\omega B}{V_f} \tag{82}$$

where the lag parameters are embedded in the diagonal matrix $\boldsymbol{R}$, which must be identified with matrices $\mathbf{A}_0 \sim \mathbf{A}_2$, $\mathbf{D}$ and $\mathbf{E}$. Notice that (81) can be cast in the form (82) by writing:

$$\mathbf{D} = \begin{bmatrix}\boldsymbol{I}_1 & \boldsymbol{I}_2 & \cdots & \boldsymbol{I}_N\end{bmatrix} \quad ; \quad \boldsymbol{R} = -\begin{bmatrix}\gamma_1\boldsymbol{I}_1 & \mathbf{0} & \cdots & \mathbf{0}\\ \mathbf{0} & \gamma_2\boldsymbol{I}_2 & \cdots & \mathbf{0}\\ \vdots & \vdots & \ddots & \vdots\\ \mathbf{0} & \mathbf{0} & \cdots & \gamma_N\boldsymbol{I}_N\end{bmatrix} \quad ; \quad \mathbf{E} = \begin{bmatrix}\mathbf{A}_3\\ \mathbf{A}_4\\ \vdots\\ \mathbf{A}_{N+2}\end{bmatrix} \tag{83}$$

where the identity matrices $\boldsymbol{I}_1 \sim \boldsymbol{I}_N$ are the same size of the square matrices $\mathbf{A}_n$.

The proximity of (81) with (31), which is directly related with the modelling framework (43), is unmistakable. This is even more so, as some authors prefer a modified form of (80) without $\bar{s}$ multiplying the numerators of the expansion, because - as stated by Eversman and Tewari (1991) - "The present study has determined that there is no need to include the Laplace variable in the numerator of the lag terms". Hence the ensuing alternative to model (81):

$$\hat{\bar{\mathbf{D}}}_{mm}^{AE}(\bar{\omega}) = -\bar{\omega}^2\mathbf{A}_2 + i\bar{\omega}\mathbf{A}_1 + \mathbf{A}_0 + \sum_{n=1}^{N}\frac{\mathbf{A}_{n+2}}{i\bar{\omega}+\gamma_n} \quad ; \quad \bar{\omega} = \frac{\omega B}{V_f} \tag{84}$$

which is similar to (31), although the poles λ_n in (31) may be real or complex, whereas the poles γ_n only take real values. Obviously, analogue to the present work, these are augmented aeroelastic models, with internal flow variables. However, opposite to the proposed framework, they are mostly of empirical nature, certainly resulting from ample insight, but lacking a formal justification for their successful structure, which is mathematically demonstrated here as a direct consequence of formulation (43). On the other hand, in the field of aeroelasticity frequency-domain models are typically converted to the time-domain using first-order state-space formulations, suitable for control purposes, whereas in the present work second-order formulations are preferred for their insight potential.

7. Application to experimental data obtained at "CEA-Saclay"

7.1 Tested system and fluidelastic measurements

Experiments are often performed using a rigid bundle subjected to cross-flow, with a single flexible tube vibrating along the lift direction. Such was the case of the system tested at CEA-Saclay, which is shown in Fig. 16, from which fluidelastic forces were identified by Piteau et al. (2012, 2018) for water cross-flow. The bundle consists of 15 tubes (3×5) with $D=30$ mm and $P/D=1.5$. A control system enabled to identify the fluidelastic coefficients in the range $V_p=0.7\sim2.5$ m/s, well beyond the fluidelastic instability boundary, corresponding to a reduced velocity of $V_R=V_p/(f_V D)=1.3\sim5.3$, with $f_V\equiv f_1(V_p)$, and to the Reynolds number range $\mathrm{Re}=21000\sim87000$. The tube is clamped through a flat bar, in order to constrain the vibrations to be planar, leading to a first modal frequency f_1 along the lift direction of 29 Hz in air and 18 Hz in stagnant water.

The control system used for the estimation of fluidelastic forces is shown in Figs. 16(a,b). This control system was used essentially to enable their estimation at higher flow velocities, well within the fluidelastic instability region of the test rig. Concerning the flow forces, they were not directly measured, neither was the tube motion directly imposed, in this experimental set-up. Actually, the fluidelastic forces were indirectly inferred from the changes in the modal frequency and modal damping of the vibrating tube, under natural excitation by the flow turbulence. All the experimental details and procedures used in the experiments are thoroughly described by Caillaud et al. (2003).

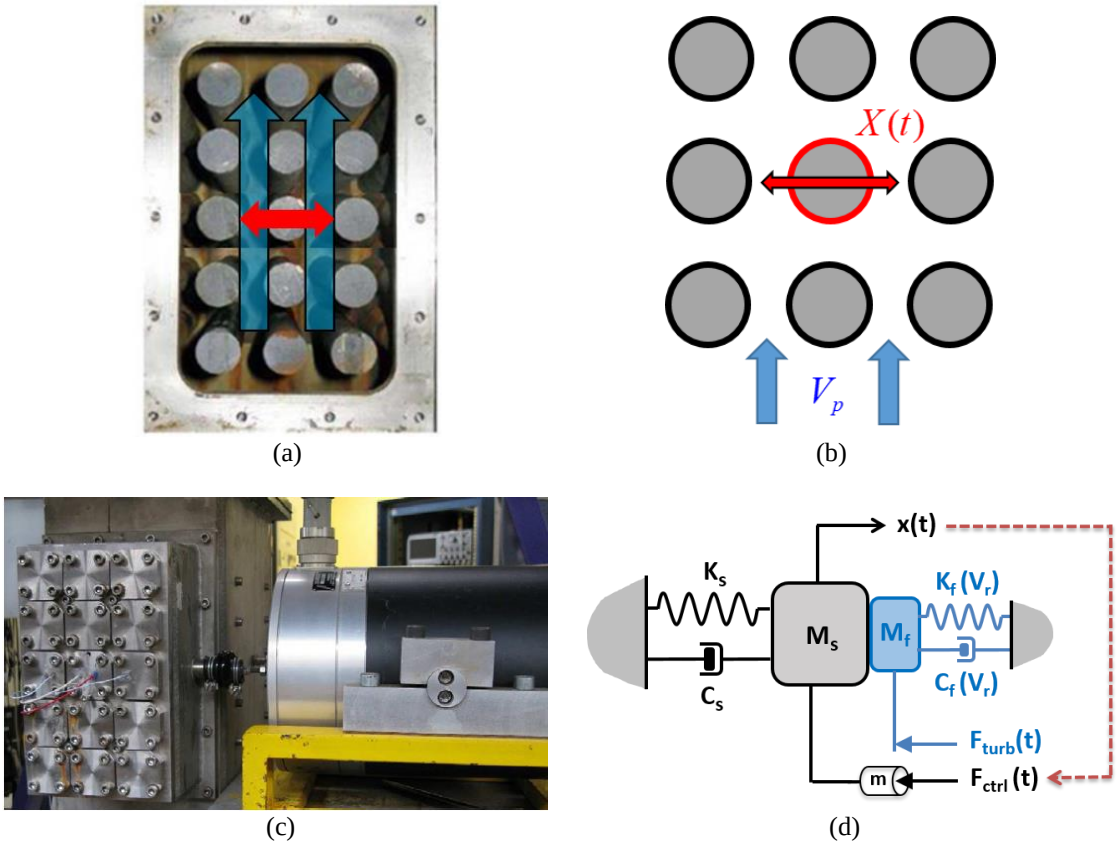

(a) (b)

(c) (d)

Fig. 16. Experiments performed at CEA-Saclay by Piteau et al. (2012): (a,b) Flexible tube in a rigid square bundle, subjected to cross-flow and vibrating along the lift direction; (c) Electromagnetic shaker for stabilization of the tube through feedback control (Caillaud et al., 2003); (d) Scheme of the control loop (Piteau et al., 2019).

From these experiments were obtained the dimensionless fluidelastic coefficients $C_k(V_R)$ and $C_d(V_R)$ shown in Fig. 2, while a constant value of the dimensionless added-mass per unit length was assumed, estimated at $C_m = 2.01$ in stagnant water. Notice that, in accordance with the sign convention for the dimensionless fluidelastic coefficients per unit length adopted here, the plots in Fig. 2 are such that positive values of $C_d(V_R)$ are stabilizing, while positive values of $C_k(V_R)$ increase the modal frequency of the flow-structure coupled system. As a general trend, $C_d(V_R)$ decreases as V_R increases, becoming negative and leading to fluidelastic instability beyond about $V_R > 3.8$. The sudden decrease of $C_d(V_R)$ near $V_R \approx 2.2$ was tentatively attributed to vortex shedding phenomena. For the full range of flow velocity explored in the tests, except a couple of measurements, $C_k(V_R)$ decreases as V_R increases.

From the coupling coefficients, the dimensionless fluidelastic function $\hat{\bar{D}}_{mm}^{FS}(\bar{\omega})$ was obtained from expression (72). The real and imaginary parts of $\hat{\bar{D}}_{mm}^{FS}(\bar{\omega})$ are shown in Fig. 17 as a function of the reduced frequency f_R and of the reduced velocity V_R, as well as the corresponding Argand plot.

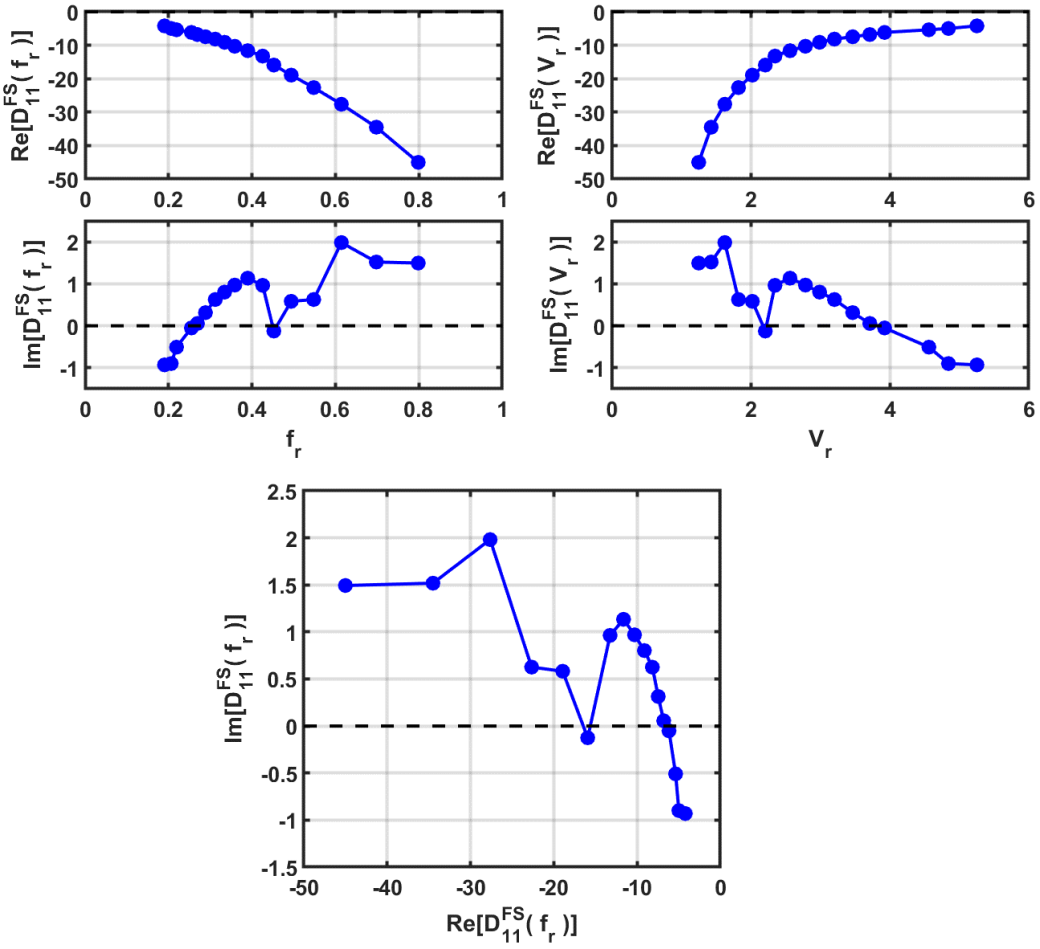

Fig. 17. Experiments performed at CEA-Saclay by Piteau et al. (2018): Dimensionless fluidelastic function $\hat{\bar{D}}_{mm}^{FS}(\bar{\omega})$ obtained from the experimental dimensionless coefficients. Real part, imaginary part and Argand plot.

7.2 Fluidelastic coupling in a square bundle with a single lift-vibrating tube

For the measurements performed with the tested bundle, the dimensionless flow-structure coupled equation becomes:

$$\left(-\bar{\omega}^2 \begin{bmatrix} \bar{m}_{mm}^S + \bar{m}_{mm}^F & \begin{bmatrix} 0 & \cdots & 0 \end{bmatrix} \\ \begin{bmatrix} 0 \\ \vdots \\ 0 \end{bmatrix} & \begin{bmatrix} 1 & \cdots & 0 \\ \vdots & \ddots & \vdots \\ 0 & \cdots & 1 \end{bmatrix} \end{bmatrix} + i\bar{\omega} \begin{bmatrix} \bar{c}_{mm}^S + \bar{c}_{mm}^F & \begin{bmatrix} \bar{c}_{mh}^1 & \cdots & \bar{c}_{mh}^H \end{bmatrix} \\ \begin{bmatrix} \bar{c}_{mh}^1 \\ \vdots \\ \bar{c}_{mh}^H \end{bmatrix} & \begin{bmatrix} \bar{c}_{hh}^1 & \cdots & 0 \\ \vdots & \ddots & \vdots \\ 0 & \cdots & \bar{c}_{hh}^H \end{bmatrix} \end{bmatrix} + \begin{bmatrix} \bar{k}_{mm}^S + \bar{k}_{mm}^F & \begin{bmatrix} \bar{k}_{mh}^1 & \cdots & \bar{k}_{mh}^H \end{bmatrix} \\ \begin{bmatrix} \bar{k}_{mh}^1 \\ \vdots \\ \bar{k}_{mh}^H \end{bmatrix} & \begin{bmatrix} \bar{k}_{hh}^1 & \cdots & 0 \\ \vdots & \ddots & \vdots \\ 0 & \cdots & \bar{k}_{hh}^H \end{bmatrix} \end{bmatrix} \right) \begin{Bmatrix} \bar{X}_m(\bar{\omega}) \\ \begin{Bmatrix} \bar{Q}_h^1(\bar{\omega}) \\ \vdots \\ \bar{Q}_h^H(\bar{\omega}) \end{Bmatrix} \end{Bmatrix} = \begin{Bmatrix} \bar{F}_{ext}(\bar{\omega}) \\ \begin{Bmatrix} 0 \\ \vdots \\ 0 \end{Bmatrix} \end{Bmatrix} \quad (85)$$

with the hidden variables given, as a function of the measured variable, by:

$$\begin{Bmatrix} \bar{Q}_h^1(\bar{\omega}) \\ \vdots \\ \bar{Q}_h^H(\bar{\omega}) \end{Bmatrix} = -\left(-\bar{\omega}^2 \begin{bmatrix} 1 & \cdots & 0 \\ \vdots & \ddots & \vdots \\ 0 & \cdots & 1 \end{bmatrix} + i\bar{\omega} \begin{bmatrix} \bar{c}_{hh}^1 & \cdots & 0 \\ \vdots & \ddots & \vdots \\ 0 & \cdots & \bar{c}_{hh}^H \end{bmatrix} + \begin{bmatrix} \bar{k}_{hh}^1 & \cdots & 0 \\ \vdots & \ddots & \vdots \\ 0 & \cdots & \bar{k}_{hh}^H \end{bmatrix} \right)^{-1} \left(i\bar{\omega} \begin{Bmatrix} \bar{c}_{mh}^1 \\ \vdots \\ \bar{c}_{mh}^H \end{Bmatrix} + \begin{Bmatrix} \bar{k}_{mh}^1 \\ \vdots \\ \bar{k}_{mh}^H \end{Bmatrix} \right) \bar{X}_m(\bar{\omega}) \quad (86)$$

so that the dimensionless fluidelastic function is written:

$$\bar{D}_{mm}^{FS}(\bar{\omega}) = \left(-\bar{\omega}^2 \bar{m}_{mm}^F + i\bar{\omega}\bar{c}_{mm}^F + \bar{k}_{mm}^F \right)$$

$$- \left(i\bar{\omega} \begin{Bmatrix} \bar{c}_{mh}^1 \\ \vdots \\ \bar{c}_{mh}^H \end{Bmatrix} + \begin{Bmatrix} \bar{k}_{mh}^1 \\ \vdots \\ \bar{k}_{mh}^H \end{Bmatrix} \right)^T \left(-\bar{\omega}^2 \begin{bmatrix} 1 & \cdots & 0 \\ \vdots & \ddots & \vdots \\ 0 & \cdots & 1 \end{bmatrix} + i\bar{\omega} \begin{bmatrix} \bar{c}_{hh}^1 & \cdots & 0 \\ \vdots & \ddots & \vdots \\ 0 & \cdots & \bar{c}_{hh}^H \end{bmatrix} + \begin{bmatrix} \bar{k}_{hh}^1 & \cdots & 0 \\ \vdots & \ddots & \vdots \\ 0 & \cdots & \bar{k}_{hh}^H \end{bmatrix} \right)^{-1} \left(i\bar{\omega} \begin{Bmatrix} \bar{c}_{mh}^1 \\ \vdots \\ \bar{c}_{mh}^H \end{Bmatrix} + \begin{Bmatrix} \bar{k}_{mh}^1 \\ \vdots \\ \bar{k}_{mh}^H \end{Bmatrix} \right) \quad (87)$$

with the optimal order H of the flow hidden degrees of freedom to be established, in order to reproduce the essential features of the measured $\hat{\bar{D}}_{mm}^{FS}(\bar{\omega})$.

7.3 Formulation of the fluidelastic forces using the proposed approach

For the polynomial identification of the fluidelastic data through expression (26), opposite to the simpler identifications performed in section 5, a constraint imposing stable poles (negative real parts) was here activated in the identification algorithm. This is necessary to insure that the flow-coupling forces lag the structure motions, as dictated by the system physics. Satisfactory identifications from the experimental fluidelastic data were achieved, although the procedure proved somewhat delicate. Actually, when stability of the model is imposed, the zeros/poles identified in (26) depend somewhat on the identification method parameters. Here, after many trials, we used the value $\lambda_r = 4\times10^{-5}$ for the algorithm regularization parameter, as it led to consistent data fitting as the model order H was increased. On the other hand, for some values of the poles/residuals, the scalar solutions k_n and c_n computed from (101) are only complex. Therefore, there is room for improvement of the present identification approach.

The decrease of the identification error as H increases is shown in Fig. 18, for order $H = 0 \sim 3$. The results obtained suggest that low model orders are enough to capture the system dynamics embedded in the experimental data, as shown in Figs. 19 to 22, which present the

measured dimensionless data $\hat{\bar{D}}_{mm}^{FS}(\bar{\omega})$ and the corresponding identified models $\bar{D}_{mm}^{FS}(\bar{\omega})$, equation (87), for increasing order $H = 0 \sim 3$. The experimental data and identified curves are shown as a function of the reduced frequency f_R and of the reduced velocity V_R, as well as the corresponding Argand plots.

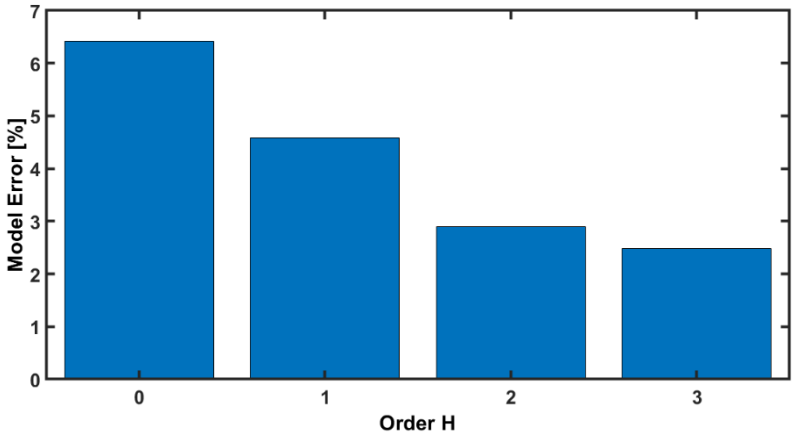

Fig. 18. Experiments performed at CEA-Saclay by Piteau et al. (2018): Identification error with respect to the measured values of $\hat{\bar{D}}_{11}^{FS}(\bar{\omega})$ as a function of the model order H.

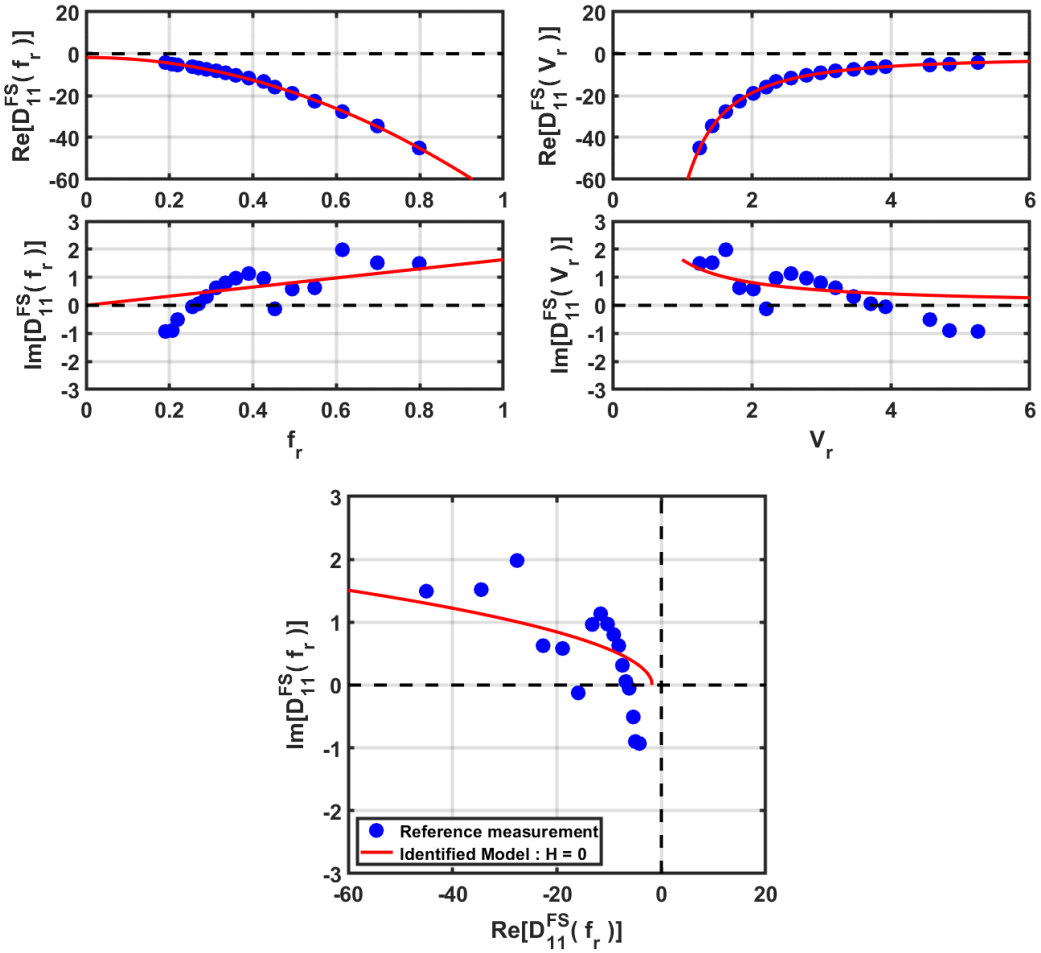

Fig. 19. Experiments performed at CEA-Saclay by Piteau et al. (2018): Reference measurement $\hat{\bar{D}}_{11}^{FS}(\bar{\omega})$ and reconstructed $\bar{D}_{11}^{FS}(\bar{\omega})$ from the identified model with order $H = 0$.

The identified results with $H=0$ of Fig. 19 are obviously reduced to the flow force terms directly applied to the structural measurement DOF, with no hidden flow dynamics. In terms of equation (85), the identified dimensionless flow-structure model is:

$$\left(-\bar{\omega}^2\left(\bar{m}^S_{mm}+\bar{m}^F_{mm}\right)+i\bar{\omega}\left(\bar{c}^S_{mm}+\bar{c}^F_{mm}\right)+\left(\bar{k}^S_{mm}+\bar{k}^F_{mm}\right)\right)\bar{X}_m(\bar{\omega})=\bar{F}_{ext}(\bar{\omega}) \tag{88}$$

with the numerical values:

$$\bar{m}^F_{mm}=1.72 \quad ; \quad \bar{c}^F_{mm}=0.259 \quad ; \quad \bar{k}^F_{mm}=-1.78 \tag{89}$$

and the curves in the first plot of Fig. 19 clearly show the corresponding inertial and damping behavior, as well as the residual negative stiffness at $\bar{\omega}=0$. Notice that the identified dimensionless added mass $\bar{m}^F_{mm}=1.72$ is reasonably close to the measured value under stagnant conditions $C_m=2.01$.

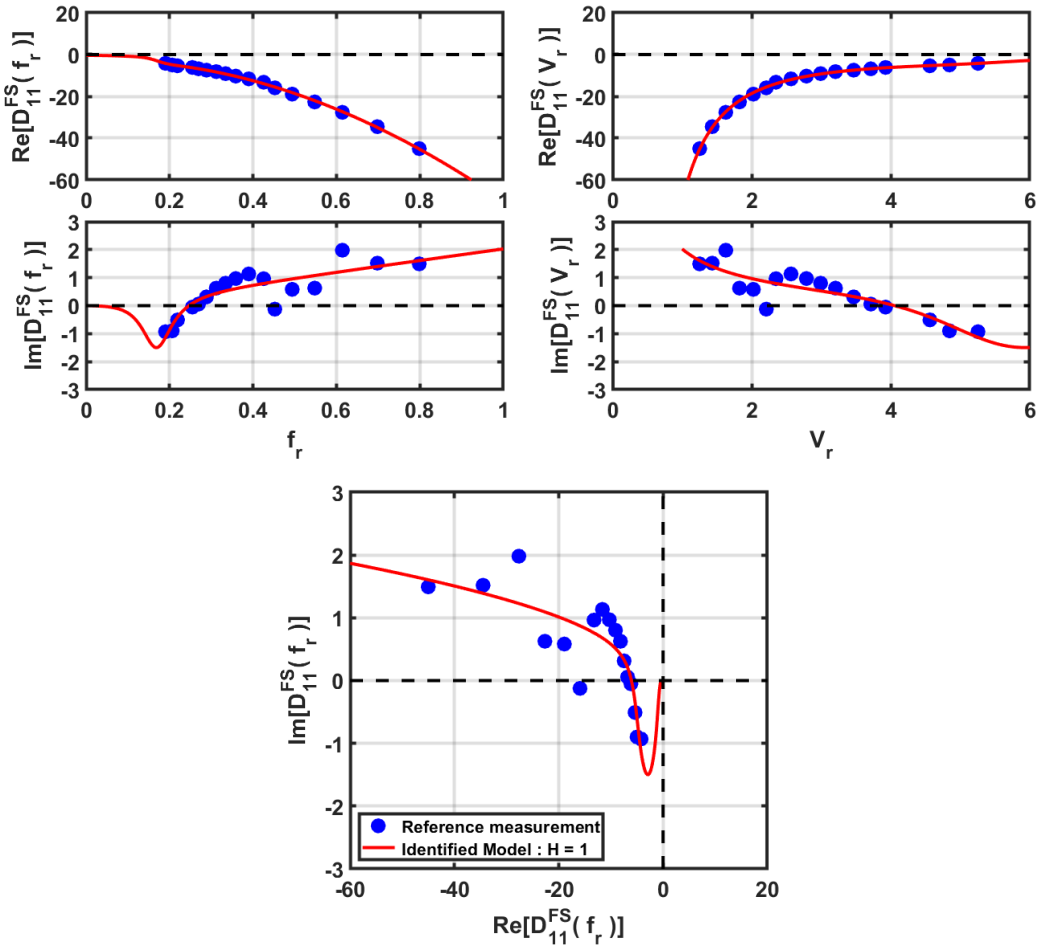

Fig. 20. Experiments performed at CEA-Saclay by Piteau et al. (2018): Reference measurement $\hat{\bar{D}}^{FS}_{11}(\bar{\omega})$ and reconstructed $\bar{D}^{FS}_{11}(\bar{\omega})$ from the identified model with order $H=1$.

For the case $H=1$ presented in Fig. 20, there is a single hidden flow variable, leading to the dimensionless model:

$$\left(-\bar{\omega}^2\begin{bmatrix}\bar{m}^S_{mm}+\bar{m}^F_{mm} & \bar{\mathbf{M}}^F_{mh}\\ \left(\bar{\mathbf{M}}^F_{mh}\right)^T & \bar{\boldsymbol{M}}^F_{hh}\end{bmatrix}+i\bar{\omega}\begin{bmatrix}\bar{c}^S_{mm}+\bar{c}^F_{mm} & \bar{\mathbf{C}}^F_{mh}\\ \left(\bar{\mathbf{C}}^F_{mh}\right)^T & \bar{\boldsymbol{C}}^F_{hh}\end{bmatrix}+\begin{bmatrix}\bar{k}^S_{mm}+\bar{k}^F_{mm} & \bar{\mathbf{K}}^F_{mh}\\ \left(\bar{\mathbf{K}}^F_{mh}\right)^T & \bar{\boldsymbol{K}}^F_{hh}\end{bmatrix}\right)\begin{Bmatrix}\bar{X}_1(\bar{\omega})\\ \bar{\mathbf{q}}_h(\bar{\omega})\end{Bmatrix}=\begin{Bmatrix}\bar{F}_{ext}(\bar{\omega})\\ \mathbf{0}_h\end{Bmatrix} \tag{90}$$

and the scalar flow coefficients were identified as:

$$\begin{aligned} \bar{m}^F_{mm} &= 1.74 \quad ; \quad \bar{c}^F_{mm} = 0.325 \quad ; \quad \bar{k}^F_{mm} = -3.422 \\ \bar{\boldsymbol{M}}^F_{hh} &= 1 \quad ; \quad \bar{\boldsymbol{C}}^F_{hh} = 0.560 \quad ; \quad \bar{\boldsymbol{K}}^F_{hh} = 1.189 \\ \bar{\mathbf{M}}^F_{mh} &= 0 \quad ; \quad \bar{\mathbf{C}}^F_{mh} = 0.993 \quad ; \quad \bar{\mathbf{K}}^F_{mh} = 0.238 \end{aligned} \tag{91}$$

The improved fitting of the damping stemming from the flow DOF is obvious.

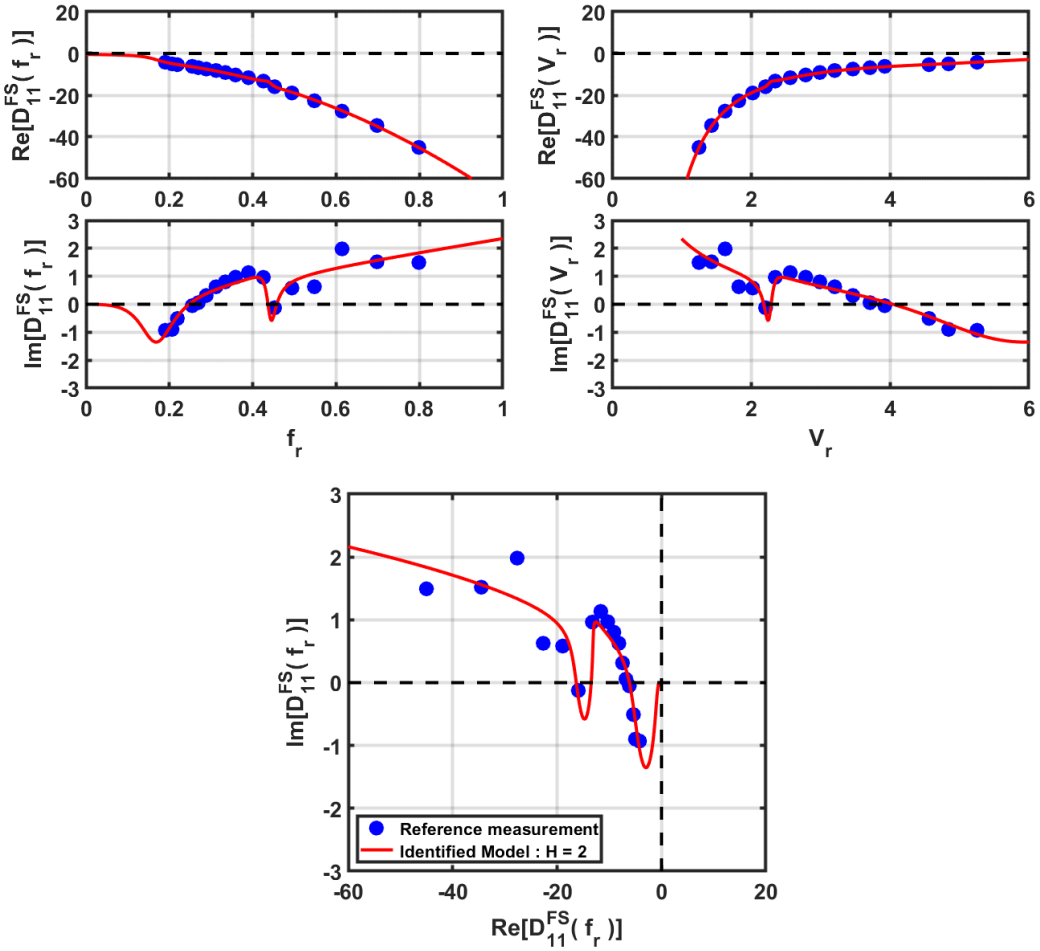

Fig. 21. Experiments performed at CEA-Saclay by Piteau et al. (2018): Reference measurement $\hat{\bar{D}}^{FS}_{11}(\bar{\omega})$ and reconstructed $\bar{D}^{FS}_{11}(\bar{\omega})$ from the identified model with order $H = 2$.

The case $H = 2$ presented in Fig. 21 leads to the dimensionless model (90) with the following identified scalar and matrix coefficients:

$$\begin{aligned} \bar{m}^F_{mm} &= 1.72 \quad ; \quad \bar{c}^F_{mm} = 0.384 \quad ; \quad \bar{k}^F_{mm} = -0.432 \\ \bar{\boldsymbol{M}}^F_{hh} &= \begin{bmatrix} 1 & 0 \\ 0 & 1 \end{bmatrix} \quad ; \quad \bar{\boldsymbol{C}}^F_{hh} = \begin{bmatrix} 0.644 & 0 \\ 0 & 0.162 \end{bmatrix} \quad ; \quad \bar{\boldsymbol{K}}^F_{hh} = \begin{bmatrix} 1.19 & 0 \\ 0 & 7.69 \end{bmatrix} \\ \bar{\mathbf{M}}^F_{mh} &= \begin{bmatrix} 0 & 0 \end{bmatrix} \quad ; \quad \bar{\mathbf{C}}^F_{mh} = \begin{bmatrix} 1.05 & 0.299 \end{bmatrix} \quad ; \quad \bar{\mathbf{K}}^F_{mh} = \begin{bmatrix} 0.253 & -0.231 \end{bmatrix} \end{aligned} \tag{92}$$

This model order already seems to capture the essential features of the identified experimental data, and might therefore be usable for predictive purposes.

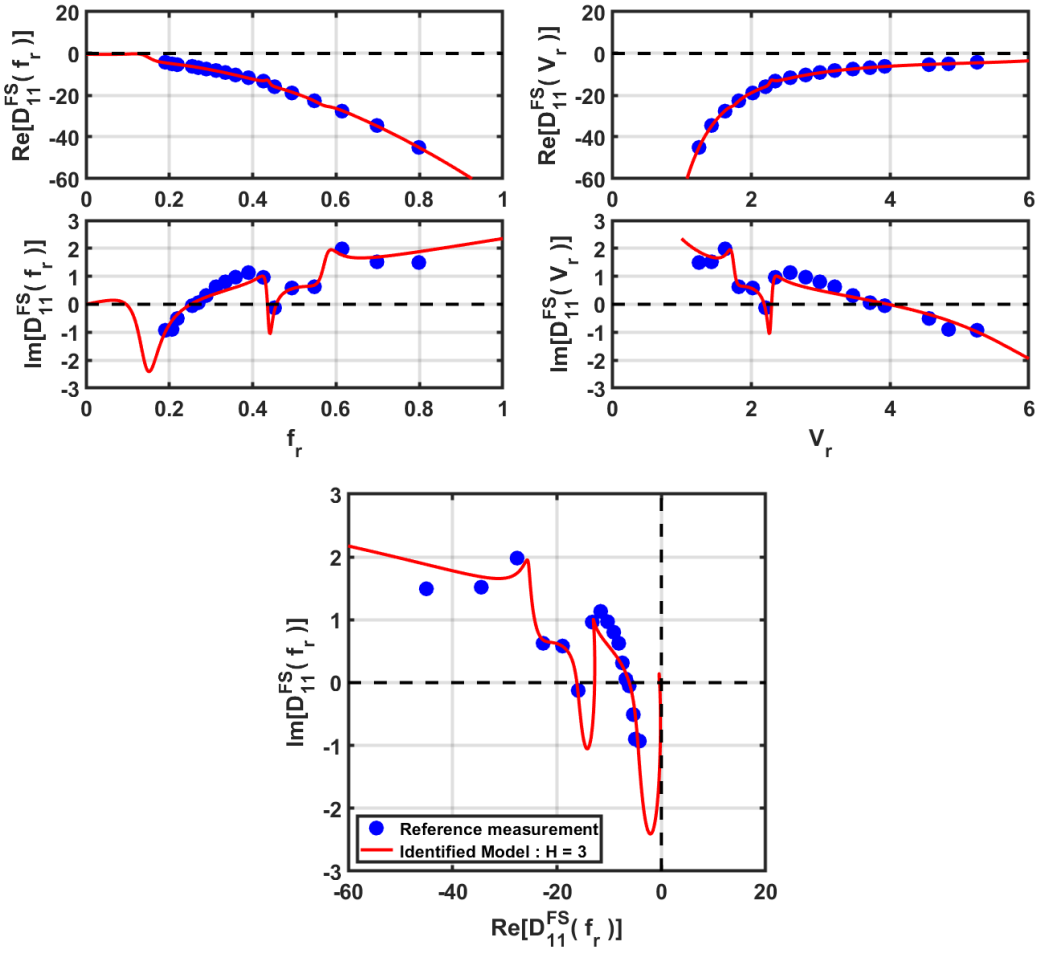

Fig. 22. Experiments performed at CEA-Saclay by Piteau et al. (2018): Reference measurement $\hat{\bar{D}}_{11}^{FS}(\bar{\omega})$ and reconstructed $\bar{D}_{11}^{FS}(\bar{\omega})$ from the identified model with order $H=3$.

Finally, Fig. 22 presents the results obtained for the case $H=3$, corresponding the following identified model:

$$\bar{m}_{mm}^{F}=1.73 \quad ; \quad \bar{c}_{mm}^{F}=0.382 \quad ; \quad \bar{k}_{mm}^{F}=-0.335$$

$$\bar{\boldsymbol{M}}_{hh}^{F}=\begin{bmatrix}1&0&0\\0&1&0\\0&0&1\end{bmatrix} \; ; \; \bar{\boldsymbol{C}}_{hh}^{F}=\begin{bmatrix}0.376&0&0\\0&0.0918&0\\0&0&0.250\end{bmatrix} \; ; \; \bar{\boldsymbol{K}}_{hh}^{F}=\begin{bmatrix}0.857&0&0\\0&7.58&0\\0&0&13.0\end{bmatrix} \qquad (93)$$

$$\bar{\mathbf{M}}_{mh}^{F}=\begin{bmatrix}0&0&0\end{bmatrix} \; ; \; \bar{\mathbf{C}}_{mh}^{F}=\begin{bmatrix}1.05&0.242&0.160\end{bmatrix} \; ; \; \bar{\mathbf{K}}_{mh}^{F}=\begin{bmatrix}-0.0385&-0.287&0.851\end{bmatrix}$$

This model order is possibly the best to capture the experimental data, beyond which overfitting may occur, leading to degrading performance on extrapolating the experimental range of reduced frequency.

7.4 Application of the proposed fluidelastic formulation in predictive analysis

As a final application of the proposed framework, we apply the experimentally identified flow-structure models to the actual experimental rig used by Piteau et al. (2012, 2018), with the main physical parameters detailed in section 7.1. Moreover, the structural modal coefficients (in air) for the first mode of the flexible tube ($r=1$), are: $m_{rr}^S \equiv m_1^S = 0.0665$ Kg, $c_{rr}^S = 2m_1^S \omega_1^S \zeta_1^S = 0.080$ Ns/m and $k_{rr}^S = m_1^S \left(\omega_1^S\right)^2 = 2208$ N/m, with the modal parameters $\omega_1^S = 2\pi \times 29 = 182.2$ rad/s and $\zeta_1^S = 0.0033$, the excited tube modeshape being $\phi_{rr}^S(x/L) \equiv \phi_{rr}^S(\bar{x}) = d + e\bar{x}$ (for $0 \le \bar{x} \le 1$), with $d = 0.154$ and $e = 0.846$.

We will use here the dimensionless flow models identified with orders $H = 0 \sim 3$, and the physical flow-structure model (77) reads:

$$\left(-\omega^2 \begin{bmatrix} m_{rr}^S + a\, I_r \bar{m}_{mm}^F & \begin{bmatrix} 0 & \cdots & 0 \end{bmatrix} \\ \begin{bmatrix} 0 \\ \vdots \\ 0 \end{bmatrix} & a \begin{bmatrix} 1 & \cdots & 0 \\ \vdots & \ddots & \vdots \\ 0 & \cdots & 1 \end{bmatrix} \end{bmatrix} + i\omega \begin{bmatrix} c_{rr}^S + b\, I_r\, \bar{c}_{mm}^F & b\, J_r \begin{bmatrix} \bar{c}_{mh}^1 & \cdots & \bar{c}_{mh}^H \end{bmatrix} \\ b\, J_r \begin{bmatrix} \bar{c}_{mh}^1 \\ \vdots \\ \bar{c}_{mh}^H \end{bmatrix} & b \begin{bmatrix} \bar{c}_{hh}^1 & \cdots & 0 \\ \vdots & \ddots & \vdots \\ 0 & \cdots & \bar{c}_{hh}^H \end{bmatrix} \end{bmatrix} + \begin{bmatrix} k_{rr}^S + c\, I_r\, \bar{k}_{mm}^F & c\, J_r \begin{bmatrix} \bar{k}_{mh}^1 & \cdots & \bar{k}_{mh}^H \end{bmatrix} \\ c\, J_r \begin{bmatrix} \bar{k}_{mh}^1 \\ \vdots \\ \bar{k}_{mh}^H \end{bmatrix} & c \begin{bmatrix} \bar{k}_{hh}^1 & \cdots & 0 \\ \vdots & \ddots & \vdots \\ 0 & \cdots & \bar{k}_{hh}^H \end{bmatrix} \end{bmatrix} \right) \begin{Bmatrix} Q_r(\omega) \\ \begin{Bmatrix} Q_h^1(\omega) \\ \vdots \\ Q_h^2(\omega) \end{Bmatrix} \end{Bmatrix} = \begin{Bmatrix} f_r^{Ext}(\omega) \\ \begin{Bmatrix} 0 \\ \vdots \\ 0 \end{Bmatrix} \end{Bmatrix} \quad (94)$$

with the modal projection coefficients:

$$I_r = \int_0^1 \left(\phi_{rr}^S(\bar{x})\right)^2 d\bar{x} = \int_0^1 \left(d + e\bar{x}\right)^2 d\bar{x} = d^2 + de + e^2/3 = 0.393 \quad (95)$$

and:

$$J_r = \int_0^1 \phi_{rr}^S(\bar{x})\, d\bar{x} = \int_0^1 \left(d + e\bar{x}\right) d\bar{x} = d + e/2 = 0.577 \quad (96)$$

where the velocity-dependent scaling coefficients a, b and c are given by (79), with $\rho_f = 1000$ Kg/m^3, $D = 0.03$ m and $L = 0.3$ m. Then:

$$a = \frac{1}{2}\rho_f D^2 L = 0.135 \quad ; \quad b = \frac{1}{2}\rho_f V_p D L = 4.5\, V_p \quad ; \quad c = \frac{1}{2}\rho_f V_p^2 L = 150\, V_p^2 \quad (97)$$

From the previous numerical values, we now compute the eigenvalues of the non-forced equation (94), as a function of the flow velocity, in the range $0 \le V_p \le 4$ m/s. From the computed eigenvalues, the modal frequencies and damping values of the flow-structure system are extracted and compared to the experimental results, as a function of V_p. These are presented in Figs. 23 to 26 and the results clearly show the progressive convergence of the eigenvalue predictions from the identified fluidelastic model, as the model order H increases. Also, one can notice the enrichment of the eigenvalues chart, as the order H of the "flow" hidden variables increases. Interestingly, such a behavior is also reported in the work by Langthjem et al. (2006), where linearly increasing eigenvalue branches are described as "predominantly related to fluid motion". In their work, these eigenvalue branches arise from the finite element eigen-formulation of a flexible rod in annular leakage flow, their model including the axial flow rate in the formulation.

One may wonder if these eigenvalue branches pertain to physical modes of the system, or if they are only spurious (although organized) numerical results. It is well known that spurious

eigenvalues often arise from models of coupled systems and depend on subtle modelling details, see Gottlieb and Orzag (1977) or Dawkins et al. (1998). Some methods exist for the identification and/or removal of spurious eigenvalues, see Zebib (1987) and Chen et al. (2000), which were not tested yet on this problem. Under such conditions, one should address with caution this topic. Nonetheless, our current view is that the "extra" eigenvalues appearing in Figures 24 to 26 are not spurious but correspond to actual flow modes, for the following reasons: (*i*) Their number is equal to the order of the hidden flow model, e.g. the number of assumed flow modes; (*ii*) Far from mode-crossings, the physical modal frequency of each branch increases linearly with the flow velocity, a behavior that is consistent with their constant reduced modal frequencies, $\omega_n = \left(V_p / D\right)\bar{\omega}_n$, the branches slopes being given by $\partial\omega_n / \partial V_p = \bar{\omega}_n / D$; (*iii*) The linear increase of these "flow" eigenvalues is disrupted near mode-crossings, showing that these branches effectively couple with the "main" eigenvalue branch of the fluidelastically coupled tube; and (*iv*) Most often, the subtle local changes of eigenvalues resulting from modal interactions follow the experimental data.

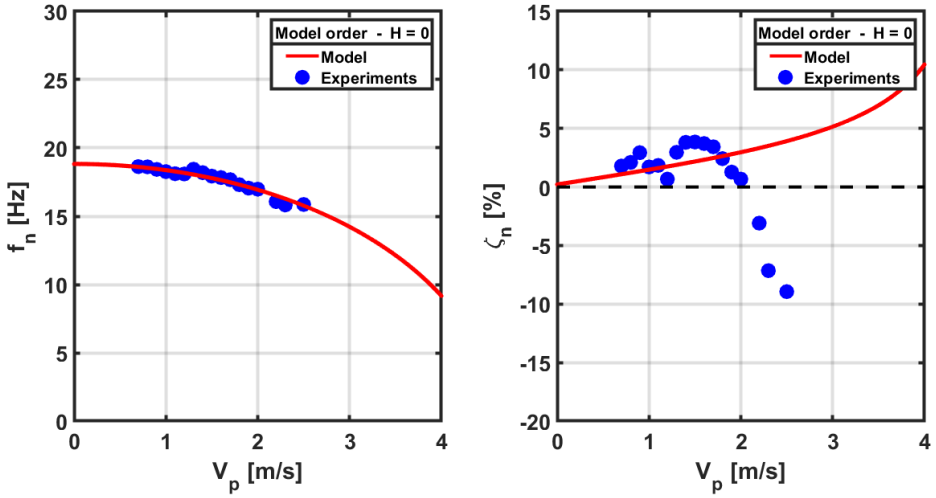

Fig. 23. Experiments performed at CEA-Saclay by Piteau et al. (2018): Reference measured modal frequencies and damping values of the flexible tube, as a function of the flow pitch velocity V_p, and the corresponding modes computed from the identified coupled model with order $H = 0$.

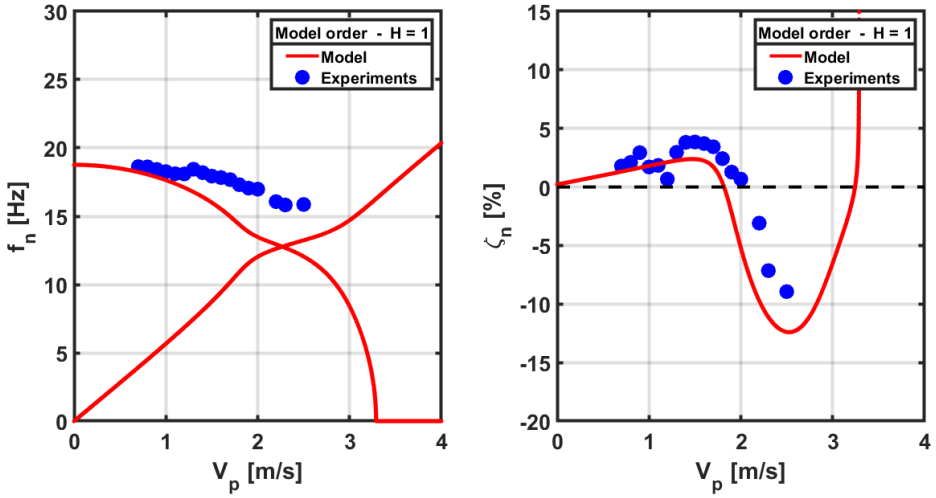

Fig. 24. Experiments performed at CEA-Saclay by Piteau et al. (2018): Reference measured modal frequencies and damping values of the flexible tube, as a function of the flow pitch velocity V_p, and the corresponding modes computed from the identified coupled model with order $H = 1$.

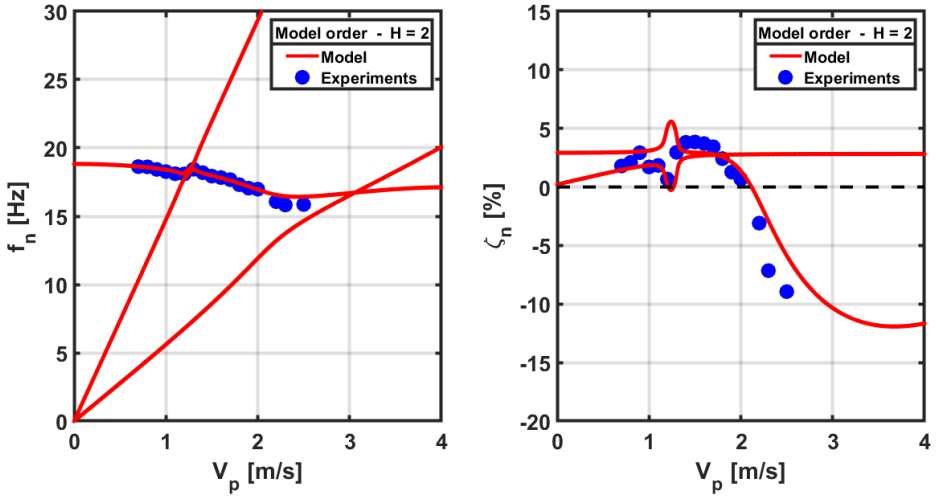

Fig. 25. Experiments performed at CEA-Saclay by Piteau et al. (2018): Reference measured modal frequencies and damping values of the flexible tube, as a function of the flow pitch velocity V_p, and the corresponding modes computed from the identified coupled model with order $H = 2$.

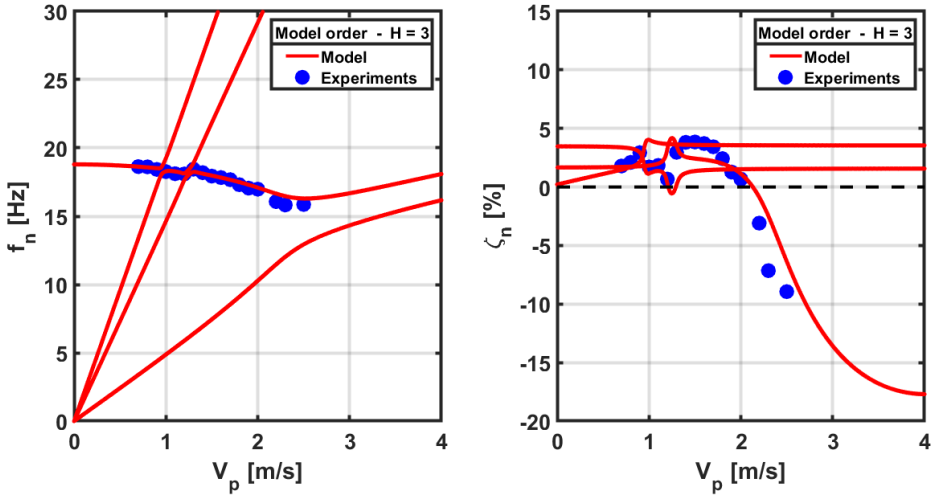

Fig. 26. Experiments performed at CEA-Saclay by Piteau et al. (2018): Reference measured modal frequencies and damping values of the flexible tube, as a function of the flow pitch velocity V_p, and the corresponding modes computed from the identified coupled model with order $H = 3$.

It thus appears that, for the three orders with hidden variables $H = 1 \sim 3$, the identified flow models leads to complex modes, which encapsulate the flow response lags, but also intrinsic flow dynamics at frequencies which essentially increase linearly with the flow velocity.

8. Conclusions

In this paper we developed a new approach for dealing with experimental fluidelastic forces, by explicitly accounting for a set of "hidden" variables connected with the flow internal dynamics. This assumption enables extracting frequency-independent inertia, damping and stiffness matrices from the measured frequency-dependent coefficients. A general framework was developed to convert the experimental frequency-dependent fluidelastic data into a standard second-order matrix formulation of the flow-structure coupled system, which was detailed here for the specific case of symmetric coupling. The relation between the proposed

formulation and similar empirically-based work in aeroelasticity was discussed. Then, the developed formulation and procedures were applied to actual experimental data obtained at CEA-Saclay, for a flexible tube vibrating in the lift direction within a square rigid bundle subjected to cross-flow, with interesting results.

The proposed modelling approach is based on data stemming from fluidelastic force measurements and, therefore, the results obtained will be as good as the quality of the experimental data and the effectiveness of the data-reduction scaling factors. Though this can be stated about any method based on experimental data. The proposed flow modelling and identification approach show significant potential in practical applications, with many definite advantages: (1) Flow-coupling phenomena are described in terms of classical frequency-independent flow mass, damping and stiffness matrices; (2) Explicit modelling of the flow hidden dynamics may allow for increased physical insight, in particular when several moving tubes are coupled; (3) Physical compatibility between the various flow-coupling measurements can be asserted; (4) Stability analysis of the system can be performed through a standard eigen-formulation; (5) Model conversion from the frequency-domain to the time-domain does not entail a frequency interpolation/extrapolation of the measured data; (6) Nevertheless, the frequency interpolation/extrapolation of flow-coupling measurements is immediate and naturally causal; (7) The asymptotic expansion of the measured fluidelastic functions at $\omega \to 0$ and $\omega \to \infty$ stem directly from the modelling approach; (8) Flow-coupling forces are computed from standard ODE instead of costly integral convolutions; (9) The flow-structure coupled dynamics may be analyzed using standard structural dynamics software, and (10) Flow-coupling force dynamics are computed simultaneously with the structural dynamics, not with one time-step delay, even using explicit time-integration algorithms.

The present work should be extended to achieve the conversion of experimental frequency-dependent fluidelastic data to second-order formulation in the general case involving both symmetric and anti-symmetric fluidelastic coupling. This important development will be addressed in subsequent work. Although applied here in the context of heat-exchanger tube-bundle vibrations, the proposed modelling and identification approach obviously embraces a much wider range of coupled flow-structure applications.

Appendix

In this appendix a new method for solving equations (50) :

$$\left[\mathbf{k}_n \;\; \mathbf{c}_n\right]\begin{bmatrix} 1 & 0 \\ 0 & -k_n \end{bmatrix}\begin{bmatrix} \mathbf{k}_n^T \\ \mathbf{c}_n^T \end{bmatrix} = \mathbf{A}_n \quad ; \quad \left[\mathbf{k}_n \;\; \mathbf{c}_n\right]\begin{bmatrix} 0 & 1 \\ 1 & -c_n \end{bmatrix}\begin{bmatrix} \mathbf{k}_n^T \\ \mathbf{c}_n^T \end{bmatrix} = \mathbf{B}_n \quad , \quad n = 1, \cdots, H \tag{98}$$

is presented, applicable when $\mathbf{A}_n$ and $\mathbf{B}_n$ are generic symmetric matrices. We start with the scalar case, when there is only a measured DOF, so that equations (98) become:

$$\left[\mathrm{k}_n \;\; \mathrm{c}_n\right]\begin{bmatrix} 1 & 0 \\ 0 & -k_n \end{bmatrix}\begin{bmatrix} \mathrm{k}_n \\ \mathrm{c}_n \end{bmatrix} = \mathrm{A}_n \quad ; \quad \left[\mathrm{k}_n \;\; \mathrm{c}_n\right]\begin{bmatrix} 0 & 1 \\ 1 & -c_n \end{bmatrix}\begin{bmatrix} \mathrm{k}_n \\ \mathrm{c}_n \end{bmatrix} = \mathrm{B}_n \quad , \quad n = 1, \cdots, H \tag{99}$$

which cannot be addressed by the general method developed in the following, devised for two or more measurement DOF. The scalar form of equations (99) is then more convenient:

$$\mathrm{k}_n^2 - k_n \mathrm{c}_n^2 = \mathrm{A}_n \quad ; \quad 2\mathrm{k}_n \mathrm{c}_n - c_n \mathrm{c}_n^2 = \mathrm{B}_n \quad , \quad n = 1, \cdots, H \tag{100}$$

from which the following solutions are obtained:

$$\mathrm{c}_n = \sqrt{\frac{\left(\mathrm{B}_n c_n - 2\mathrm{A}_n\right) + 2\sqrt{\mathrm{A}_n^2 + k_n \mathrm{B}_n^2 - \mathrm{A}_n \mathrm{B}_n c_n}}{4k_n - c_n^2}} \quad ; \quad \mathrm{k}_n = \frac{\mathrm{A}_n + \sqrt{\mathrm{A}_n^2 + k_n \mathrm{B}_n^2 - \mathrm{A}_n \mathrm{B}_n c_n}}{\mathrm{B}_n} \mathrm{c}_n \tag{101}$$

Actually, from equations (100) one obtains four different solutions for k_n and c_n. The complex solutions are safely disregarded, as both k_n and c_n are real quantities, while the real solutions are equivalent.

The general case of several measurement DOF is considerably harder to solve, and the full vector-matrix equations (98) must be addressed. Then, matrices $\mathbf{A}_n$ and $\mathbf{B}_n$ are of rank 2, whatever the number of the system measurement DOF (greater than 2), so their eigen-decomposition leads to:

$$\mathbf{A}_n = \begin{bmatrix} \boldsymbol{\phi}_{a1} & \boldsymbol{\phi}_{a2} \end{bmatrix} \begin{bmatrix} \lambda_{a1} & 0 \\ 0 & \lambda_{a2} \end{bmatrix} \begin{bmatrix} \boldsymbol{\phi}_{a1}^T \\ \boldsymbol{\phi}_{a2}^T \end{bmatrix} = \begin{bmatrix} \mathbf{k}_n & \mathbf{c}_n \end{bmatrix} \begin{bmatrix} 1 & 0 \\ 0 & -k_n \end{bmatrix} \begin{bmatrix} \mathbf{k}_n^T \\ \mathbf{c}_n^T \end{bmatrix} \tag{102}$$

$$\mathbf{B}_n = \begin{bmatrix} \boldsymbol{\phi}_{b1} & \boldsymbol{\phi}_{b2} \end{bmatrix} \begin{bmatrix} \lambda_{b1} & 0 \\ 0 & \lambda_{b2} \end{bmatrix} \begin{bmatrix} \boldsymbol{\phi}_{b1}^T \\ \boldsymbol{\phi}_{b2}^T \end{bmatrix} = \begin{bmatrix} \mathbf{k}_n & \mathbf{c}_n \end{bmatrix} \begin{bmatrix} 0 & 1 \\ 1 & -c_n \end{bmatrix} \begin{bmatrix} \mathbf{k}_n^T \\ \mathbf{c}_n^T \end{bmatrix} \tag{103}$$

Let us now consider the transformations $\mathbf{T}_a$ and $\mathbf{T}_b$ such that:

$$\mathbf{T}_a \begin{bmatrix} \lambda_{a1} & 0 \\ 0 & \lambda_{a2} \end{bmatrix} \mathbf{T}_a^T = \begin{bmatrix} 1 & 0 \\ 0 & -k_n \end{bmatrix} \quad ; \quad \mathbf{T}_b \begin{bmatrix} \lambda_{b1} & 0 \\ 0 & \lambda_{b2} \end{bmatrix} \mathbf{T}_b^T = \begin{bmatrix} 0 & 1 \\ 1 & -c_n \end{bmatrix} \tag{104}$$

and one obtains, from (102)-(104):

$$\begin{aligned} \mathbf{A}_n &= \begin{bmatrix} \boldsymbol{\phi}_{a1} & \boldsymbol{\phi}_{a2} \end{bmatrix} \begin{bmatrix} \lambda_{a1} & 0 \\ 0 & \lambda_{a2} \end{bmatrix} \begin{bmatrix} \boldsymbol{\phi}_{a1}^T \\ \boldsymbol{\phi}_{a2}^T \end{bmatrix} = \begin{bmatrix} \boldsymbol{\phi}_{a1} & \boldsymbol{\phi}_{a2} \end{bmatrix} \mathbf{T}_a^{-1} \mathbf{T}_a \begin{bmatrix} \lambda_{a1} & 0 \\ 0 & \lambda_{a2} \end{bmatrix} \mathbf{T}_a^T \mathbf{T}_a^{-T} \begin{bmatrix} \boldsymbol{\phi}_{a1}^T \\ \boldsymbol{\phi}_{a2}^T \end{bmatrix} \\ &= \begin{bmatrix} \boldsymbol{\phi}_{a1} & \boldsymbol{\phi}_{a2} \end{bmatrix} \mathbf{T}_a^{-1} \begin{bmatrix} 1 & 0 \\ 0 & -k_n \end{bmatrix} \mathbf{T}_a^{-T} \begin{bmatrix} \boldsymbol{\phi}_{a1}^T \\ \boldsymbol{\phi}_{a2}^T \end{bmatrix} = \begin{bmatrix} \mathbf{k}_n & \mathbf{c}_n \end{bmatrix} \begin{bmatrix} 1 & 0 \\ 0 & -k_n \end{bmatrix} \begin{bmatrix} \mathbf{k}_n^T \\ \mathbf{c}_n^T \end{bmatrix} \end{aligned} \tag{105}$$

and:

$$\mathbf{B}_n = \begin{bmatrix} \boldsymbol{\phi}_{b1} & \boldsymbol{\phi}_{b2} \end{bmatrix} \mathbf{T}_b^{-1} \begin{bmatrix} 0 & 1 \\ 1 & -c_n \end{bmatrix} \mathbf{T}_b^{-T} \begin{bmatrix} \boldsymbol{\phi}_{b1}^T \\ \boldsymbol{\phi}_{b2}^T \end{bmatrix} = \begin{bmatrix} \mathbf{k}_n & \mathbf{c}_n \end{bmatrix} \begin{bmatrix} 0 & 1 \\ 1 & -c_n \end{bmatrix} \begin{bmatrix} \mathbf{k}_n^T \\ \mathbf{c}_n^T \end{bmatrix} \tag{106}$$

hence the expressions:

$$\begin{bmatrix} \mathbf{k}_n & \mathbf{c}_n \end{bmatrix} = \begin{bmatrix} \boldsymbol{\phi}_{a1} & \boldsymbol{\phi}_{a2} \end{bmatrix} \mathbf{T}_a^{-1} \quad ; \quad \begin{bmatrix} \mathbf{k}_n & \mathbf{c}_n \end{bmatrix} = \begin{bmatrix} \boldsymbol{\phi}_{b1} & \boldsymbol{\phi}_{b2} \end{bmatrix} \mathbf{T}_b^{-1} \tag{107}$$

which imply:

$$\begin{bmatrix} \boldsymbol{\phi}_{a1} & \boldsymbol{\phi}_{a2} \end{bmatrix} \mathbf{T}_a^{-1} = \begin{bmatrix} \boldsymbol{\phi}_{b1} & \boldsymbol{\phi}_{b2} \end{bmatrix} \mathbf{T}_b^{-1} \tag{108}$$

We must therefore obtain the transformations $\mathbf{T}_a$ and $\mathbf{T}_b$ that solve the identification problem through (107). Let us write (104) in compact form:

$$\mathbf{T}_a \boldsymbol{L}_a \mathbf{T}_a^T = \mathbf{M}_a \quad ; \quad \mathbf{T}_b \boldsymbol{L}_b \mathbf{T}_b^T = \mathbf{M}_b \tag{109}$$

so that:

$$\mathbf{M}_a^{-1/2} \mathbf{T}_a \boldsymbol{L}_a \mathbf{T}_a^T \mathbf{M}_a^{-1/2} = \boldsymbol{I} \quad ; \quad \mathbf{M}_b^{-1/2} \mathbf{T}_b \boldsymbol{L}_b \mathbf{T}_b^T \mathbf{M}_b^{-1/2} = \boldsymbol{I} \tag{110}$$

and, as noted by Poloni (2020), matrices $\boldsymbol{L}_a$, $\mathbf{M}_a$, $\boldsymbol{L}_b$ and $\mathbf{M}_b$ being symmetric, we have:

$$\mathbf{M}_a^{-1/2} \mathbf{T}_a \boldsymbol{L}_a^{1/2} \boldsymbol{L}_a^{1/2} \mathbf{T}_a^T \mathbf{M}_a^{-1/2} = \mathbf{Q}_a \mathbf{Q}_a^T = \boldsymbol{I} \quad ; \quad \mathbf{M}_b^{-1/2} \mathbf{T}_b \boldsymbol{L}_b^{1/2} \boldsymbol{L}_b^{1/2} \mathbf{T}_b^T \mathbf{M}_b^{-1/2} = \mathbf{Q}_b \mathbf{Q}_b^T = \boldsymbol{I} \tag{111}$$

meaning that:

$$\mathbf{Q}_a = \mathbf{M}_a^{-1/2} \mathbf{T}_a \boldsymbol{L}_a^{1/2} \quad ; \quad \mathbf{Q}_b = \mathbf{M}_b^{-1/2} \mathbf{T}_b \boldsymbol{L}_b^{1/2} \tag{112}$$

where $\mathbf{Q}_a$ and $\mathbf{Q}_b$ are any orthogonal matrices. Then, the matrix transformations read:

$$\mathbf{T}_a = \mathbf{M}_a^{1/2}\mathbf{Q}_a\boldsymbol{L}_a^{-1/2} \quad ; \quad \mathbf{T}_b = \mathbf{M}_b^{1/2}\mathbf{Q}_b\boldsymbol{L}_b^{-1/2} \tag{113}$$

and, accounting for the results (108) and (113):

$$\left[\boldsymbol{\phi}_{a1} \;\; \boldsymbol{\phi}_{a2}\right]\boldsymbol{L}_a^{1/2}\mathbf{Q}_a^{-1}\mathbf{M}_a^{-1/2} = \left[\boldsymbol{\phi}_{b1} \;\; \boldsymbol{\phi}_{b2}\right]\boldsymbol{L}_b^{1/2}\mathbf{Q}_b^{-1}\mathbf{M}_b^{-1/2} \tag{114}$$

with the orthogonality conditions $\mathbf{Q}_a\mathbf{Q}_a^T = \boldsymbol{I}$ and $\mathbf{Q}_b\mathbf{Q}_b^T = \boldsymbol{I}$, which imply $\mathbf{Q}_a^{-1} = \mathbf{Q}_a^T$ and $\mathbf{Q}_b^{-1} = \mathbf{Q}_b^T$, therefore (114) becomes:

$$\left[\boldsymbol{\phi}_{a1} \;\; \boldsymbol{\phi}_{a2}\right]\boldsymbol{L}_a^{1/2}\mathbf{Q}_a^T\mathbf{M}_a^{-1/2} = \left[\boldsymbol{\phi}_{b1} \;\; \boldsymbol{\phi}_{b2}\right]\boldsymbol{L}_b^{1/2}\mathbf{Q}_b^T\mathbf{M}_b^{-1/2} \tag{115}$$

and, pre-multiplying (115) by $\left[\boldsymbol{\phi}_{a1} \;\; \boldsymbol{\phi}_{a2}\right]^T$, one obtains:

$$\boldsymbol{\Phi}_{aa}\boldsymbol{L}_a^{1/2}\mathbf{Q}_a^T\mathbf{M}_a^{-1/2} = \boldsymbol{\Phi}_{ab}\boldsymbol{L}_b^{1/2}\mathbf{Q}_b^T\mathbf{M}_b^{-1/2} \tag{116}$$

with the square matrices $\boldsymbol{\Phi}_{aa} = \left[\boldsymbol{\phi}_{a1} \;\; \boldsymbol{\phi}_{a2}\right]^T\left[\boldsymbol{\phi}_{a1} \;\; \boldsymbol{\phi}_{a2}\right]$ and $\boldsymbol{\Phi}_{ab} = \left[\boldsymbol{\phi}_{a1} \;\; \boldsymbol{\phi}_{a2}\right]^T\left[\boldsymbol{\phi}_{b1} \;\; \boldsymbol{\phi}_{b2}\right]$, hence:

$$\mathbf{Q}_b = \mathbf{M}_b^{1/2}\mathbf{M}_a^{-1/2}\mathbf{Q}_a\boldsymbol{L}_a^{1/2}\boldsymbol{\Phi}_{aa}^T\boldsymbol{\Phi}_{ab}^{-T}\boldsymbol{L}_b^{-1/2} \tag{117}$$

Then, from the orthogonality of $\mathbf{Q}_a$ and $\mathbf{Q}_b$:

$$\mathbf{Q}_b\mathbf{Q}_b^T = \boldsymbol{I} = \left(\mathbf{M}_b^{1/2}\mathbf{M}_a^{-1/2}\mathbf{Q}_a\boldsymbol{L}_a^{1/2}\boldsymbol{\Phi}_{aa}^T\boldsymbol{\Phi}_{ab}^{-T}\boldsymbol{L}_b^{-1/2}\right)\left(\boldsymbol{L}_b^{-1/2}\boldsymbol{\Phi}_{ab}^{-1}\boldsymbol{\Phi}_{aa}\boldsymbol{L}_a^{1/2}\mathbf{Q}_a^T\mathbf{M}_a^{-1/2}\mathbf{M}_b^{1/2}\right) \tag{118}$$

and, from (118):

$$\mathbf{M}_b^{1/2}\mathbf{M}_a^{-1/2}\mathbf{Q}_a\boldsymbol{L}_a^{1/2}\boldsymbol{\Phi}_{aa}^T\boldsymbol{\Phi}_{ab}^{-T}\boldsymbol{L}_b^{-1}\boldsymbol{\Phi}_{ab}^{-1}\boldsymbol{\Phi}_{aa}\boldsymbol{L}_a^{1/2}\mathbf{Q}_a^T\mathbf{M}_a^{-1/2}\mathbf{M}_b^{1/2} = \boldsymbol{I} \tag{119}$$

or:

$$\mathbf{M}_a^{-1/2}\mathbf{M}_b\mathbf{M}_a^{-1/2}\mathbf{Q}_a = \mathbf{Q}_a^{-T}\boldsymbol{L}_a^{-1/2}\boldsymbol{\Phi}_{aa}^{-1}\boldsymbol{\Phi}_{ab}\boldsymbol{L}_b\boldsymbol{\Phi}_{ab}^T\boldsymbol{\Phi}_{aa}^{-T}\boldsymbol{L}_a^{-1/2} \tag{120}$$

with $\mathbf{Q}_a^{-T} = \mathbf{Q}_a$, hence:

$$\mathbf{M}_a^{-1/2}\mathbf{M}_b\mathbf{M}_a^{-1/2}\mathbf{Q}_a = \mathbf{Q}_a\boldsymbol{L}_a^{-1/2}\boldsymbol{\Phi}_{aa}^{-1}\boldsymbol{\Phi}_{ab}\boldsymbol{L}_b\boldsymbol{\Phi}_{ab}^T\boldsymbol{\Phi}_{aa}^{-T}\boldsymbol{L}_a^{-1/2} \tag{121}$$

Notice that (121) is a homogeneous Sylvester equation of the form:

$$\mathbf{M}_1\mathbf{Q}_a = \mathbf{Q}_a\mathbf{M}_2 \quad \text{with} \quad \begin{cases} \mathbf{M}_1 = \mathbf{M}_a^{-1/2}\mathbf{M}_b\mathbf{M}_a^{-1/2} \\ \mathbf{M}_2 = \boldsymbol{L}_a^{-1/2}\boldsymbol{\Phi}_{aa}^{-1}\boldsymbol{\Phi}_{ab}\boldsymbol{L}_b\boldsymbol{\Phi}_{ab}^T\boldsymbol{\Phi}_{aa}^{-T}\boldsymbol{L}_a^{-1/2} \end{cases} \tag{122}$$

and it can be shown that (122) has at least a nonzero solution if $\mathbf{M}_1$ and $\mathbf{M}_2$ share at least one eigenvalue in common, see Horn and Johnson (1991), which is the case here. Equation (122) is of size 2×2 and may be easily recast in the homogeneous form:

$$\mathbf{M}_0\mathbf{q}_a = \mathbf{0} \tag{123}$$

with the vector $\mathbf{q}_a = [Q_a(1,1)\,,\, Q_a(1,2)\,,\, Q_a(2,1)\,,\, Q_a(2,2)]^T$ and matrix:

$$\mathbf{M}_0 = \begin{bmatrix} \left(M_1(1,1) - M_2(1,1)\right) & -M_2(2,1) & M_1(1,2) & 0 \\ -M_2(1,2) & \left(M_1(1,1) - M_2(2,2)\right) & 0 & M_1(1,2) \\ M_1(2,1) & 0 & \left(M_1(2,2) - M_2(1,1)\right) & -M_2(2,1) \\ 0 & M_1(2,1) & -M_2(1,2) & \left(M_1(2,2) - M_2(2,2)\right) \end{bmatrix} \tag{124}$$

The rank of matrix $\mathbf{M}_0$ is 2 and the general solution of equation (123) is given by the nullspace basis of matrix $\mathbf{M}_0$, spanned by the complex vectors $\mathbf{v}_1$ and $\mathbf{v}_2$, which are the two last columns in matrix $\mathbf{V}$ of the Singular Value Decomposition $\mathbf{M}_0 = \mathbf{U}\boldsymbol{S}\mathbf{V}^T$, those pertaining to the two near-zero singular values. Then, the range of possible solutions is given by:

$$\mathbf{q}_a = \alpha\mathbf{v}_1 + \beta\mathbf{v}_2 \tag{125}$$

where α and β are arbitrary complex parameters. Then, we reshape (125) as:

$$\mathbf{Q}_a = \alpha \begin{bmatrix} \mathrm{v}_1(1) & \mathrm{v}_1(2) \\ \mathrm{v}_1(3) & \mathrm{v}_1(4) \end{bmatrix} + \beta \begin{bmatrix} \mathrm{v}_2(1) & \mathrm{v}_2(2) \\ \mathrm{v}_2(3) & \mathrm{v}_2(4) \end{bmatrix} = \alpha \mathbf{V}_1 + \beta \mathbf{V}_2 \tag{126}$$

with parameters α and β determined such that $\mathbf{Q}_a$ is orthogonal, $\mathbf{Q}_a \mathbf{Q}_a^T = \boldsymbol{I}$, which is the only suitable solution. These are computed numerically by minimizing the error:

$$\varepsilon(\alpha, \beta) = \left\| \mathbf{Q}_a \mathbf{Q}_a^T - \boldsymbol{I} \right\|_{L2} = \left\| (\alpha \mathbf{V}_1 + \beta \mathbf{V}_2)(\alpha \mathbf{V}_1 + \beta \mathbf{V}_2)^T - \boldsymbol{I} \right\|_{L2} \tag{127}$$

using $\alpha = \alpha_R + i\alpha_I$ and $\beta = \beta_R + i\beta_I$ when a real-parameter minimizing function is used. Here, the Matlab function "*fmincon*" was used, with an imposed constraint $1 \le \|\mathbf{Q}_a\|_{L2} \le 1 + \varepsilon$ (with $\varepsilon \ll 1$), stemming from the orthogonality of $\mathbf{Q}_a$, which also avoids computing trivial near-zero solutions. A satisfactory convergence of the identified orthogonal matrix $\mathbf{Q}_a^{\mathrm{ide}}$ was thus achieved. Then, from $\mathbf{Q}_a^{\mathrm{ide}}$ and the result (117), the other orthogonal matrix $\mathbf{Q}_b^{\mathrm{ide}}$ may be obtained:

$$\mathbf{Q}_b^{\mathrm{ide}} = \mathbf{M}_b^{1/2} \mathbf{M}_a^{-1/2} \mathbf{Q}_a^{\mathrm{ide}} \boldsymbol{L}_a^{1/2} \boldsymbol{\Phi}_{aa}^T \boldsymbol{\Phi}_{ab}^{-T} \boldsymbol{L}_b^{-1/2} \tag{128}$$

and, finally, the problem solution is given by (115):

$$\left[\mathbf{k}_n \;\; \mathbf{c}_n \right] = \left[\boldsymbol{\phi}_{a1} \;\; \boldsymbol{\phi}_{a2} \right] \boldsymbol{L}_a^{1/2} \left(\mathbf{Q}_a^{\mathrm{ide}} \right)^T \mathbf{M}_a^{-1/2} = \left[\boldsymbol{\phi}_{b1} \;\; \boldsymbol{\phi}_{b2} \right] \boldsymbol{L}_b^{1/2} \left(\mathbf{Q}_b^{\mathrm{ide}} \right)^T \mathbf{M}_b^{-1/2} \tag{129}$$

using the identified orthogonal matrices $\mathbf{Q}_a^{\mathrm{ide}}$ and $\mathbf{Q}_b^{\mathrm{ide}}$. The two solutions (129) are identical.

Acknowledgements

The authors wish to thank Doctor Hugh Goyder, from Cranfield University, UK, for calling their attention to the rich literature in the field of Network Synthesis, as well as his interesting work on the topic, which are related to the identification problem addressed in this paper. Sincere thanks are also due to the three anonymous reviewers, for their careful analysis and relevant comments on this paper, which we believe enabled a significantly improved manuscript.

References

Abel, I. (1979). An analytical design technique for predicting the characteristics of a flexible wing equipped with an active flutter suppression system and comparison with wind-tunnel data. Report NASA TP-1367.

Alyaldin, L., Mureithi, N. 2022. Equivalent Theodorsen function for fluidelastic excitation in a normal triangular array. ASME Journal of Pressure Vessel Technology 144, Paper 061401, 1-10.

Alyaldin, L., Mureithi, N. 2023. An analytical frequency response function for fluidelastic instability model of a normal triangular array in cross-flow. Journal of Sound and Vibration 561, Paper 117752, 1-15.

Anderson, B., Vongpanitlerd, S. 1973. Network analysis and synthesis: A modern systems theory approach. Prentice-Hall, Englewood Cliffs, USA.

Anderson, B., Hassan, M., Mohany, A. 2014. Modelling of fluidelastic instability in a square inline tube array including the boundary layer effect. Journal of Fluids and Structures 48, 362-375.

Antunes, J., Axisa, F., Grunenwald, T. 1996. Dynamics of rotors immersed in eccentric annular flow. Part 1: Theory. Journal of Fluids and Structures 10, 893-918.

Antunes, J., Piteau, P., Delaune, X., Lagrange, R. 2022. Spectral extrapolation of frequency-dependent fluidelastic coupling coefficients from causality enforcing. Transactions of the 26th International Conference on Structural Mechanics in Reactor Technology (SMIRT-26), 10-15 July 2022, Berlin/Potsdam, Germany.

Bhattacharya, S.K., Singh, M. 2015. Network analysis and synthesis. Pearson India Education Services, Uttar Pradesh, India.

Blevins, R.D. 1974. Fluidelastic whirling of a tube row. ASME Journal of Pressure Vessel Technology 96, 263-267.

Blevins, R.D. 2001. Flow-induced vibration. Krieger Publishing Company, Malabar, USA.

Caillaud, S., De Langre, E., Baj, F. 2003. Active vibration control for the measurement of fluidelastic effects. ASME Journal of Pressure Vessel Technology 125, 165-170.

Chen, J.T., Huang, C.X., Wong, F.C. 2000. Determination of spurious eigenvalues and multiplicities of true eigenvalues in the dual multiple reciprocity method using the singular value decomposition. Journal of Sound and Vibration 230, 203-219.

Chen, M., Wang, K., Chen, G. 2020. Passive network synthesis: Advances with inerter. World Scientific, Singapore.

Chen, S.S. 1983a. Instability mechanisms and stability criteria of a group of circular cylinders subjected to cross-flow. Part I: Theory. ASME Journal of Vibration, Acoustics, Stress and Reliability in Design 105, 51-58.

Chen, S.S. 1983b. Instability mechanisms and stability criteria of a group of circular cylinders subjected to cross-flow. Part II: Numerical results and discussion. ASME Journal of Vibration, Acoustics, Stress and Reliability in Design 105, 253-260.

Chen, S.S. 1987. Flow-induced vibration of circular cylindrical structures. Hemisphere Publishing, Washington DC, USA.

Connors, H.J. 1970. Fluidelastic vibration of tube arrays excited by cross-flow. In Flow-Induced Vibration in Heat Exchangers (ed. D.D. Reiff), 42-56. ASME, New York, USA.

Cottereau, R., Clouteau, D., Soize, C. 2007. Construction of a probabilistic model for impedance matrices. Computer Methods in Applied Mechanics and Engineering 196, 2252-2268.

Cummings, W.E. 1962. The impulse response function and ship motions. Schiffstechnik 8, 101-109.

Damaren, C.J. 2000. Time-domain floating body dynamics by rational approximation of the radiation impedance and diffraction mapping. Ocean Engineering 27, 687-705.

Daryanani, G. 1976. Principles of active network synthesis and design. John Wiley & Sons, New York, USA.

Dawkins, P.T., Dunbar, S.R., Douglass, R.W. 1998. The origin and nature of spurious eigenvalues in the spectral tau method. Journal of Computational Physics 147, 441-462.

De Pedro, B., Parrondo, J., Meskell, C., Oro, J.F. 2016. CFD modelling of the cross-flow through normal triangular tube arrays with one tube undergoing forced vibrations or fluid elastic instability. Journal of Fluids and Structures 64, 67-86.

Dowell, E.H. (Editor) 2022. A Modern Course in Aeroelasticity. Springer Nature, Switzerland.

El Bouzidi, S., Hassan, M. 2015. An investigation on time lag causing fluidelastic instability in tube arrays. Journal of Fluids and Structures 57, 264-276.

Eversman, W., Tewari, A. 1991. Consistent rational function approximations for unsteady aerodynamics. Journal of Aircraft 28, 545-552.

Eversman, W., Tewari, A. 1991. Modified exponential series approximation for the Theodorsen function. Journal of Aircraft 28, 553-557.

Friswell, M.I., Inman, D.J., Lam, M. 1997. On the realisation of GHM models in viscoelasticity, Journal of Intelligent Material Systems and Structures 8, 986-993.

Friswell, M.I. 1999. Extracting second-order systems from state-space representations, AIAA Journal 37, 132-135.

Fung, Y.C. 1969. An introduction to the theory of aeroelasticity. Dover Publications Inc., New York, USA.

Ginsberg, J.H. 2001. Mechanical and structural vibrations: Theory and applications. John Wiley & Sons, New York, USA.

Golla, D.F., Hughes, P.C. 1985. Dynamics of viscoelastic structures: A time domain, finite element formulation. Journal of Applied Mechanics 52, 897-906.

Gottlieb, D., Orzag, S.A. 1977. Numerical analysis of spectral methods: Theory and application. SIAM, Philadelphia, USA.

Goyder, H. 2012. Reducing the complexity when modelling damping in vibrating systems. Proceedings of the ASME 2012 International Design Engineering Technical Conference & Computers and Information in Engineering Conference (IDETC/CIE2012), 29-31 August 2012, Chicago, USA.

Granger, S., Païdoussis, M.P. 1996. An improvement to the quasi-steady model with application to cross-flow-induced vibration of tube arrays. Journal of Fluid Mechanics 320, 163-184.

Guillemin, E.A. 1951. A summary of modern methods of network synthesis. Advances in Electronics and Electron Physics 3, 261-303.

Guillemin, E.A. 1957. Synthesis of passive networks: Theory and methods appropriate to the realization and approximation problems. John Wiley & Sons, New York, USA.

Hassan, M., Gerber, A., Omar, H. 2010. Numerical estimation of fluidelastic instability in tube arrays. ASME Journal of Pressure Vessel Technology 132, Paper 041307, 1-11.

Horn, R.A., Johnson, C.R. 1991. Topics in matrix analysis. Cambridge University Press, New York, USA.

Houlston, P.R. 2006. Extracting second-order matrices from state space system. Proceedings of IMechE - Journal of Mechanical Engineering Science 220, 1147-1149.

Inada, F., Kawamura, K., Yasuo, A., Yoneda, K. 2002. An experimental study on the fluidelastic forces acting on a square tube bundle in two-phase cross-flow. Journal of Fluids and Structures 16, 891-907.

Isermann, R., Münchhof, M. 2011. Identification of dynamic systems: An introduction with applications. Springer-Verlag, Berlin, Germany.

Kaneko, S., Nakamura, T., Inada, F., Kato, M., Ishihara, K., Nishihara, T., Mureithi, N., Langthjem, M.A. 2014. Flow-induced vibrations: Classifications and lessons from practical experiences. Academic Press, London, UK.

Karpel, M. 1982. Design for active flutter suppression and gust alleviation using state-space aeroelastic modeling. Journal of Aircraft 19, 221-227.

Lagrange, R., Piteau, P., Delaune, X., Antunes, J. 2019. Fluid-elastic coefficients in single phase cross flow: Dimensional analysis, direct and indirect experimental methods. Proceedings of the ASME 2019 Pressure Vessel and Piping Conference (PVP2019), 14-19 July 2019, San Antonio, USA.

Lagrange, R., Panunzio, D., Piteau, P., Delaune, X., Antunes, J. 2023. A new criterion for the instability threshold of a square tube bundle subject to an air-water cross-flow. Journal of Fluids and Structures 122, Paper 103980, 1-14.

Langthjem, M.A., Morita, H., Nakamura, T., Nakano, M. 2006. A flexible rod in annular leakage flow: Influence of turbulence and equilibrium offset, and analysis of instability mechanisms. Journal of Fluids and Structures 22, 617-645.

Leung, A.Y.T. 1993. Dynamic Stiffness and Substructures. Springer-Verlag, London, UK.

Lever, J., Weaver, D. 1982. A theoretical model for fluid-elastic instability in heat exchanger tube bundles. ASME Journal of Pressure Vessel Technology 104, 147-158.

Li, H., Mureithi, N. 2017. Development of a time delay formulation for fluidelastic instability model. Journal of Fluids and Structures 70, 346-359.

Ljung, L. 1999. System identification: Theory for the user. Prentice-Hall, Upper Saddle River, USA.

Lus, H., De Angelis, M., Betti, R., Longman, R.W. 2003a. Constructing second-order models of mechanical systems from identified state space realizations. Part 1: Theoretical discussions. ASCE Journal of Engineering Mechanics 129, 477-488.

Lus, H., De Angelis, M., Betti, R., Longman, R.W. 2003b. Constructing second-order models of mechanical systems from identified state space realizations. Part 2: Numerical investigations. ASCE Journal of Engineering Mechanics 129, 489-501.

Maia, N., Silva, J.M. 1997. Theoretical and experimental modal analysis. John Wiley & Sons, New York, USA.

Marcel, T. 2011. Simulation numérique et modélisation de la turbulence statistique et hybride dans un écoulement de faisceau de tubes à nombre de Reynolds élevé dans le contexte de l'interaction fluide-structure. Thèse de doctorat, INPT, Institut National Polytechnique de Toulouse.

Meskell, C. 2009. A new model for damping controlled fluidelastic instability in heat exchanger tube arrays. Proceedings of IMechE - Journal of Power Energy 223, 361-368.

Morelli, A., Smith, M.C. 2019. Passive Network Synthesis: An approach to classification. SIAM - Society for Industrial and Applied Mathematics, Philadelphia, USA.

Mureithi, N. 2017. Development of a time delay formulation for fluidelastic instability model. Journal of Fluids and Structures 70, 346-359.

Nishida, S., Azuma, S., Morita, H., Hirota, K., Kawakami, R., Nishikawa, Y. 2018. Evaluation method for in-plane FEI of triangular array tube bundle, Paper FIV2018-149, 1-6, Proceedings of the 9th International Symposium on Fluid-Structure Interactions, Flow-Sound Interactions, Flow-Induced Vibration & Noise, 8-11 July 2018, Toronto, Canada.

Ozdemir, A.A., Gumussoy, S. 2017. Transfer function estimation in system identification toolbox via vector fitting. IFAC - PapersOnLine 50-1, 6232-6237.

Païdoussis, M.P., Price, S.J., De Langre, E. 2011. Fluid-structure interactions: Cross-flow-induced instabilities. Cambridge University Press, New York, USA.

Païdoussis, M.P. 2014. Fluid-structure interactions - Slender structures and axial flow: Volume 1 (2nd Edition). Academic Press - Elsevier, Oxford, UK.

Païdoussis, M.P. 2016. Fluid-structure interactions - Slender structures and axial flow: Volume 2 (2nd Edition). Academic Press - Elsevier, Oxford, UK.

Paronesso, A., Wolf, J.P. 1995. Global lumped-parameter model with physical representation for unbounded medium. Earthquake Engineering and Structural Dynamics 24, 637-654.

Pettigrew, M.J., Taylor, C.E., Fisher, N.J. 2022. Flow-induced vibration handbook for nuclear and process equipment. ASME - John Wiley & Sons, Hoboken, USA.

Pintelon, R., Schoukens, J. 2012. System identification: A frequency domain approach. IEEE - John Wiley & Sons, Hoboken, USA.

Piteau, P., Delaune, X., Antunes, J., Borsoi, L. 2012. Experiments and computations of a loosely supported tube in a rigid bundle subjected to single-phase flow. Journal of Fluids and Structures 28, 56-71.

Piteau, P., Borsoi, L., Delaune, X., Antunes, J. 2018. Time-domain numerical simulations of a loosely supported tube subjected to frequency-dependent fluid-elastic forces. Journal of Fluids and Structures 81, 383-398.

Piteau, P., Delaune, X., Borsoi, L., Antunes, J. 2019. Experimental identification of the fluid-elastic coupling forces on a flexible tube within a rigid square bundle subjected to single-phase cross-flow. Journal of Fluids and Structures 86, 156-169.

Poloni, F. 2020. Closed form solution for $XAX^T=B$. https://mathoverflow.net/q/366116.

Price, S.J. 1995. A review of theoretical models for fluidelastic instability of cylinder arrays in cross-flow. Journal of Fluids and Structures 9, 463-518.

Price, S.J., Paidoussis, M.P. 1984. An improved mathematical model for the stability of cylinder rows subject to cross-flow. Journal of Sound and Vibration 97, 615-640.

Richardson, M.H., Formenti, D.L. 1982. Parameter estimation from frequency response measurements using rational fraction polynomials. Proceedings of the 1st International Modal Analysis Conference (IMAC), 8-10 November 1982, Orlando, USA.

Rish, I., Grabarnik, G.Y. 2015. Sparse modeling: Theory, algorithms and applications. CRC Press - Taylor & Francis, Boca Raton, USA.

Roberts, B.W. 1962. Low frequency, self-excited vibration in a row of circular cylinders mounted in an airstream. Ph.D. Thesis, University of Cambridge.

Roger, K.L. 1977. Airplane math modeling methods for active control design. AGARD Report CP-228.

Ropars, P., Bonnet, G., Jean, P. 2014. A stabilization process applied to a hidden variables method for evaluating the uncertainties on foundation impedances and their effect on vibrations induced by railways in a building. Journal of Sound and Vibration 333, 1953-1971.

Sawadogo, T., Mureithi, N. 2014a. Fluid-elastic instability study in a rotated triangular tube array subject to two-phase cross-flow. Part 1: Fluid force measurements and time delay extraction. Journal of Fluids and Structures 49, 1-15.

Sawadogo, T., Mureithi, N. 2014b. Fluid-elastic instability study in a rotated triangular tube array subject to two-phase cross-flow. Part 2: Experimental tests and comparison with theoretical results. Journal of Fluids and Structures 49, 16-28.

Sevart, F.D. 1975. Development of active flutter suppression wind tunnel testing technology. U.S. Air Force, Wright Air Development Center, Report AFFDL-TR-74-126.

Takagi, T. 1924. On an algebraic problem related to an analytic theorem of Carathéodory and Fejér and on an allied theorem of Landau. Japanese Journal of Mathematics 1, 83-93.

Tanaka, H., Takahara, S. 1981. Fluid elastic vibration of tube array in cross flow, Journal of Sound and Vibration 77, 19-37.

Tewari, A. 2015. Aeroservoelasticity - Modeling and control. Birkhäuser-Springer, New York, USA.

Tiffany, S.H., Adams, W.M. 1987. Nonlinear programming extensions to rational function approximations of unsteady aerodynamics. Proceedings of the AIAA Symposium on Structural Dynamics and Aeroelasticity, Paper 87-0854, 406-420.

Wagner, H. 1925. Über die entstehung des dynamischen auftriebes von tragflügeln. ZAMM Journal of Applied Mathematics and Mechanics (Zeitschrift für angewandte Mathematik und Mechanik) 5,17-35.

Wolf, J.P. 1991. Consistent lumped-parameter models for unbounded soil: Frequency-independent stiffness, damping and mass matrices. Earthquake Engineering and Structural Dynamics 20, 33-41.

Wolf, J.P. 1994. Foundation vibration analysis using simple physical models. PTR Prentice Hall, Upper Saddle River, USA.

Zebib, A. 1987. Removal of spurious modes encountered in solving stability problems by spectral methods. Journal of Computational Physics 70, 521-525.